

**ACTIVE PLASMONICS: SURFACE PLASMON  
POLARITON MODULATION**

BY

**SYED SALMAAN RASHID**

A Thesis Presented to the  
DEANSHIP OF GRADUATE STUDIES

**KING FAHD UNIVERSITY OF PETROLEUM & MINERALS**

DHAHRAN, SAUDI ARABIA

1963 ١٣٨٣

In Partial Fulfillment of the  
Requirements for the Degree of

**MASTER OF SCIENCE**

In

**ELECTRICAL ENGINEERING**

**DECEMBER 2011**

KING FAHD UNIVERSITY OF PETROLEUM & MINERALS

DHAHRAN 31261, SAUDI ARABIA

DEANSHIP OF GRADUATE STUDIES

This thesis, written by **Syed Salmaan Rashid** under the direction of his thesis advisor and approved by his thesis committee, has been presented to and accepted by the Dean of Graduate Studies, in partial fulfillment of the requirements for the degree of **MASTER OF SCIENCE IN ELCTRICAL ENGINEERING**.

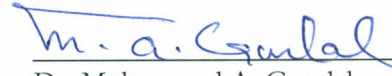
Thesis Committee



Dr. Mohammad A. Alsunaidi (Advisor)



Dr. Hussain Ali Al-Jamid (Member)



Dr. Mohammad A. Gondal (Member)



Dr. Ali Ahmad Al-Shaikhi  
Department Chairman



Dr. Salam A. Zummo  
Dean of Graduate Studies



21/1/12

Date

*I dedicate this thesis to my **grandparents, parents, siblings & relatives** for giving me sweetest  
childhood memories, endless love, immense care and encouragement.*

## ACKNOWLEDGEMENT

All praise, glory and gratitude is to Allah, the most beneficent, the most merciful.

I am heartily thankful to my advisor Dr. Mohammad Alsunaidi for his guidance, valuable suggestions, support and encouragement for finishing my thesis on time. I am grateful to him for precisely organizing my thesis work and for constantly enquiring about my progress in such a manner that he was able to motivate me to finish my work even though he was working nearly 800 miles away from my university.

I would like to thank my thesis committee members, Dr. Hussain Ali Al-Jamid and Dr. Ashraf Gondal for giving valuable advice and for investing their precious time in clarifying my understanding of key concepts. Their comments and positive feedbacks helped me improve my thesis.

I am indebted to many of my fellow graduate students and friends for helping me complete my thesis work and in giving me joyful company throughout. I would like to thank the Department of Electrical Engineering for providing world class facilities and high performance computers to carry-out uninterrupted simulation runs.

Finally, I owe my deepest gratitude to my parents for their support, encouragement and supplications, without which this thesis would not have been accomplished.

# TABLE OF CONTENTS

<b>ACKNOWLEDGEMENT</b> .....	<b>III</b>
<b>TABLE OF CONTENTS</b> .....	<b>IV</b>
<b>LIST OF FIGURES</b> .....	<b>VIII</b>
<b>LIST OF TABLES</b> .....	<b>XI</b>
<b>THESIS ABSTRACT</b> .....	<b>XII</b>
<b>CHAPTER 1</b> .....	<b>1</b>
<b>INTRODUCTION</b> .....	<b>1</b>
1.1 NANOPHOTONICS AND PLASMONICS .....	2
1.2 NEED FOR SPP MANIPULATION .....	4
1.3 IMPORTANCE OF ACTIVE PLASMONICS .....	5
1.4 LITERATURE REVIEW .....	7
1.5 THESIS OBJECTIVE.....	10
1.6 THESIS ORGANIZATION .....	11
<b>CHAPTER 2</b> .....	<b>13</b>
<b>ACTIVE PLASMONICS</b> .....	<b>13</b>
2.1 SURFACE PLASMON POLARITON THEORY .....	13
2.1.1 <i>The Electromagnetic Wave Equation</i> .....	14
2.1.1. (a) Maxwell's equations.....	14
2.1.1. (b) EM Wave Equation .....	15
2.1.2 <i>Surface Plasmon Polariton at Single Interface</i> .....	20

2.1.3 Surface Plasmon Polariton at multiple Interface.....	22
2.2 METHODS OF SPP MODULATION .....	25
2.3 NON-LINEAR OPTICS.....	26
<b>CHAPTER 3 .....</b>	<b>29</b>
<b>MATERIAL MODELS.....</b>	<b>29</b>
3.1 METALS .....	29
3.2 OVERVIEW OF STANDARD MODELS .....	30
3.2.1 The Drude Model.....	30
3.2.2 The Lorentz Model.....	33
3.2.3 The Lorentz-Drude Model.....	34
3.2.4 The Debye Model.....	35
3.3 CHALCOGENIDE GLASS .....	37
3.4 MODELLING NON-LINEAR DISPERSIVE GLASS ( $As_2S_3$ ).....	38
3.4.1 Material Dispersion .....	39
3.4.2 Nonlinear Lorentz model of $As_2S_3$ .....	41
3.4.3 $\chi^{(3)}$ Model for $As_2S_3$ .....	44
<b>CHAPTER 4 .....</b>	<b>46</b>
<b>FDTD SOLUTION FOR SPP WAVES AND NON-LINEAR MATERIAL.....</b>	<b>46</b>
4.1 NUMERICAL SIMULATION.....	46
4.2 OVERVIEW OF THE FDTD METHOD .....	47
4.3 YEE'S ORTHOGONAL GRID .....	49
4.4 MATERIAL DISPERSION IN THE FDTD.....	53

4.4.1 <i>Auxiliary Differential Equation</i> .....	54
4.4.2 <i>The General Algorithm</i> .....	55
4.5 INTEGRATING THIRD ORDER NON-LINEAR SUSCEPTIBILITY $\chi^{(3)}$ INTO THE GENERAL ALGORITHM .....	59
<b>CHAPTER 5</b> .....	<b>62</b>
<b>INVESTIGATION OF SPP MODULATION</b> .....	<b>62</b>
5.1 SIMULATOR VERIFICATION .....	62
5.2 TECHNIQUE USED FOR TESTING THE ALGORITHM FOR NON-LINEAR DISPERSIVE MATERIAL .....	63
5.3 DISPERSION RELATION OF CHALCOGENIDE GLASS .....	67
5.4 TESTING THE ALGORITHM FOR PLASMONIC STRUCTURE .....	68
5.4.1 <i>The Normalized SPP wavelength</i> .....	70
5.4.2 <i>The SPP field penetration depth</i> .....	71
<b>CHAPTER 6</b> .....	<b>73</b>
<b>SIMULATION RESULTS FOR MODULATION OF SURFACE PLASMON POLARITONS</b> .....	<b>73</b>
6.1 GENERAL PULSE CHARACTERISTICS .....	73
6.2 METAL-WAVEGUIDE STRUCTURE .....	75
6.2.1 <i>Model Description</i> .....	75
6.2.2 <i>Input Source</i> .....	76
6.2.3 <i>Results for Inputs with Different Amplitudes</i> .....	78
6.3 METAL-INSULATOR-METAL (MIM) STRUCTURE .....	82

6.3.1 Model Description .....	82
6.3.2 Input Source.....	83
6.3.3 Results for Inputs with Different Amplitudes .....	85
6.4 EMBEDDED METAL FILM STRUCTURE .....	89
6.4.1 Model Description .....	89
6.4.2 Input Source.....	90
6.4.3 Results for Inputs with Different Amplitudes .....	91
6.5 COUPLED PLASMONIC NANOCAVITIES STRUCTURE .....	98
6.5.1 Model Description .....	98
6.5.2 Input Source.....	100
6.5.3 Results for Inputs with Different Amplitudes .....	101
<b>CHAPTER 7 .....</b>	<b>106</b>
<b>CONCLUSIONS AND FUTURE WORKS.....</b>	<b>106</b>
7.1 SUMMARY AND CONCLUSIONS.....	106
7.2 FUTURE WORK.....	108
<b>REFERENCE .....</b>	<b>109</b>
<b>VITAE .....</b>	<b>114</b>



# List of Figures

Figure 2 - 1: Characteristic diagram of planar waveguide geometry. Propagation of wave is along the x-direction in a Cartesian coordinate system.....	17
Figure 2 - 2: Transverse Magnetic Field profile of SPPs at the metal and dielectric interface. ....	20
Figure 2 - 3: Geometry of a three-layer system consisting of a thin layer I sandwiched between two infinitely thick cladding layers (II, III).....	23
Figure 2 - 4: Geometry of a specific three-layer system consisting of metal as thin layer I sandwiched between dielectric represented by two infinite half spaces II and III.....	23
Figure 4 - 1: Yee's spatial grid.....	49
Figure 4 - 2: Leapfrog scheme: the temporal scheme of the FDTD method.....	51
Figure 4 - 3: FDTD algorithm for linear dispersive case. ....	58
Figure 4 - 4: FDTD algorithm for nonlinear dispersive case. ....	61
Figure 5 - 1: 1-D structure to solve non-linear dispersive material of Tafllove [33]. ....	63
Figure 5 - 2: Input pulse in the time domain.....	64
Figure 5 - 3: ADE-FDTD simulation result for linear Lorentz dispersive material at the time of 487fs and 973fs. (a) Published result [33] (b) Simulated result. ....	65
Figure 5 - 4: ADE-FDTD simulation result for linear Lorentz dispersive material at the time of 487fs and 973fs. (a) Published result[10] (b) Simulated result. ....	66
Figure 5 - 5: The dispersion relation of ChG glass.....	68
Figure 5 - 6: The dielectric metal structure considered for the simulator verification. ....	69
Figure 5 - 7: Snapshot of $E_z$ profile of SPP propagating along a Metal-Dielectric interface. 70	

Figure 5 - 8: Normalized SPP wavelength at different free space wavelength.....	71
Figure 5 - 9: Penetration depth of SPP into air versus wavelength. ....	72
Figure 6 - 1: Input Pulse in the time domain .....	74
Figure 6 - 2: Input pulse in the wavelength domain .....	74
Figure 6 - 3: Block diagram of Metal-Waveguide structure. ....	76
Figure 6 - 4: The normalized fundamental mode of the waveguide pumped into the device	77
Figure 6 - 5: The normalized $H_y$ field profile pumped in the device. ....	77
Figure 6 - 6: Snapshot of Metal-Waveguide device with CW SPP and CW waveguide input. .....	78
Figure 6 - 7: The Normalized power curve for different control input levels at the device output. ....	79
Figure 6 - 8: The normalized intensity curve for different control input levels at the device output. ....	80
Figure 6 - 9: Spatial power profile of the Metal-Waveguide structure at low control signal intensity.....	81
Figure 6 - 10: Spatial power profile of the Metal-Waveguide structure at high control signal intensity.....	81
Figure 6 - 11: Block diagram of Metal-Insulator-Metal structure.....	83
Figure 6 - 12: The normalized $E_z$ field profile pumped in the device.....	84
Figure 6 - 13: The normalized $E_z$ field profile pumped in the device.....	84
Figure 6 - 14: Snapshot of the MIM structure with test signal and control signal clearly visible.....	85
Figure 6 - 15: Normalized output power of MIM device at low intensities .....	86
Figure 6 - 16: Normalized output power of MIM device at high intensities .....	86

Figure 6 - 17: Normalized output power of truncated MIM device at low intensities.....	87
Figure 6 - 18: Normalized output power of truncated MIM device at high intensities.....	88
Figure 6 - 19: Block diagram of Embedded Metal Film structure.....	90
Figure 6 -20: The normalized Ez field profile pumped in the device.....	91
Figure 6 - 21: The normalized Ez field profile pumped in the device.....	91
Figure 6 - 22: Snapshot of Embedded Film Structure showing test signal and control signal inputs. ....	92
Figure 6 - 23: Power profile of EMF structure at low control signal intensity (a) Profile of complete device (b) Magnified version. ....	93
Figure 6 - 24: Power profile of EMF structure at high control signal intensity .....	94
Figure 6 -25: Power profile of EMF structure at low control signal intensity (a) Profile of complete device (b) Magnified version. ....	95
Figure 6 - 26: Power profile of EMF structure at low control signal intensity (a) Profile of complete device (b) Magnified version. ....	96
Figure 6 - 27: Power plot of a novel model depicting the coupling behavior of CW SPP along thin metal film for dielectric material of different refractive index.....	97
Figure 6 - 28: Block diagram of Coupled Plasmonic Nanocavities structure. ....	99
Figure 6 - 29: Enlarged view of Metal gratings with clear labeling.....	99
Figure 6 - 30: The normalized Ez field profile pumped in the device.....	101
Figure 6 - 31: Snapshot of CPN structure with only the pulsed Line source switched on..	102
Figure 6 - 32: Snapshot of CPN structure with CW SPP pumped in.....	103
Figure 6 - 33: Power plot of CNP device with gap dimension of 40nm .....	104
Figure 6 - 34: Power plot of CNP device with gap dimension of 20nm .....	105
Figure 6 - 35: Power plot of CNP device with gap dimension of 60nm .....	105

# List of Tables

Table 4 - 1: Algorithm constant:  $C_1$ ,  $C_2$  and  $C_3$  for different dispersion relation models..... 57

# THESIS ABSTRACT

**Name:** Syed Salmaan Rashid

**Title:** Active Plasmonics: Surface Plasmon Polariton Modulation

**Major:** Electrical Engineering

**Date:** December 2011

Free electrons in metals can strongly interact with light to form Surface-Plasmon-Polaritons (SPPs). The resulting electromagnetic waves are confined within sub-wavelength dimensions and can propagate along the metal interface. These waves can potentially be used in many areas such as sensing, imaging, energy and optoelectronics. To efficiently utilize SPP propagation, their relatively short propagation length has to be enhanced. Also, methods of SPP modulation have to be devised. Efficient optical modulation of SPPs will pave the way for great advances in all-optical switching and miniaturization of on-chip circuits. It will also unlock the tremendous potential of nano-scale propagation of SPPs for the possibility to make efficient sensors to be applied in fields such as medicine and drug delivery. The aim of this thesis is to survey the existing methods for SPP modulation and to investigate novel engineering approaches to achieve efficient SPP modulation. The theoretical approach used in the investigations is based on a numerical model recently developed using Finite Difference Time Domain (FDTD) method. Various prototypes that can modulate SPP have been simulated through the use of Chalcogenide (ChG) glass and noble metals. It was found that the designed prototypes when pumped with varying input intensity signals were capable of modulating SPPs by activating the nonlinear behaviour of ChG glass, thus paving the way for fabrication of active devices.

ملخص الرسالة  
درجة الماجستير

الاسم: سيد سلمان راشد

عنوان الرسالة: البلازمونات التفاعلية: طرق جديدة لتحويل البلازمونات السطحية

التخصص: هندسة كهربائية

تاريخ التخرج: ديسمبر 2011

يمكن للإلكترونات في المعادن أن تتفاعل بقوة مع الضوء لتشكيل ما يعرف بالبلازمونات السطحية (SPPs). تنحصر الموجات الكهرومغناطيسية الناجمة عن ذلك في إطار طول موجي أقصر بكثير من الطول الموجي للموجة الضوئية الأصلية. من الممكن استخدام هذه الموجات في العديد من المجالات مثل الاستشعار عن بعد ، والتصوير ، والطاقة والإلكترونيات الضوئية. للاستفادة من كفاءة ال SPP لابد من إيجاد أساليب لتعديلها و التأثير فيها و سيفتح هذا الأمر المجال لمزيد من التطبيقات و في مجالات جديدة مثل الإتصالات و معالجة الإشارات و في مجال التشخيص الطبي و إيصال الدواء إلى الخلايا الحية.

الهدف من هذه الأطروحة هو دراسة الطرق القائمة لتعديل ال SPP و اقتراح أساليب هندسية مبتكرة لتحقيق كفاءة أكثر في تعديل ال SPP. ويستند النهج النظري المستخدم في الدراسة على نموذج عددي وضع مؤخرا باستخدام طريقة FDTD الحسابية. وقد تم وضع نماذج مختلفة لتعديل ال SPP محاكاة باستخدام الخصائص غير الخطية للزجاج من نوع Chalcogenide مع المعادن النبيلة. وقد وجد أن النماذج المصممة قادرة على تحويل ال SPPs من خلال تفعيل السلوك غير الخطي للزجاج عندما ضخّت بإشارات متفاوتة مما يمهد الطريق لتصنيع الأجهزة النشطة.

# CHAPTER 1

## INTRODUCTION

Following the ground-breaking work of Ritchie in the 1950s [1], the concept of collective electronic excitations at metal surfaces found immense applications in wide range of sciences such as surface science, chemistry, physics and biology [2]. These collective electronic excitations at metal surfaces under the influence of incident light are generally referred to as Surface Plasmon Polaritons (SPPs) which propagate along the surface of a conductor.

The fact that the propagation of SPP wave depends strongly on the property of the metal closest to the interface can be exploited for potential use in subwavelength optics. Presently, as the technology is shifting from integrated electronics to integrated photonics, immense research is being carried out in finding ways to manipulate SPPs to act as information carriers in nanophotonic devices which could result in bridging the gap between current electronic and photonic technologies [3] [4].

Renewed interest in SPPs comes from recent advances in developing planar waveguides and photonic crystal structures as fundamental blocks in guiding light in photonic devices [5]. Hence, the possibility of developing highly integrated optical devices by controlling light at sub-wavelength scales to achieve strong guidance and manipulation of light, commonly referred to as “Active Plasmonics”, is being investigated .

Potential applications of active plasmonics are in areas ranging from sub-wavelength light-guiding, solar power generation and high sensitivity material sensing. As mentioned earlier, the most revolutionizing application of SPPs would be the potential prospect of it acting as information carriers in future highly-integrated nanophotonic devices. This can be achieved by combining the speed and bandwidth of photonics with nanoscale component size of electronics and the possibility of integrating them into powerful hybrid devices [6].

Hence, surface-plasmon polaritons can serve as a basis for fabricating nanoscale photonic devices that will be able to conduct electric currents and simultaneously transmit optical signals. This is an exciting challenge which has triggered immense research activity around the globe.

## **1.1 Nanophotonics and Plasmonics**

The science which deals with the physical, chemical or structural nature of nanoscale matter that controls light-matter interaction at wavelength or sub-wavelength scale and which is either engineered artificially or occurs naturally is called as Nanophotonics. Nanophotonic structures can be classified as one-dimensional, two-dimensional or three-dimensional structures based on their structural optical functionality. While Bragg reflectors are famous examples of one-dimensional nanophotonic structures, the form-birefringence comes under the category of two-dimensional nanophotonic structures. Nanophotonic structures can also be divided based on different physical nanoscale phenomenon occurring in the structures driven by physics that is determined by the size scale relative to a wavelength. The four major categories that are classified based on this scheme are



- *Photonic crystals*, in which the optical materials are engineered using periodic dielectric structure with spatial periodicity of the order of the wavelength of the light. These devices enable the tailoring of the propagation of light through the control of the photonic crystal structure [7] [8].
- *Metamaterials*, are individual nanostructures that are fabricated on a scale much smaller than a wavelength and that respond resonantly to either electric or magnetic fields [9].
- *Plasmonics*, in which manipulation of light at the nanoscale is based on the properties of collective oscillations of electron gas termed as ‘surface plasmons’ that arises from metal free-electron response (negative permeability) [10] and
- *Confined semiconductor structures*, occur when a structure’s extent in one or more dimensions becomes comparable to the Fermi wavelength of the charge carrier (i.e., electron or hole) [11].

Plasmonics is the science that deals primarily with the manipulation of light at the nanoscale through collective oscillations of electron gas called Surface Plasmon Polaritons (SPPs). Thus the SPPs are electromagnetic excitations that propagate at the interface between a dielectric and a conductor, evanescently confined in the perpendicular direction and whose electromagnetic field is confined to the near vicinity of the dielectric–metal interface [10]. As a result, enhancement of the electromagnetic field at the interface occurs, resulting in an extraordinary sensitivity of SPPs to surface conditions. There are two consequences due to interaction between light and valence electrons of a conductor. The first consequence is that the SPPs will propagate along the metal surface but will eventually die out as a result of absorption by the metal. The other consequence is that the field perpendicular to the surface

is evanescent in nature making it non-radiative and hence preventing the power from being dissipated from the surface. This striking feature of SPPs makes it a suitable candidate for carrying information in the future photonic devices.

## **1.2 Need for SPP manipulation**

The appetite of mankind for speed and bandwidth has not yet been satisfied and as a result the field of photonics is emerging as an alternative for providing high speed and large bandwidth. But the problem that we are facing today is the lack of ‘All photonic switching device’. This is due to the fact that the researchers are yet to come up with an optimum method of manipulating/modulating electromagnetic waves such as photons/solitons/plasmons which can act as information carriers in integrated photonic devices. Microprocessors built with the latest state of the art technology with transistor gate lengths as small as 35 nm have speeds upto 3 GHz with over 800 million transistors. However, further MOS scaling is leading to high power dissipation and increased circuit delay as the gate lengths approach the single nano-meter scale. This is often referred to as “interconnect bottleneck” [12] [13]. Hence the manipulation of SPPs to act as information carriers leading to development of integrated nanophotonic devices and paving the way for compact, ultrafast and highly sophisticated devices is needed.

### 1.3 Importance of Active Plasmonics

As already stated in the previous section, the science that deals with the behaviour and treatment of electromagnetic signals by coherent coupling of photons to unbound electron oscillations at the conductor-dielectric interface is referred to as 'Plasmonics'.

The diffraction limit of light appears as the fundamental limitation for mankind in its quest for developing ever smaller devices. But the field of nanophotonics comes to its rescue by circumventing this limitation by engaging with the science of plasmonics, where manipulation of light takes place at the nanoscale level through collective oscillations of the electron gas.

The most attractive prospect for Plasmonics arises from the fact that light can be guided in the form of surface plasmon waves on metallic structures paving the way for advancement of integrated semiconductor nano-photonic devices where an all optical information processing can be done without the need for optical to electronic or electronic to optical conversion. This will further enhance the possibility for integrating silicon electronics with photonics on a totally compatible platform.

The research in this field finds several applications ranging from the field of life sciences, energy generation, high-density data storage, information technologies and security. Moreover there is an exponentially growing number of applications being envisaged using the concept of optical "systems on a chip". By integrating electronics with plasmonic nanostructures, the operational characteristics of photo-detectors and light emitting diodes can be improved immensely.

The current surge in the research carried out in the field of plasmonics has led to substantial advancement in engineering of photonic properties of various passive plasmonic components, such as plasmonic metamaterials, plasmonic crystals and waveguides. However, the study of plasmonics was wholly focussed on metallic nanostructures and passive devices with properties fixed by the nanostructure parameters. Simultaneously, in order to achieve real-life applications such as signal switching and modulation, the direct generation and detection of plasmons and amplification required to compensate losses, compelled for the active control of such devices. For all this to be accomplished the functional properties of the materials such as molecular, ferroelectric, nonlinearity etc. needs to be hybridised. Hence we intend to develop and examine hybrid plasmonic nanostructures to facilitate active functionalities in plasmonic circuitry through active modulation of SPPs which can act as information carriers. This thesis will try to unravel the plasmonic's potential for enhancement of real-world optoelectronic and photonic devices and provide insight into physical intricacies for achieving it and thereby catering to the need of optical physics and photonic technologies.

It can be stated that 'Active plasmonics' is a field where active control for modulation of plasmons is achieved either through light compression or amplification in the nanostructures through the change in the intrinsic properties of the dielectric medium by applying electric, thermal, optical, and magnetic field externally.

## 1.4 Literature Review

“We will only be able to speak about ‘plasmonics’ in the same way we speak about ‘photonics’ when efficient techniques for active manipulation of surface plasmon polariton (SPP) signal are identified.” This was the challenge set out by Krasavin et al [14] in a paper published in 2004 and they were the first to introduce the term ‘active plasmonics’. The SPPs are surface phenomenon and hence are very closely confined to metal surfaces. Any change in the material properties close to the metal such as change in the refractive index can cause the SPP to behave in a different manner. This underlying fact was used by Krasavin et al to effectively control the behaviour of SPP by switching the structural phase of polyvalent metals such as Gallium of length few microns placed on silica substrate in a gold film waveguide. Using Otto configuration experiment, Krasavin et al [15] demonstrated high plasmonic contrast between gallium’s solid and liquid forms at a free-space light wavelength of 780 nm leading to control of light with light.

Following this, Nikolajsen et al [16] reported a device which exploited the long-range surface-plasmon-polariton waveguiding along gold stripes implanted in polymer and heated through electrical signal currents named as thermo-optic Mach–Zender interferometry. The geometric outline, construction, and interpretation of the device are studied in detail.

Dominico et al [17] reported a device that consist of a thin layer of CdSe quantum dots (QDs) in which effective interaction between two light beams at different wavelengths is achieved by converting them into co-propagating SPPs. Due to high SPP field confinement and high QD-absorption cross-section in micrometre-scale planar devices the Optical modulation at low power densities was achieved.

Employing photochromic molecules as the active constituents, Ragip et al [18] demonstrated a non-volatile plasmonic switch. The switch contained gratings on either side of an aluminium film coated with photochromic (PC) molecule layer. The first grating helps in exciting SPPs that interact effectively with the PC molecules. A free space optical pump acts as external excitation in absence of which the PC layer allows SPP to propagate and hence the switch is in “ON” state. In the presence of external excitation the SPPs are strongly attenuated turning the switch to “OFF” state. The SPPs are decoupled back into free space and hence enabling measurements of the modulated signal with a far-field detector. An ‘electro-plasmonic’ modulator was reported by Dicken et al [19] by utilizing electro-optic barium titanate as the dielectric layer. The refractive index of ferroelectric BaTiO<sub>2</sub> thin film is achieved by applying bias voltage across silver/barium-titanate SPP waveguide. Hence transmitted light modulation is ascribed to two effects, electrically induced domain switching and electro-optic modulation of the barium titanate index.

S’amson et al [20] reported that the metal component of an aluminium/silica waveguide on direct optical excitation lead to the ultrafast modulation of a femtosecond SPP signal. The transient modulation of SPP signals propagating in the waveguide was achieved by the excitation of an aluminium/dielectric plasmonic waveguide with 200 fs optical pulses. Due to the spectral dispersion of the ultrafast optical modulation effect for an aluminium/silica SPP waveguide in the vicinity of aluminium’s near-infrared interband absorption peak, ‘Fast’ (femtosecond) and ‘slow’ (picosecond) modulation response components were observed.

Cai et al [21] reported a metal-oxide-semiconductor (MOS) field-effect plasmonic modulator operating at 1.55  $\mu\text{m}$  also called as ‘plasMOStor’. It is a waveguide structure that supports both photonic and plasmonic modes. The device basically comprises of metal-MOS-metal

(Ag-SiO<sub>2</sub>-Si-Ag) layers and its transmission coefficient is determined by interference between the two modes. This device utilizes high optical mode confinement to enhance electro-optical non-linearities in Si.

Temnov et al [22] demonstrated an active magneto-plasmonic micro-interferometry, where the surface plasmon wave vector in a gold–ferromagnet–gold trilayer system is controlled using a weak external magnetic field. Here the fact that the magnetic field can modify the properties of electron plasma has been utilized for modulation of SPPs. The manipulation of the SPP wave vector was achieved by applying magnetic field parallel to the interface and perpendicular to the SPP wave vector.

Sámson et al [23] demonstrated active plasmonic switching device based on reversible photo-induced changes in the optical properties of a chalcogenide thin film. The chalcogenide is excited by low-intensity white light resulting in photo-induced change in the efficiency of plasmonic coupling to the silver/Chalcogenide interface.

Christ et al [24] reported a device built up of noble metal nanowires acting as elementary electronic dipole oscillators. Hybridised plasmonic modes are developed due to the strong coupling between resonant excitation of localized and delocalized surface plasmon modes supported by a multilayer metallic photonic crystal slab. The periodic nature of these nanowires enables surface plasmon excitation at the nearby silver film with regard to plasmonic band gap structures due to the Bragg diffraction phenomenon.

Immense research is being carried out throughout the world to optimize and fabricate these active Plasmonic devices in order to propel and revolutionize the usage of fast, compact and sophisticated all optical circuits.

## 1.5 Thesis Objective

The necessity and the urgency for carrying out research in the field of active plasmonics for developing all optical switching devices has motivated us to investigate innovative engineering approaches to achieve efficient SPP modulation. Apart from this the aim of the thesis is,

- To thoroughly understand the intricacies of functioning of active plasmonics. This includes review and evaluating all existing methods of manipulating and modulating SPPs.
- Develop a time-domain multi-dimensional algorithm for the propagation of SPPs in nano structures. The algorithm is general enough to accommodate various material types that are encountered in nano photonics applications.
- Build a FDTD based simulator. The simulator is used to carry out all various investigations including analysis for modal, power, propagation and other characteristics.
- Use the simulator to build and test efficient strategies and techniques for SPP modulation.
- Extract important conclusions.



## 1.6 Thesis Organization

This thesis investigates various innovative engineering approaches to achieve efficient SPP modulation through active control of devices.

- In **Chapter 2**, the basic theory of SPP propagation in general media starting with Electromagnetic Wave Equation has been described. This is followed by the discussion on propagation of SPPs along a single interface and along multiple interfaces. **Chapter 2** lists various methods employed for modulation of SPP along with a detailed discussion about the intricacies of Non-Linear Optics.
- Modeling all the materials involved in the process of SPP propagation is an important step to have a realistic simulation output. Hence, **Chapter 3** elucidates about the different models used widely to represent metals. **Chapter 3** also describes the non-linear model of dispersive materials, where all the parameters affecting the non-linearity are discussed in detail.
- In **Chapter 4**, a time-domain two-dimensional simulator based on the FDTD method and the general dispersive algorithm is presented which is capable of representing the propagation dynamics of SPP in Chalcogenide glass. The third-order nonlinearity of the glass is also accounted for, which is basically a cubic equation and solved in the time domain.
- In **Chapter 5**, the algorithm of the simulator is tested for plasmonic structure by comparing the simulation results with the established equations. In this chapter, the non-linear material model and the dispersive material model are discussed.

- In **Chapter 6**, the detailed results of various devices for modulation of SPPs in non-linear medium are described. In this chapter multi-interface plasmonic structures have been considered. The results were produced for different power levels of pumped signals, analyzed and discussed further.
- **Chapter 7** contains the conclusions of the thesis, where a brief summary of the results is given. Also the extension of this work is described at the end of this chapter.

## CHAPTER 2

# ACTIVE PLASMONICS

### 2.1 Surface Plasmon Polariton Theory

Ritchie [1] predicted that at metal surfaces there could exist self-sustained collective excitations during his investigation of the characteristic energy losses of fast electrons passing through thin metal films. In the course of his further investigation about the impact of the film boundaries on the production of collective excitations he found that the boundary effect is the main cause for the appearance of a new lowered loss due to the excitation of collective surface oscillations. Powell and Swan [25] in a series of electron energy-loss experiments demonstrated the existence of these collective excitations, the quanta of which Stern and Ferrell [26] called ‘the surface plasmon’. Advancements in theoretical and experimental investigations of surface plasmons have taken place ever since.

Interpretation of a great variety of experiments and understanding of various fundamental properties of solids such as the nature of Van der Waals forces, the de-excitation of adsorbed molecules, the classical image potential acting between a point classical charge and a metal surface, the energy transfer in gas–surface interactions, the damping of surface vibrational modes, surface energies etc. was made possible with the help of SPPs.

In the presence of surface roughness or grating the non-radiative surface plasmons in both thin and thick films can couple to electromagnetic radiation. Alternatively, this coupling can

also be achieved by using a prism to enhance the momentum of incident light, as demonstrated by Otto and by Kretschmann [27] which was later used in a large variety of applications.

### 2.1.1 The Electromagnetic Wave Equation

The physical properties of surface plasmon Polaritons can be better explained by first analyzing the wave propagation along the flat interface between a conductor and a dielectric by applying Maxwell's equations. In order to have a clear discussion the equations are first cast in a general form applicable to the guiding of electromagnetic waves.

#### 2.1.1. (a) Maxwell's equations

Maxwell's equations are outlined in the following form:

$$\nabla \cdot D = \rho_{ext} \quad (2.1)$$

$$\nabla \cdot B = 0 \quad (2.2)$$

$$\nabla \times E = -\frac{\partial B}{\partial t} \quad (2.3)$$

$$\nabla \times H = J_{ext} + \frac{\partial D}{\partial t} \quad (2.4)$$

where,

E is the electric field vector in volt per meter

D is the electric flux density vector in coulombs per square meter

H is the magnetic field vector in amperes per meter

B is the magnetic flux density vector in Webbers per square meter

$\rho_{ext}$  is the charge density

$J_{ext}$  is the current density

The electric and magnetic fields are related to polarization  $P$  and magnetization  $M$

$$D = \epsilon_0 E + P \quad (2.5)$$

$$H = \frac{1}{\mu_0} B - M \quad (2.6)$$

Considering the case of linear, isotropic and nonmagnetic media, the relation can be simplified to

$$D = \epsilon_0 \epsilon_r E \quad (2.7)$$

$$B = \mu_0 \mu_r H \quad (2.8)$$

where,

$\epsilon_0$  is the electric permittivity of vacuum in Farad per meter

$\mu_0$  is the magnetic permeability of vacuum in Henry per meter

$\epsilon_r$  is the relative permittivity

$\mu_r$  is the relative permeability

### 2.1.1. (b) EM Wave Equation

The EM wave equation is derived from Maxwell's equations. Using Faraday's law we can combine the curl equations (2.3, 2.4) in the absence of external charge and current densities to yield

$$\nabla \times \nabla \times E = -\mu_o \frac{\partial^2 D}{\partial t^2} \quad (2.9)$$

With the identities  $\nabla \times \nabla \times E \equiv \nabla(\nabla \cdot E) - \nabla^2 E$  and  $\nabla \cdot (\epsilon E) \equiv E \cdot \nabla \epsilon + \epsilon \nabla \cdot E$  and taking  $\nabla \cdot D = 0$  in the absence of external charge, the above equation can be expressed as

$$\nabla \left( -\frac{1}{\epsilon} E \cdot \nabla \epsilon \right) - \nabla^2 E = -\mu_o \epsilon_o \epsilon_r \frac{\partial^2 E}{\partial t^2} \quad (2.10)$$

If the variation of the dielectric profile  $\epsilon$  is negligible over distance, equation (2.10) can be simplified to the following wave equation:

$$\nabla^2 E - \frac{\epsilon_r}{c^2} \frac{\partial^2 E}{\partial t^2} = 0 \quad (2.11)$$

Equation (2.11) needs to be solved separately in regions of constant  $\epsilon$ , and then the solutions are to be matched with appropriate boundary conditions. We assume a harmonic time dependence of the electric field, namely  $E(r,t) = E(r)e^{j\omega t}$  in order to have the solution in a suitable form. Substituting  $E$  in (2.11), we get the Helmholtz equation

$$\nabla^2 E + k_o^2 \epsilon_r E = 0 \quad (2.12)$$

where, the wave vector of the propagation  $k_o = \frac{\omega}{c}$ , correspond to free space.

It is assumed that the wave travels along the x-direction of the Cartesian co-ordinate system, and no spatial variation in y direction as shown in Figure 2-1,

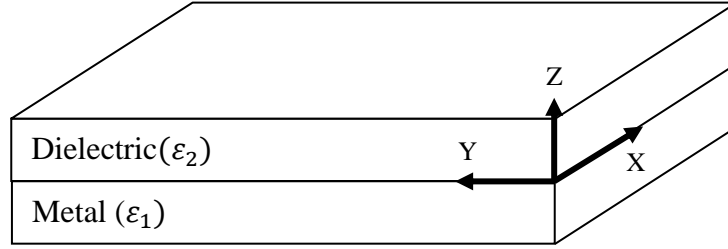


Figure 2 - 1: Characteristic diagram of planar waveguide geometry. Propagation of wave is along the x-direction in a Cartesian coordinate system.

For figure 2-1, we can write  $E(x,y,z)=E(z)e^{j\beta x}$ , where  $\beta=k_x$ , which is called the propagation constant. Now inserting the value of E in equation (2.11) the wave equation takes the following form

$$\frac{\partial^2 E(z)}{\partial z^2} + (k_o^2 \epsilon_r - \beta^2)E = 0 \quad (2.13)$$

A similar equation can be derived for the magnetic field. The field E and H can be decomposed in the Cartesian coordinate system as

$$E = E_x \cdot \vec{a}_x + E_y \cdot \vec{a}_y + E_z \cdot \vec{a}_z \quad (2.14)$$

$$H = H_x \cdot \vec{a}_x + H_y \cdot \vec{a}_y + H_z \cdot \vec{a}_z \quad (2.15)$$

By solving Ampere's law and Faraday's law for harmonic time dependence ( $\frac{\partial}{\partial t} = -j\omega$ ), the following set of coupled equations can be obtained

$$\frac{\partial E_z}{\partial y} - \frac{\partial E_y}{\partial z} = j\omega\mu_o H_x \quad (2.16)$$

$$\frac{\partial E_x}{\partial z} - \frac{\partial E_z}{\partial x} = j\omega\mu_o H_y \quad (2.17)$$

$$\frac{\partial E_y}{\partial x} - \frac{\partial E_x}{\partial y} = j\omega\mu_o H_z \quad (2.18)$$

$$\frac{\partial H_z}{\partial y} - \frac{\partial H_y}{\partial z} = -j\omega\varepsilon_o\varepsilon_r E_x \quad (2.19)$$

$$\frac{\partial H_x}{\partial z} - \frac{\partial H_z}{\partial x} = -j\omega\varepsilon_o\varepsilon_r E_y \quad (2.20)$$

$$\frac{\partial H_y}{\partial x} - \frac{\partial H_x}{\partial y} = -j\omega\varepsilon_o\varepsilon_r E_z \quad (2.21)$$

Since the propagation is assumed along the x-direction in the form  $e^{j\beta x}$ , it then follows that

$\frac{\partial}{\partial x} = -j\beta$ . The homogeneity in the y-direction results in  $\frac{\partial}{\partial y} = 0$ . The system of equations

then simplifies to

$$-\frac{\partial E_y}{\partial z} = j\omega\mu_o H_x \quad (2.22)$$

$$\frac{\partial E_x}{\partial z} - j\beta E_z = j\omega\mu_o H_y \quad (2.23)$$

$$j\beta E_y = j\omega\mu_o H_z \quad (2.24)$$

$$\frac{\partial H_y}{\partial z} = j\omega\varepsilon_o\varepsilon_r E_x \quad (2.25)$$

$$\frac{\partial H_x}{\partial z} - j\beta H_z = -j\omega\varepsilon_o\varepsilon_r E_y \quad (2.26)$$

$$j\beta H_y = -j\omega\varepsilon_o\varepsilon_r E_z \quad (2.27)$$



There are two sets of independent solutions with different polarization properties: Transverse magnetic (TM) modes and Transverse electric (TE) modes. For the TM modes, the governing equations are

$$E_x = -j \frac{1}{\omega \epsilon_0 \epsilon_r} \frac{\partial H_y}{\partial z} \quad (2.28)$$

$$E_z = -\frac{\beta}{\omega \epsilon_0 \epsilon_r} H_y \quad (2.29)$$

The wave equation for TM polarized wave becomes

$$\frac{\partial^2 H_y}{\partial z^2} + (k_o^2 \epsilon_r - \beta^2) H_y = 0 \quad (2.30)$$

Similarly for TE polarized the equation sets are

$$H_x = j \frac{1}{\omega \mu_0} \frac{\partial E_y}{\partial z} \quad (2.31)$$

$$H_z = \frac{\beta}{\omega \mu_0} E_y \quad (2.32)$$

The wave equation for TE waves becomes

$$\frac{\partial^2 E_y}{\partial z^2} + (k_o^2 \epsilon_r - \beta^2) E_y = 0 \quad (2.33)$$

Using above equations the description of surface plasmon polaritons becomes particularly easy.

## 2.1.2 Surface Plasmon Polariton at Single Interface

A single, flat interface (Figure 2-2) flanked by a dielectric, with positive real dielectric constant  $\epsilon_2$  and a metal having a negative real part of the dielectric constant  $\epsilon_1$  is the simplest geometry that can sustain SPP propagation. For metals, the condition that the real part of the dielectric constant be negative can only be fulfilled below the bulk Plasmon frequency  $\omega_p$ . The evanescent decay occurs in the z-direction for the geometry shown in Figure 2-2

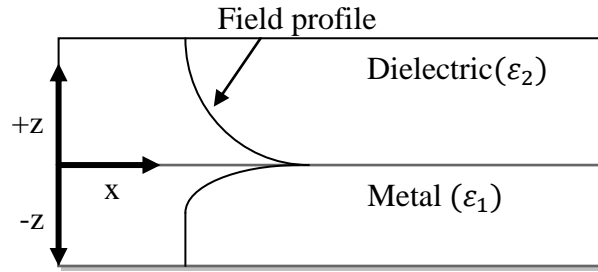


Figure 2 - 2: Transverse Magnetic Field profile of SPPs at the metal and dielectric interface.

For obtaining the TM solution, equation (2.30) can be used in both spaces i.e. metal and dielectric. Applying it for  $z > 0$ , yields

$$H_y(z) = A_2 e^{j\beta x} e^{-k_2 z} \quad (2.34)$$

$$E_x(z) = jA_2 \frac{1}{\omega \epsilon_0 \epsilon_2} k_2 e^{j\beta x} e^{-k_2 z} \quad (2.35)$$

$$E_z(z) = -A_1 \frac{\beta}{\omega \epsilon_0 \epsilon_2} e^{j\beta x} e^{-k_2 z} \quad (2.36)$$

and for  $z < 0$  yields

$$H_y(z) = A_1 e^{j\beta x} e^{k_1 z} \quad (2.37)$$

$$E_x(z) = -jA_1 \frac{1}{\omega \varepsilon_0 \varepsilon_1} k_1 e^{j\beta x} e^{k_1 z} \quad (2.38)$$

$$E_z(z) = -A_1 \frac{\beta}{\omega \varepsilon_0 \varepsilon_1} e^{j\beta x} e^{k_1 z} \quad (2.39)$$

where,  $k_i \equiv k_{z,i}$  ( $i = 1,2$ ) represents the component of the wave vector perpendicular to the interface of the two media.

Continuity of  $H_y$  and  $\varepsilon_i E_x$  at the metal dielectric interface gives  $A_1 = A_2$  and

$$\frac{k_2}{k_1} = -\frac{\varepsilon_2}{\varepsilon_1} \quad (2.40)$$

The surface wave exists at the interface between metal and dielectric with the opposite sign of their real dielectric permittivities. So one can write

$$k_1^2 \varepsilon = \beta^2 - k_o^2 \varepsilon_1 \quad (2.41)$$

$$k_2^2 \varepsilon = \beta^2 - k_o^2 \varepsilon_2 \quad (2.42)$$

The dispersion relation of SPPs propagating in the interface between metal and dielectric can be found using Eqn. (2.40) - (2.42), as

$$\beta = k_o \sqrt{\frac{\varepsilon_1 \varepsilon_2}{\varepsilon_1 + \varepsilon_2}} \quad (2.43)$$

Equation (2.43) is valid for both real and complex  $\varepsilon_1$

Similarly TE surface modes can be expressed for  $z > 0$ , as

$$E_y(z) = A_2 e^{j\beta x} e^{-k_2 z} \quad (2.44)$$

$$H_x(z) = -jA_2 \frac{1}{\omega \mu_0} k_2 e^{j\beta x} e^{-k_2 z} \quad (2.45)$$

$$H_z(z) = -A_2 \frac{\beta}{\omega \mu_0} e^{j\beta x} e^{-k_2 z} \quad (2.46)$$

for  $z < 0$  as

$$E_y(z) = A_1 e^{j\beta x} e^{k_1 z} \quad (2.47)$$

$$H_x(z) = jA_1 \frac{1}{\omega \varepsilon_0 \varepsilon_1} k_1 e^{j\beta x} e^{k_1 z} \quad (2.48)$$

$$H_z(z) = A_1 \frac{\beta}{\omega \varepsilon_0 \varepsilon_1} e^{j\beta x} e^{k_1 z} \quad (2.49)$$

The continuity of  $E_y$  and  $H_x$  requires

$$A_1(k_1 + k_2) = 0 \quad (2.50)$$

It is essential that the real parts of  $k_1$  and  $k_2$  be greater than zero for the waves to be confined to the surface. This is possible only if  $A_1 = 0$  so that  $A_2 = A_1 = 0$ . This implies that no surface modes exist for the TE polarization. SPPs only exist for the TM polarization.

### 2.1.3 Surface Plasmon Polariton at multiple Interface

Multi-layers consisting of alternating conducting and dielectric thin films can sustain bound SPPs at each single interface. Interactions between SPPs give rise to coupled modes provided that the separation between adjacent interfaces is comparable to or smaller than the decay length  $\hat{z}$  of the interface mode. To further explain the general properties of coupled SPPs, geometry of specific three layer systems depicted in Fig. 2.3 will be studied. One of it is an insulator-metal-insulator (IMI) heterostructure having thin metallic layer (I) sandwiched between two infinitely thick dielectric claddings (II, III), and the other is a metal-insulator-metal (MIM) heterostructure having thin dielectric core layer (I) sandwiched between two metallic claddings (II, III).

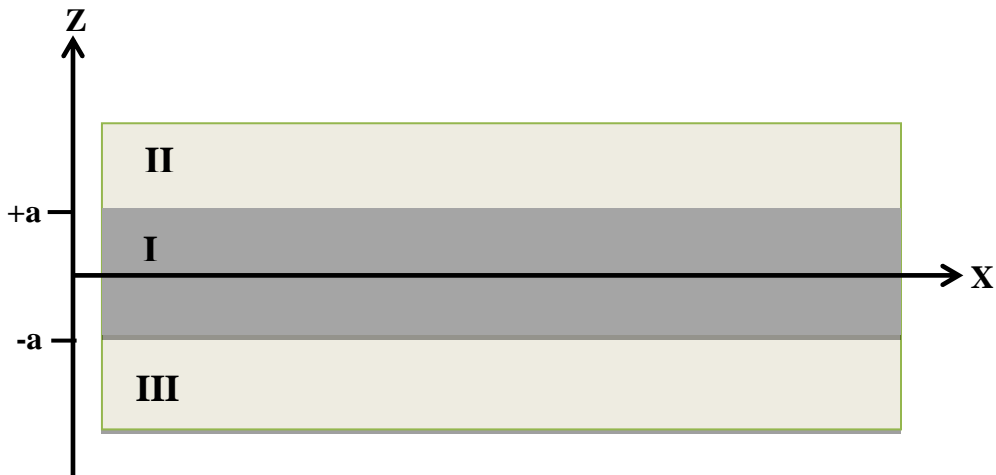


Figure 2 - 3: Geometry of a three-layer system consisting of a thin layer I sandwiched between two infinitely thick cladding layers (II, III)

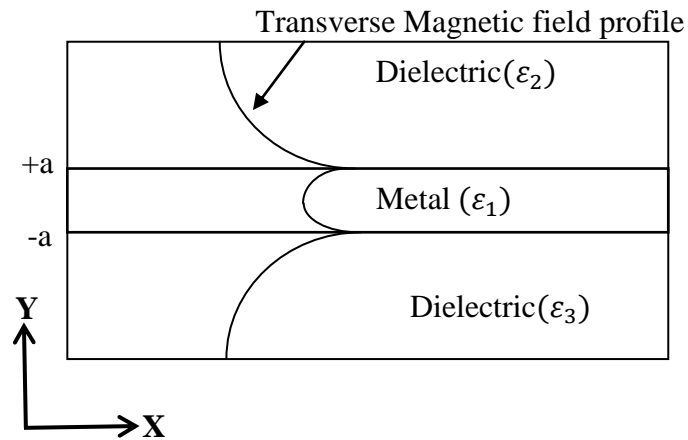


Figure 2 - 4: Geometry of a specific three-layer system consisting of metal as thin layer I sandwiched between dielectric represented by two infinite half spaces II and III.

Beginning with a general description of TM modes that are non-oscillatory in the  $z$ -direction normal to the interfaces, only the lowest-order bound modes are discussed, using Eqn. (2.28) – (2.30). For  $z > a$ , the field components are

$$H_y = Ae^{j\beta x} e^{-k_3 z} \quad (2.51)$$

$$E_x = jA \frac{1}{\omega \epsilon_0 \epsilon_3} k_3 e^{j\beta x} e^{-k_3 z} \quad (2.52)$$

$$E_z = -A \frac{\beta}{\omega \epsilon_0 \epsilon_3} e^{j\beta x} e^{-k_3 z} \quad (2.53)$$

for  $z < -a$ ,

$$H_y = Be^{j\beta x} e^{k_2 z} \quad (2.54)$$

$$E_x = -jB \frac{1}{\omega \epsilon_0 \epsilon_2} k_2 e^{j\beta x} e^{k_2 z} \quad (2.55)$$

$$E_z = -B \frac{\beta}{\omega \epsilon_0 \epsilon_2} e^{j\beta x} e^{k_2 z} \quad (2.56)$$

The above equations conclude that fields decay exponentially in the claddings (II) and (III).

In the core region  $-a < z < a$ , the modes localized at the bottom and top interface couple, yielding

$$H_y = Ce^{j\beta x} e^{k_1 z} + De^{j\beta x} e^{-k_1 z} \quad (2.57)$$

$$E_x = -jC \frac{1}{\omega \epsilon_0 \epsilon_1} k_1 e^{j\beta x} e^{k_1 z} + jD \frac{1}{\omega \epsilon_0 \epsilon_1} k_1 e^{j\beta x} e^{-k_1 z} \quad (2.58)$$

$$E_z = C \frac{\beta}{\omega \epsilon_0 \epsilon_1} e^{j\beta x} e^{k_1 z} + D \frac{\beta}{\omega \epsilon_0 \epsilon_1} e^{j\beta x} e^{-k_1 z} \quad (2.59)$$

Linear system of four coupled equations are obtained due to the condition of continuity of  $H_y$  and  $E_x$ . At  $z = a$

$$Ae^{-k_3 a} = Ce^{-k_1 a} + De^{-k_1 a} \quad (2.60)$$

$$\frac{A}{\varepsilon_3} k_3 e^{-k_3 a} = -\frac{C}{\varepsilon_1} k_1 e^{k_1 a} + \frac{D}{\varepsilon_1} k_1 e^{-k_1 a} \quad (2.61)$$

at  $z = -a$

$$B e^{-k_2 a} = C e^{-k_1 a} + D e^{-k_1 a} \quad (2.62)$$

$$\frac{B}{\varepsilon_2} k_2 e^{-k_2 a} = -\frac{C}{\varepsilon_1} k_1 e^{-k_1 a} + \frac{D}{\varepsilon_1} k_1 e^{k_1 a} \quad (2.63)$$

$H_y$  further has to fulfill the wave equation (2.30) in the three distinct regions, via

$$k_i^2 = \beta^2 - k_o^2 \varepsilon_i \quad (2.64)$$

for  $i = 1, 2, 3$ . An implicit expression for the dispersion relation linking  $\beta$  and  $\omega$  can be obtained by solving this system of linear equations

$$e^{-4k_1 a} = \frac{k_1/\varepsilon_1 + k_2/\varepsilon_2}{k_1/\varepsilon_1 - k_2/\varepsilon_2} \cdot \frac{k_1/\varepsilon_1 + k_3/\varepsilon_3}{k_1/\varepsilon_1 - k_3/\varepsilon_3} \quad (2.65)$$

For infinite thickness ( $a \rightarrow \infty$ ), Eqn. (2.65) reduces to Eqn. (2.40), which represents equation of two uncoupled SPP at the respective interfaces.

## 2.2 Methods of SPP Modulation

High-speed photonic components and small-size electronic circuits can be interfaced with Plasmonic devices provided surface plasmon polaritons (SPP) can be made to act as optical information carriers. Light manipulation on subwavelength scales can be achieved by exploiting the unique properties of SPPs such as high localization and remarkable field enhancement at metal/dielectric interface. Functionalities of traditional electrical circuits

such as guiding, switching and multiplexing can be achieved on plasmonic chips by effective modulation of SPP with the help of nanostructures or tailored excitation of optical beams. Beams with amplitude modulation, phase modulation [28] and frequency modulation are used as light sources for this purpose.

The various methods for manipulating SPPs that are reported in research work are Otto configuration experiment, thermo-plasmonics, Mach–Zender interferometric modulator (MZIM) [16], directional-coupler switch (DCS) configurations, SPP-induced generation of excitons in CdSe quantum dots [17], non-volatile plasmonic switch employing photochromic molecules [18], electro-plasmonic modulator [19], ultrafast modulation of a femtosecond SPP signal via the direct optical excitation [20] and metal-oxide-semiconductor (MOS) field-effect plasmonic modulator [21], etc.

### 2.3 Non-Linear Optics

The study that deals with the interaction of radiation with matter in which response of the matter (described by certain parameters such as electric polarization or power absorption) is not proportional to incident radiation (such as incident electric field strength or energy flux) is known as “Non-linear Optics”. Before the invention of laser devices many optical phenomenon were described by assuming that the optical materials respond linearly to the incident light in the area of conventional optics.

For instance, in conventional optics, the electric polarization vector  $P$  is assumed to be linearly proportional to the Electric field strength  $E$  of an applied optical wave as shown in the Eqn. 2.66



$$P = \varepsilon_0 \chi E \quad (2.66)$$

where,  $\chi$  is the susceptibility of a given medium and  $\varepsilon_0$  is the free space permittivity.

Based on this linear assumption it was believed that there can be no coupling between different light beams or different monochromatic components when they pass through the same medium. Similarly it was assumed that the attenuation of an optical beam propagating in an absorbing medium is linearly proportional to the local intensity itself. Moreover it was supposed that the transmitted intensity of light through a medium was linearly proportional to the incident intensity, based on the belief that refractive index of a medium is constant and independent of the incident beam intensity for a given wavelength.

This notion of linearity in optics changed after the invention of the first laser. The above mentioned equation (Eqn. 2.66) was unable to explain second harmonic frequency generation at an optical frequency observed in the piezoelectric crystal sample pumped with laser beam. Moreover, it was unable to explain optical sum-frequency generation, optical difference-frequency generation and third-harmonic generation discovered subsequently.

It was then realized that the new effects could be realistically explained by replacing the linear term on the right hand side of Eqn. 2.66 with by a power series as shown in Eqn. 2.67

$$P = \varepsilon_0 [\chi^{(1)} E + \chi^{(2)} E^2 + \chi^{(3)} E^3 + \dots] \quad (2.67)$$

where,  $\chi^{(1)}$ ,  $\chi^{(2)}$  and  $\chi^{(3)}$  are first order (linear), second order (non-linear), and third-order (non-linear) susceptibilities and so on, eventually giving rise to the birth of a new science called 'Non-linear Optics' [29].

In non-linear optics the principle of superposition is no longer valid as is clearly evident from Eqn. 2.67. As a result the interaction between the spectral components of the electromagnetic field occurs through the nonlinear interaction with the matter. Optical Kerr effect, stimulated Raman scattering, self-focusing and Optical Solitons are few more examples which fall under non-linear optics.

## CHAPTER 3

# MATERIAL MODELS

### 3.1 Metals

Silver and gold are the primary metals that support the confinement and propagation of SPPs at optical wavelengths. Hence knowledge of various material models is necessary to gain insight about the behavior and functionality of SPPs.

Metals behave as perfect conductors at low frequencies and hence do not support any fields within it. At frequencies in the optical range, metals become dispersive materials and hence act as dielectrics supporting the existence of fields within it. These fields die out at distance of few nanometers within it. Many models have been proposed to explain the behavior of metals at high frequencies some of which are discussed in this chapter.

The behavior of any material can be determined from three vectors i.e. D: the electrical flux density, E: the electric field intensity and P: the polarization density under the influence of external oscillating EM field.

The above quantities can be related using the following constitutive relation in the frequency domain,

$$D(\omega) = \varepsilon(\omega)E(\omega) \quad (3.1)$$

$$P(\omega) = \varepsilon_o\chi(\omega)E(\omega) \quad (3.2)$$

$$D(\omega) = \varepsilon_0 E(\omega) + P(\omega) \quad (3.3)$$

Combining (3.2) and (3.3), we have

$$D(\omega) = \varepsilon_0 E(\omega)(1 + \chi(\omega)) \quad (3.4)$$

where,  $\chi$  is the electric susceptibility, which is a measure of how easily the dielectric is polarized in response to an applied electric field.

Combining (3.1) and (3.4) we get

$$\varepsilon(\omega) = \varepsilon_0(1 + \chi(\omega)) \quad (3.5)$$

So the relative permittivity can be written as

$$\varepsilon_r(\omega) = 1 + \chi(\omega) \quad (3.6)$$

For linear isotropic materials these quantities are simple, whereas the dispersive materials have frequency dependent permeability and susceptibility.

## 3.2 Overview of Standard Models

The two main aspects based on which the dispersion relation is derived are Electron oscillation and Electric dipole relaxation. Drude model and Lorentz model for permittivity is derived based on Electron oscillation concept and the Debye model for permittivity is derived based on dipole relaxation.

### 3.2.1 The Drude Model

At the beginning of the twentieth century, Paul Drude [30] [31] developed a model to describe the transport properties of electrons in metals. It was named after him as the Drude model. He proposed that the metals contain sea of constantly jittering electrons bouncing

and rebounding off heavier, relatively immobile positive ions following the kinetic theory of gases. These electrons under the influence of external electric field were presumed to travel inside the metal without interacting with each other due to the charge shielding effect.

The driving force and the damping force act on the electrons travelling in a metal. The driving force  $F_d$  is defined by the following Eqn.

$$F_d = qE = -eE \quad (3.7)$$

and the damping force  $F_g$  is defined as

$$F_g = -\Gamma v \quad (3.8)$$

They act opposite to each other, so the resultant force becomes

$$F = F_d - F_g \quad (3.9)$$

Applying Newton's first law of motion,

$$mr'' = -eE + \Gamma r' \quad (3.10)$$

where:

$m$  is the mass of an electron.

$\Gamma$  is damping constant in Newton second per meter.

$r$  is displacement in meter.

$v$  is velocity of the electron.

$e$  is electron's charge.

the prime indicates differentiation with respect to time.

The time harmonic electric field can be written in frequency domain as

$$E(t) = E_0 e^{-j\omega t} \Leftrightarrow E(\omega) \quad (3.11)$$

similarly time harmonic displacement can be written in frequency domain as

$$r(t) = R_0 e^{-j\omega t} \Leftrightarrow R(\omega) \quad (3.12)$$

After applying the frequency domain transformation to equation (3.10) gives

$$mR''(\omega) - \Gamma mR'(\omega) + eE(\omega) = 0 \quad (3.13)$$

Finding derivatives in time of the above equation gives

$$-m\omega^2 R(\omega) + j\omega m\Gamma R(\omega) + eE(\omega) = 0 \quad (3.14)$$

After simplifying and solving the above equation for R one gets

$$R(\omega) = \frac{-e}{m(j\Gamma\omega - \omega^2)} E(\omega) \quad (3.15)$$

The polarization for electron density denoted by  $n$  is written as

$$P(\omega) = -neR(\omega) \quad (3.16)$$

Combining (3.15) and (3.16) one can write

$$P(\omega) = \frac{ne^2}{m(j\Gamma\omega - \omega^2)} E(\omega) \quad (3.17)$$

The expression for the susceptibility can be obtained from the above equation by dividing it with as  $\epsilon_0 E(\omega)$  as

$$\frac{P(\omega)}{\epsilon_0 E(\omega)} = \frac{ne^2}{\epsilon_0 m(j\Gamma\omega - \omega^2)} = \chi(\omega) \quad (3.18)$$

Substituting equation (3.18) in equation (3.6) gives

$$\epsilon_r(\omega) = 1 + \frac{ne^2}{\epsilon_0 m(j\Gamma\omega - \omega^2)} \quad (3.19)$$

As the plasma frequency  $\omega_p$  is defined as  $\omega_p^2 = \frac{ne^2}{\epsilon_0 m}$ , the above equation can be written as

$$\epsilon_r(\omega) = \left(1 + \frac{\omega_p^2}{j\Gamma\omega - \omega^2}\right) \quad (3.20)$$

According to the Drude model the final relation between D and E is obtained by combining Eqn. 3.1 and 3.20 as

$$D(\omega) = \varepsilon_0 \left( 1 + \frac{\omega_p^2}{j\Gamma\omega - \omega^2} \right) E(\omega) \quad (3.21)$$

For low frequencies, the term  $\Gamma\omega \ll 1$  as  $\Gamma \ll 1$ . So equation (3.21) is simplified to

$$D(\omega) = \varepsilon_0 \left( 1 - \frac{\omega_p^2}{\omega^2} \right) E(\omega) \quad (3.22)$$

The above relationship is referred to as the Drude model.

### 3.2.2 The Lorentz Model

The Lorentz model also called the Lorentz oscillator model explains much of classical optics via a physical picture borrowed from mechanics. It describes the electrons connected to nuclei via an analogy similar to that of “mass on a spring” description. Hence it states that, under the application of incident electric field the electron is under the influence of a spring-like restoring force due to the nucleus. The restoring force  $F_r$  is given by

$$F_r = -kr \quad (3.23)$$

$k$  is the spring constant in Newton/meter

Hence the equation (3.13) becomes

$$mr'' + m\Gamma r' + mkr + eE = 0 \quad (3.24)$$

Converting the above equation into the frequency domain yields

$$R(\omega)(m\omega_o^2 + j\omega m\Gamma - m\omega^2) = -eE(\omega) \quad (3.25)$$

where,  $\omega_o = \sqrt{\frac{k}{m}}$

$R(\omega)$  can be written in terms of  $E(\omega)$  by using the Equation (3.25) as

$$R(\omega) = \frac{-e}{m(\omega_o^2 + j\Gamma\omega - \omega^2)} E(\omega) \quad (3.26)$$

Susceptibility is derived using (3.16) and (3.26) as

$$\frac{P(\omega)}{\varepsilon_0 E(\omega)} = \frac{ne^2}{\varepsilon_0 m(\omega_o^2 + j\Gamma\omega - \omega^2)} = \chi(\omega) \quad (3.27)$$

Expression for  $D$  in the frequency domain on combining equation (3.1) and (3.6) becomes

$$D(\omega) = \varepsilon_0 \left( 1 + \frac{\omega_p^2}{\omega_o^2 + j\Gamma\omega - \omega^2} \right) E(\omega) \quad (3.28)$$

The above relationship is well-known as the Lorentz model.

### 3.2.3 The Lorentz-Drude Model

The Lorentz-Drude model is the most generalized model describing the behavior of a metal under the influence of EM wave. In this model the permittivity of a material is characterized by oscillating electrons of two types. Permittivity of the Drude model is characterized by the oscillation of free electrons and the permittivity of Lorentz model is characterized by the oscillation of bound electrons [32]. Therefore the permittivity of the Lorentz-Drude model is given by

$$\varepsilon = \varepsilon_{free} + \varepsilon_{bound} \quad (3.29)$$

The permittivity characterized by free electron is written as



$$\varepsilon_{free} = 1 + \frac{\omega_p}{j\Gamma\omega - \omega^2} \quad (3.30)$$

and the permittivity characterized by bound electron as

$$\varepsilon_{bound} = \frac{\omega_p}{\omega_o + j\Gamma\omega - \omega^2} \quad (3.31)$$

where,  $\omega_p$  is the frequency of the pole pair.

After combining both in frequency domain, the electric field density becomes

$$D(\omega) = \varepsilon_o \left( 1 + \frac{\omega_p}{j\Gamma\omega - \omega^2} + \frac{\omega_p}{\omega_o + j\Gamma\omega - \omega^2} \right) E(\omega) \quad (3.32)$$

The above relation is referred to as the Lorentz-Drude model.

### 3.2.4 The Debye Model

The Debye model was developed while estimating the phonon contribution to the specific heat (heat capacity) in a solid, by Peter Debye in 1912. According to this model materials are supposed to have electric dipoles and under the influence of electric field, these dipoles imitate the behavior of the field having some relaxation time. Materials are said to have low polarization (or no polarization) if it has long relaxation time and on the other hand materials with short relaxation time are said to possess high polarization. Since metals have very short relaxation times, the polarization in metals is strong.

Under the influence of DC electric field the polarization of the dielectric takes some time to follow the electric field. At steady state the polarization  $P(t)$  is given by

$$P(t) = P_\infty (1 - e^{-t/\tau}) \quad (3.33)$$

Where,

$P_\infty$  is the Polarization in the DC steady state.

$\tau$  is the Time constant.

The derivative of  $P(t)$  is given as

$$\frac{dP(t)}{dt} = \frac{1}{\tau} P_{\infty} e^{-t/\tau} \quad (3.34)$$

Combining (3.33) and (3.34) yields

$$P(t) = P_{\infty} - \tau \frac{dP(t)}{dt} \quad (3.35)$$

As the steady state value of permittivity  $P_{\infty} = \epsilon_0(\epsilon_r - 1)E(t)$  the equation (3.35) reduced to

$$P(t) = \epsilon_0(\epsilon_r - 1)E(t) - \tau \frac{dP(t)}{dt} \quad (3.36)$$

In the frequency domain equation (3.36) becomes

$$\epsilon_0(\epsilon_r - 1)E(\omega) = P(\omega) + j\omega\tau P(\omega) \quad (3.37)$$

On dividing Eqn. (3.37) with  $\epsilon_0 E(\omega)$ , the linear susceptibility thus obtained is expressed as

$$\frac{\epsilon_r - 1}{(1 + j\omega\tau)} = \frac{P(\omega)}{\epsilon_0 E(\omega)} = \chi(\omega) \quad (3.38)$$

From equation (3.6) the permittivity becomes

$$\epsilon_r(\omega) = \chi(\omega) + 1 = \frac{\epsilon_r - 1}{(1 + j\omega\tau)} + 1 \quad (3.39)$$

The boundary conditions for the permittivity function to fit the range from zero frequency to infinite frequency are

$$\epsilon_r(0) = \epsilon_s \text{ and } \epsilon_r(\infty) = \epsilon_{\infty}$$

where,

$\epsilon_s$  is the static permittivity at DC.

$\varepsilon_\infty$  is the permittivity at infinite frequency.

So the modified relation of the permittivity becomes

$$\varepsilon_r(\omega) = \varepsilon_\infty + \frac{\varepsilon_s - \varepsilon_\infty}{(1 + j\omega\tau)} \quad (3.40)$$

Another term related to the conductivity of metal in order to account for the material losses that SPPs experiences is added to the above equation. Equation (3.40) can be expanded as

$$\varepsilon_r(\omega) = \varepsilon_\infty + \frac{\varepsilon_s - \varepsilon_\infty}{(1 + j\omega\tau)} - j \frac{\sigma}{\omega\varepsilon_0} \quad (3.41)$$

Representing the model in terms of its real and imaginary parts yields

$$\varepsilon_r(\omega) = \varepsilon'(\omega) - j\varepsilon''(\omega) \quad (3.42)$$

where the real part of the permittivity is given by,  $\varepsilon'(\omega) = \varepsilon_\infty + \frac{\varepsilon_s - \varepsilon_\infty}{1 + \omega^2\tau^2}$  and the imaginary part of the permittivity is given by,  $\varepsilon''(\omega) = \frac{(\varepsilon_s - \varepsilon_\infty)\omega\tau}{1 + \omega^2\tau^2} + \frac{\sigma}{\omega\varepsilon_0}$ .

Metals in general have negative real part of permittivity for wide range of frequencies. The imaginary part of the permittivity which causes attenuation is large for most of the frequency range. This very large imaginary part of permittivity in metals causes EM waves to experience rapid attenuation inside the metals causing it to behave as perfect conductors. But in the optical range the imaginary and real part of the permittivity is reasonably small and hence supports the propagation of SPPs in the metal.

### 3.3 Chalcogenide Glass

Chalcogenide glasses always contain one or more chalcogen elements such as Sulphur, Selenium or Tellurium in combination with elements from IV<sup>th</sup>, V<sup>th</sup> or VI<sup>th</sup> group of the periodic system such as Arsenide (As), Germanium (Ge), Antimony (Sb), Gallium (Ga),

Silicon (Si) or Phosphorus (P). Chalcogenide glasses have been studied since the 1950's due to their excellent optical properties such as high refractive index, high material nonlinearity combined with the strong confinement and dispersion characteristics making these glasses attractive for the realization of ultrafast nonlinear devices. Chalcogenide glasses find applications as passive devices (lenses, windows, fibers), but these glasses are attractive for preparation of active devices such as laser fiber amplifiers and non-linear components when doped with ions of rare-earth elements. Efficient propagation of SPPs can be obtained using Chalcogenide glass combined with metal, a significant contribution in the field of photonics.

### **3.4 Modelling Non-Linear Dispersive Glass ( $\text{As}_2\text{S}_3$ )**

Most materials exhibit some or the other form of frequency-dependent permittivity. Frequency dependence behavior should be considered in order to model the electromagnetic and optical phenomena of the material. In order to get realistic outputs, inclusion of some form of dispersion is necessary while modeling non-linear optical behavior over a wide frequency range.

Presence of dispersion and non-linearity complicates analytical modeling of non-linear characteristics of chalcogenide glass. Modeling of non-linear dispersive  $\text{As}_2\text{S}_3$  chalcogenide glass is studied in this section. The Lorentz model is used for modeling the linear dispersive behavior and is subsequently upgraded to model the non-linear dispersive behavior of the material. Moreover, only non-linear instantaneous Kerr effect is considered in this chapter.

### 3.4.1 Material Dispersion

The materials having frequency-dependent dielectric constant  $\varepsilon(\omega)$  are referred to as dispersive. As the polarization response of the material cannot be instantaneous the frequency dependence of the dielectric constant comes into picture when a time-varying electric field is applied. Such dynamic response can be described by the convolutional (and causal) constitutive relationship:

$$D(x, t) = \int_{-\infty}^t \varepsilon(t - t') \cdot E(x, t') dt'$$

which becomes multiplicative in the frequency domain:

$$D(x, \omega) = \varepsilon(\omega) \cdot E(x, \omega)$$

Pulse spread is one of the major consequences of material dispersion. Pulse spread is defined as the progressive widening of a pulse as it propagates through a material which has frequency dependent dielectric constant. The data rate at which pulses can be transmitted is severely restricted due to this phenomenon. There are other types of dispersions, such as intermodal dispersion in which several modes may propagate simultaneously with different speeds, or waveguide dispersion introduced by the confining walls of a waveguide.

One can begin the analysis of the material dispersion by considering a one dimensional scalar wave equation. For Electromagnetic waves, the phenomenon in which the phase velocity of wave depends on its frequency is known as Dispersion [33]. The relation between propagating wave's wave number  $k = \frac{2\pi}{\lambda}$  and angular frequency  $\omega = 2\pi f$  is called a dispersion relation. Taking into account the one dimensional scalar wave equation, one can write

$$\frac{\partial^2 u}{\partial t^2} = v^2 \frac{\partial^2 u}{\partial x^2} \quad (3.43)$$

where,  $v^2 = \frac{1}{\mu\epsilon}$

The continuous sinusoidal travelling wave solution of the above equation is written in phasor form as

$$u(x, t) = e^{j(\omega t - kx)} \quad (3.44)$$

where the wave number  $k = \frac{2\pi}{\lambda}$  and the angular frequency  $\omega = 2\pi f$ . Substitution Eqn. 3.44 in Eqn. 3.43 yields

$$(j\omega)^2 e^{j(\omega t - kx)} = v^2 (-jk)^2 e^{j(\omega t - kx)} \quad (3.45)$$

Taking out the common factors from both sides we get

$$k = \pm \frac{\omega}{v} \quad (3.46)$$

This is the dispersion relation for the one dimensional scalar wave equation stated in (3.43). The '+' sign indicates -x directed wave propagation and '-' sign indicates +x directed wave propagation. The magnetic flux density  $B$  and electric flux density  $D$  for dispersive medium is given as

$$D(\omega) = \epsilon(\omega)E \quad (3.47)$$

$$B(\omega) = \mu(\omega)H \quad (3.48)$$

Both  $\epsilon(\omega)$  and  $\mu(\omega)$  are functions of frequency. For non-magnetic dielectric material,  $\mu$  is frequency independent and equals free space permeability and hence can be written as  $\mu = \mu_0$ .

### 3.4.2 Nonlinear Lorentz model of $\text{As}_2\text{S}_3$

In nonlinear materials, the permittivity  $\varepsilon$  may depend on the magnitude  $E$  of the applied electric field in the form:

$$D = \varepsilon(E) \cdot E \quad (3.49)$$

where,  $\varepsilon(E) = \varepsilon + \varepsilon_2 E + \varepsilon_3 E^2 + \dots \dots \dots$

Non-linear effects are sometimes highly desirable for manufacturing devices that finds wide use in day-to-day life. Example of few devices that exhibit Non-linear effects such as electro-optic effects are light phase modulators and phase retarders that are used for altering polarization. In other applications, however, they are undesirable. For example, in optical fibers nonlinear effects become important if the transmitted power is increased beyond a few milliwatts. Generation of higher harmonics is one of the biggest problem the optics industry faces while transmitting signals. For example, if  $E = E_0 e^{j\omega t}$  then eqn. 3.51 becomes,

$$D = \varepsilon E_0 e^{j\omega t} + \varepsilon_2 E_0^2 e^{2j\omega t} + \varepsilon_3 E_0^3 e^{3j\omega t} + \dots \dots \dots \quad (3.50)$$

Thus the input frequency  $\omega$  generates  $2\omega$ ,  $3\omega$ , and so on.

Certain types of non-linear waves such as solitons exist in those materials that are both nonlinear and dispersive. In such materials the spreading effect of dispersion is exactly canceled by the nonlinearity. Therefore, soliton pulses maintain their shape as they propagate in such media.

An accurate description of material response for few media can be perfectly demonstrated using the classical Lorentz model of dielectric dispersion. Polarization of a material can be modeled in such a manner that it represents the dispersive non-linear properties of the material.

So equation (3.50) can be extended to

$$D(\omega) = P_{LN(1)}(\omega) + P_{NL(2)}(\omega) + P_{NL(3)}(\omega) \quad (3.51)$$

Decomposing the susceptibility in the frequency domain yields

$$\chi(\omega) = \chi^{(1)}(\omega) + \chi^{(2)}(\omega)E(\omega) + \chi^{(3)}(\omega)E^2(\omega) \quad (3.52)$$

where,

$P_{LN(1)}$  is the linear polarization.

$P_{NL(2)}$  is second-order non-linear polarization.

$P_{NL(3)}$  is third-order non-linear polarization.

$\epsilon_0$  is the permittivity of free space.

$\epsilon_\infty$  is the relative permittivity in the limit of infinite frequency.

$\chi^{(1)}$  is the linear susceptibility.

$\chi^{(2)}$  is second order non-linear susceptibility.

$\chi^{(3)}$  is third order non-linear susceptibility.

Second order non-linear part  $\chi^{(2)}$  will be ignored in this work as this thesis considers only third order nonlinear material. On analysis of equation (3.49), one can express the linear polarization  $P_{LN(1)}(\omega)$  as



$$P_{LN(1)}(\omega) = \varepsilon_o \chi^{(1)}(\omega) E(\omega) \quad (3.53)$$

Writing Lorentz model for linear polarization as a function of frequency gives

$$P_{LN(1)}(\omega) = \left( \frac{a}{b + j\omega c - d\omega^2} \right) E(\omega) \quad (3.54)$$

where,

$$a = \varepsilon_o(\varepsilon_s - \varepsilon_\infty)\omega_o^2 \quad b = \omega_o^2 \quad c = 2\delta \quad d = 1$$

where,

$\varepsilon_s$  is the static value of the dielectric constant

$\varepsilon_\infty$  is the optical value of the dielectric constant

$\omega_o$  is the material resonance frequency (rad/s)

$\delta$  is the damping factor, ( $s^{-1}$ )

Hence the linear susceptibility of the Lorentz dispersion can be expressed as

$$\chi^{(1)}(\omega) = \frac{a}{\varepsilon_o(b + j\omega c - d\omega^2)} \quad (3.55)$$

From equation (3.54) we can get

$$(b + j\omega c - d\omega^2)P_{LN(1)}(\omega) = aE(\omega) \quad (3.56)$$

Converting it into the time domain yields

$$bP_{LN(1)}(t) + cP'_{LN(1)}(t) + dP''_{LN(1)}(t) = aE(t) \quad (3.57)$$

### 3.4.3 $\chi^{(3)}$ Model for $\text{As}_2\text{S}_3$

In the chapter dealing with the discussion on Non-linear Optics it was mentioned that the polarization of materials cannot be just explained in a linear way. Hence the additional terms were added that represent and explain various nonlinear phenomenon. Rewriting equation 2.67 as

$$P = \varepsilon_0[\chi^{(1)}E + \chi^{(2)}E^2 + \chi^{(3)}E^3 + \dots] \quad (3.58)$$

It is this term  $\chi^{(3)}$  which represents the third order nonlinear behavior of materials. Third order non-linearity is present only in materials possessing centro-symmetry and such materials are also termed as ‘Kerr’ media. Such materials are responsible for the Optical Kerr effect, stimulated Brillouin scattering, Raman scattering, four-wave mixing and third harmonic generation. After simplification of eqn. 3.58 we get

$$n(I) = n + n_2I \quad (3.59)$$

where ‘n’ is the refractive index of the medium, ‘I’ is the intensity of the pumped light and  $n_2$  is the Optical Kerr Coefficient. Equation 3.59 signifies that the change in the refractive index of the medium is proportional to the intensity of light pumped in. This is a very significant phenomenon as this can lead to fabrication of many useful active plasmonic devices.

The third-order nonlinear polarization is given by the time convolution of the electric field  $E(t)$  and the third-order susceptibility function  $\chi^{(3)}(t)$ . Assuming a simple model consisting of an electron and the core of the atoms, using Born-Oppenheimer approximation [34]

$$P_{NL}(t) = \varepsilon_0\chi_o^{(3)}E(t) \int_{-\infty}^t g(t-t')E^2(t')dt' \quad (3.60)$$

where  $\chi_o^{(3)}$  is the third-order nonlinearity coefficient and the causal response function  $g(t)$  is expressed as

$$g(t) = \alpha\delta(t) + (1 - \alpha)g_R(t) \quad (3.61)$$

with

$$g_R(t) = \frac{\tau_1^2 + \tau_2^2}{\tau_1^2\tau_2^2} \exp\left(-\frac{t}{\tau_2}\right) \sin\left(\frac{t}{\tau_1}\right) u(t) \quad (3.62)$$

The function  $u(t)$  is normalized such that

$$\int_{-\infty}^{\infty} g(t) dt = 1 \quad (3.63)$$

Expressing the third order non-linear part of equation (3.51) in the time domain as

$$P_{NL(3)}(t) = P_{NL(3)}^k(t) + P_{NL(3)}^r(t) \quad (3.64)$$

where

$\delta(t)$  represents the spontaneous response of the electrons (Kerr effect).

$g_R(t)$  represents transient Raman scattering.

$1/\tau_1$  is characteristic frequency of response function of damped oscillation.

$\tau_2$  is damping constant.

$\alpha$  is the ratio of the Kerr intensity to the total Kerr and Raman nonlinearity.

$P_{NL(3)}^k$  is the polarization caused by instantaneous Kerr non-linearity.

$P_{NL(3)}^r$  is the polarization caused by Raman effect .

1. **Instantaneous Kerr Nonlinearity:** The polarization of the instantaneous Kerr-nonlinearity is expressed as

$$P_{NL(3)}^k(t) = \varepsilon_o\chi_o^{(3)} E(t) \int_{-\infty}^t \alpha\delta(t - t')E^2(t')dt' = \alpha\varepsilon_o\chi_o^{(3)} E^3(t) \quad (3.65)$$

# CHAPTER 4

## FDTD SOLUTION FOR SPP WAVES AND NON-LINEAR MATERIAL

### 4.1 Numerical Simulation

Numerical simulation is of prime importance in the field of research as it gives the first-hand experience of any device that is to be designed and tested, if modeled appropriately. As it is very cost effective it can be used to manipulate the parameters of choice and perform analysis of the designed model iteratively without worrying about the intricacies of setting up the experiments. Moreover many parameters which cannot be analyzed using experiments can be easily performed and tabulated using numerical simulations. Most of the time, numerical modeling is done on computers and hence very economical in terms of the cost, effort and time. All methods that can reproduce the processes of a system numerically are termed as Numerical simulation. In the field of computational electromagnetics, numerical methods are used for solving differential equations ranging from simple Maxwell's equations to any given complex equations efficiently.

The various methods used for numerical simulation are the Finite Difference Time Domain (FDTD), the finite element method, the Monte Carlo method, the method of moments, the method of weighted residual, Finite Integration Technique (FIT), Pseudo Spectral Time

Domain (PSTD), Pseudo-Spectral Spatial Domain (PSSD), Transmission Line Matrix (TLM), Partial Element Equivalent Circuit (PEEC) method etc. [35] [36]. Among these methods, the FDTD method is very robust and efficient in design and simulation. In this thesis, the FDTD method is used for solving all EM equations numerically.

## 4.2 Overview of the FDTD method

Among the full-wave techniques used to solve problems in electromagnetics the finite-difference time-domain (FDTD) method is arguably the simplest, both conceptually and in terms of implementation. A wide range of complicated problems can be accurately tackled using FDTD. The FDTD method employs finite differences as approximations to both the spatial and temporal derivatives that appear in Maxwell's equations. FDTD is a popular numerical method which solves the equation in the time domain and hence in a single simulation run can cover a wide frequency range. It solves the EM equations in a cyclic and iterative manner by solving the electric field in a given instant of time followed by the magnetic field in the next instant of time. This method has undergone many modifications since the days when it was introduced as a time-stepping algorithm in 1966 by Kane Yee [37]. Its popularity has increased exponentially from 1990s onwards as it was found to be the primary means to computationally model several scientific and engineering problems dealing with the interaction of EM waves with matter.

To formulate FDTD in general we begin by expressing a non-dispersive linear isotropic material employing Maxwell's equations. Equation (2.3) and (2.4) can be expressed as

$$\frac{\partial H}{\partial t} = -\frac{1}{\mu} \nabla \times E \quad (4.1)$$

$$\frac{\partial E}{\partial t} = \frac{1}{\varepsilon} \nabla \times H \quad (4.2)$$

The following six coupled scalar equations are obtained after the expansion of the components of the curl operators of (4.1) and (4.2) in Cartesian coordinates for a nonmagnetic medium (i.e.  $\mu = \mu_0$ ),

$$\frac{\partial E_z}{\partial y} - \frac{\partial E_y}{\partial z} = -\frac{\partial H_x}{\partial t} \quad (4.3)$$

$$\frac{\partial E_x}{\partial z} - \frac{\partial E_z}{\partial x} = -\frac{\partial H_y}{\partial t} \quad (4.4)$$

$$\frac{\partial E_y}{\partial x} - \frac{\partial E_x}{\partial y} = -\frac{\partial H_z}{\partial t} \quad (4.5)$$

$$\frac{\partial H_z}{\partial y} - \frac{\partial H_y}{\partial z} = \frac{\partial E_x}{\partial t} \quad (4.6)$$

$$\frac{\partial H_x}{\partial z} - \frac{\partial H_z}{\partial x} = \frac{\partial E_y}{\partial t} \quad (4.7)$$

$$\frac{\partial H_y}{\partial x} - \frac{\partial H_x}{\partial y} = \frac{\partial E_z}{\partial t} \quad (4.8)$$

The FDTD numerical algorithm uses arbitrary three-dimensional objects for modeling electromagnetic wave interactions and relies heavily on the scheme of six coupled partial differential equations (4.3)-(4.8). The Yee algorithm simultaneously solves the electric and magnetic fields of the wave equation in both time and space, rather than by solving for either the electric field or the magnetic field separately.

The generalized Yee's algorithm is a 3-Dimensional direct solution of Maxwell's equation in integral form. Yee's FDTD scheme [38] discretizes Maxwell's curl equations and solves the time and space first-order partial derivatives approximated by central differences using a leapfrog scheme.

### 4.3 Yee's Orthogonal Grid

Yee's 3-Dimensional grid was proposed for structured lattices and it requires three orthogonal meshes for the electric and magnetic field as shown in the figure 4-1.

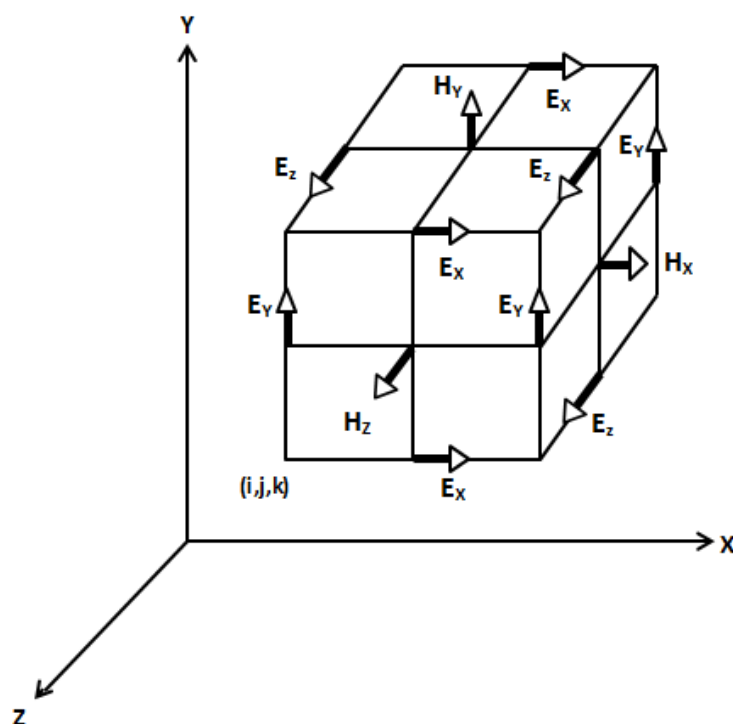


Figure 4 - 1: Yee's spatial grid.

It positions  $E$  and  $H$  components at the centers of the grid lines and surfaces such that each  $E$  component is surrounded by four  $H$  components, and vice versa. This provides a neat and simple image of 3-dimensional space being filled by interlinked arrays of Ampere's law and

Faraday's law contours. It can clearly be seen that H components associated with the magnetic flux are linked with the E loops and the E components associated with the displacement current flux are linked with the H loops.

Considering only 2-dimensional space (i.e. of x-y plane), and assuming no variation of the fields in the z-direction, it can be said that

$$\frac{\partial Hy}{\partial z} = 0, \frac{\partial Hx}{\partial z} = 0, \frac{\partial Ey}{\partial z} = 0, \frac{\partial Ex}{\partial z} = 0$$

Two independent sets of coupled equations are obtained using equation (4.3)-(4.8) as shown, where the TM polarized field is given as

$$\frac{\partial Ex}{\partial t} = \frac{1}{\epsilon} \frac{\partial Hz}{\partial y} \quad (4.9)$$

$$\frac{\partial Ey}{\partial t} = -\frac{1}{\epsilon} \frac{\partial Hz}{\partial x} \quad (4.10)$$

$$\frac{\partial Hz}{\partial t} = \frac{1}{\mu} \left( \frac{\partial Ex}{\partial y} - \frac{\partial Ey}{\partial x} \right) \quad (4.11)$$

And the TE polarized field is given as

$$\frac{\partial Hx}{\partial t} = -\frac{1}{\mu} \frac{\partial Ez}{\partial y} \quad (4.12)$$

$$\frac{\partial Hy}{\partial t} = \frac{1}{\mu} \frac{\partial Ez}{\partial x} \quad (4.13)$$

$$\frac{\partial Ez}{\partial t} = \frac{1}{\epsilon} \left( \frac{\partial Hy}{\partial x} - \frac{\partial Hx}{\partial y} \right) \quad (4.14)$$



The partial spatial derivatives in (4.9)-(4.11) can be approximated by a central difference approximation in space by utilizing Yee's spatial gridding scheme. For example, equations (4.9)-(4.11) respectively become

$$\frac{\partial E_x}{\partial t} = \frac{1}{\varepsilon} \frac{H_z(i, j) - H_z(i, j - 1)}{\Delta y} \quad (4.15)$$

$$\frac{\partial E_y}{\partial t} = -\frac{1}{\varepsilon} \frac{H_z(i, j) - H_z(i - 1, j)}{\Delta x} \quad (4.16)$$

$$\frac{\partial H_z}{\partial t} = \frac{1}{\mu} \left( \frac{E_x(i, j + 1) - E_x(i, j)}{\Delta y} - \frac{E_y(i + 1, j) - E_y(i, j)}{\Delta x} \right) \quad (4.17)$$

Central differencing in time for solving the E and H components is exploited again by the Yee's algorithm by using a leapfrog scheme as shown in Figure 4-2.

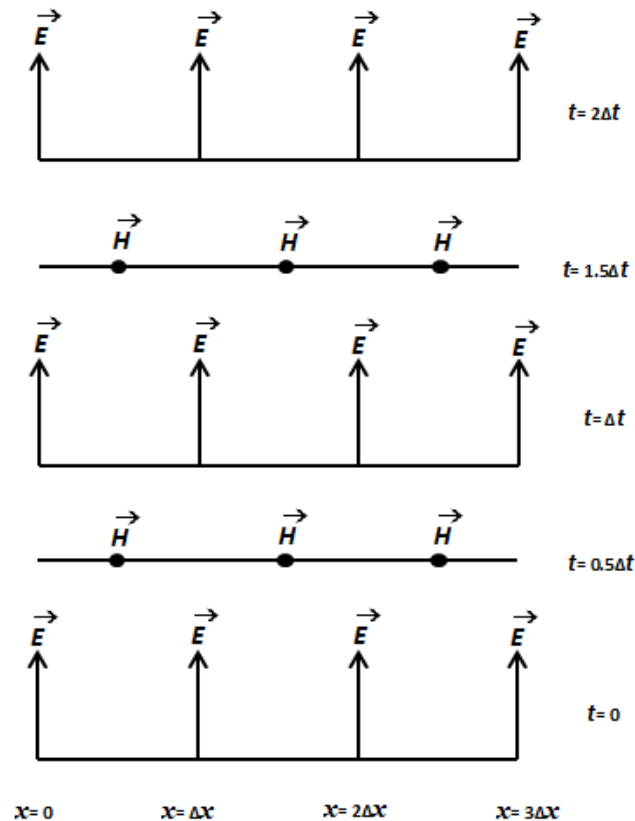


Figure 4 - 2: Leapfrog scheme: the temporal scheme of the FDTD method.

Utilizing the previously computed values of  $E$  and the newly computed  $H$  field data, all  $E$  components in the modeled space are computed and stored in memory for use in the next cycle. Similarly at each step, previously obtained  $H$  and the newly updated  $E$  are used to calculate the new  $H$ . This process continues until the time-stepping is completed.

After applying the central difference approximation, equations (4.15)-(4.17), become

$$\frac{E_x^{n+1}\left(i + \frac{1}{2}, j\right) - E_x^n\left(i + \frac{1}{2}, j\right)}{\Delta t} = \frac{1}{\varepsilon} \frac{H_z^{n+\frac{1}{2}}\left(i + \frac{1}{2}, j + \frac{1}{2}\right) - H_z^{n+\frac{1}{2}}\left(i + \frac{1}{2}, j - \frac{1}{2}\right)}{\Delta y} \quad (4.18)$$

$$\frac{E_y^{n+1}\left(i, j + \frac{1}{2}\right) - E_y^n\left(i, j + \frac{1}{2}\right)}{\Delta t} = -\frac{1}{\varepsilon} \frac{H_z^{n+\frac{1}{2}}\left(i + \frac{1}{2}, j + \frac{1}{2}\right) - H_z^{n+\frac{1}{2}}\left(i - \frac{1}{2}, j + \frac{1}{2}\right)}{\Delta y} \quad (4.19)$$

$$\begin{aligned} & \frac{H_z^{n+\frac{1}{2}}\left(i + \frac{1}{2}, j + \frac{1}{2}\right) - H_z^{n-\frac{1}{2}}\left(i + \frac{1}{2}, j + \frac{1}{2}\right)}{\Delta t} \\ &= \frac{1}{\mu} \left( \frac{E_x^n\left(i + \frac{1}{2}, j + 1\right) - E_x^n\left(i + \frac{1}{2}, j\right)}{\Delta y} - \frac{E_y^n\left(i + 1, j + \frac{1}{2}\right) - E_y^n\left(i, j + \frac{1}{2}\right)}{\Delta x} \right) \end{aligned} \quad (4.20)$$

It is required to set an upper limit to the time step,  $\Delta t$ , to ensure the numerical stability of the Yee algorithm, in accordance with spatial increment  $\Delta x$ ,  $\Delta y$ , and  $\Delta z$ . This is in perfect agreement with the Courant-Friedrich-Levy (CFL) stability condition [38]. In three dimensions, the CFL condition is

$$\Delta t \leq \Delta t_{max} = \frac{1}{c \sqrt{\frac{1}{\Delta x^2} + \frac{1}{\Delta y^2} + \frac{1}{\Delta z^2}}} \quad (4.21)$$

The stability of the algorithm is guaranteed through the upper bound on  $\Delta t$ . This stability criterion enables successful application of FDTD method to a wide variety of electromagnetic wave modeling problems.

## 4.4 Material dispersion in the FDTD

The FDTD method is widely used for solving Maxwell's equations as it is intuitive and the most versatile modeling technique, aiding the user to fully comprehend what to be expected out of a given model. It allows the user to define the material properties at all points within the computational domain. Hence modeling of wide variety of (both electrical and magnetic) material characteristics such as linearity, dispersion and nonlinearity is extremely easy. As most of the dielectrics and metals are dispersive, modeling dispersive materials in the FDTD requires familiarity of the user with the subject. The discussion of this topic was dealt with in chapter 3. The three main methods to model dispersive materials in the FDTD are

1. The recursive convolution (RC) method.
2. The auxiliary differential equation (ADE) method.
3. The Z-transform method.

In this chapter, the ADE dispersive FDTD method will be discussed in detail and applied to model metals and dielectric materials.

### 4.4.1 Auxiliary Differential Equation

Allen Taflove [33] first proposed the auxiliary differential equation to introduce dispersion relation in the FDTD. A more general representation of the dispersion relation is given by the ADE method due to its high flexibility in fitting arbitrary permittivity functions [37]. For finding new  $E$  field from the previous value of  $E$  and  $D$ , Taflove came up with an idea to convert the dispersion relation from the frequency domain to the time domain employing Fourier transforms technique. Beginning with the frequency domain relationship to get a time domain relation between  $D$  and  $E$  in a dispersive medium, we write

$$D(\omega) = \varepsilon_o \frac{\sigma}{j\omega} E(\omega) \quad (4.22)$$

which can be simplified to

$$j\omega D(\omega) = \varepsilon_o \sigma E(\omega) \quad (4.23)$$

By applying inverse Fourier transform the above equation becomes

$$\frac{dD(t)}{dt} = \varepsilon_o \sigma E(t) \quad (4.24)$$

Discretizing the above relation using forward difference scheme

$$\frac{D^{n+1} - D^n}{\Delta t} = \varepsilon_o \sigma E^{n+1} \quad (4.25)$$

So the updated  $E$  will be

$$E^{n+1} = \frac{D^{n+1} - D^n}{\varepsilon_o \sigma \Delta t} \quad (4.26)$$

### 4.4.2 The General Algorithm

The equation for a single-pole dispersion relation is simple to derive. But for a multi-pole dispersion relation, the equation becomes difficult to derive and it gets more complicated with lengthy derivations and computation for a six-pole Lorentz-Drude dispersion model. Taflove proposed matrix inversion to solve for multi-poles which requires a large computational time and a large memory. It was Alsunaidi and Al-Jabr [39], who proposed the general algorithm technique to solve these problems. It is proposed that only one algorithm is required for any dispersion relation as a result of the ADE method. The dispersive relation has the general form;

$$D(\omega) = \varepsilon(\omega)E(\omega) \quad (4.27)$$

This can be expressed as the form of equation (3.3)

$$D(\omega) = \varepsilon_0 \varepsilon_\infty E(\omega) + \sum_i^N P_i(\omega) \quad (4.28)$$

where,  $N$  represents the number of poles. On applying the inverse Fourier transform, the discretized form of the equation (4.27) becomes

$$D^n = \varepsilon_0 \varepsilon_\infty E^n + \sum_i^N P_i^n \quad (4.29)$$

Solving for  $E$  gives

$$E^n = \frac{D^n - \sum_i^N P_i^n}{\varepsilon_0 \varepsilon_\infty} \quad (4.30)$$

The procedure for the evaluation of the time-domain polarization is as follows. The polarization field for Lorentz model in the frequency domain can be written as

$$P(\omega) = \frac{a}{b + jc\omega - d\omega^2} E(\omega) \quad (4.31)$$

Applying inverse Fourier transform to Eqn. 4.3 gives

$$bP(t) + cP'(t) + dP''(t) = aE(t) \quad (4.32)$$

Writing the derivatives at time instant  $n-1$  gives

$$bP^{n-1} + c \frac{P^n - P^{n-2}}{2\Delta t} + d \frac{P^n - 2P^{n-1} + P^{n-2}}{\Delta t^2} = aE^{n-1} \quad (4.33)$$

Rearranging and solving for  $P^n$  in terms of  $P^{n-1}$ ,  $P^{n-2}$  and  $E^{n-1}$  gives

$$P^n = \frac{4d - 2b\Delta t^2}{2d + c\Delta t} P^{n-1} + \frac{-2d + c\Delta t}{2d + c\Delta t} P^{n-2} + \frac{2a\Delta t^2}{2d + c\Delta t} E^{n-1} \quad (4.34)$$

The calculation of Polarization is given by

$$P^n = C_1 P^{n-1} + C_2 P^{n-2} + C_3 E^{n-1} \quad (4.35)$$

Where  $C_1$ ,  $C_2$ ,  $C_3$  are given as

$$C_1 = \frac{4d - 2b\Delta t^2}{2d + c\Delta t}, \quad C_2 = \frac{-2d + c\Delta t}{2d + c\Delta t}, \quad C_3 = \frac{2a\Delta t^2}{2d + c\Delta t}$$

For the 6-pole Lorentz-Drude model the values of  $C_1$ ,  $C_2$  and  $C_3$  are different for different materials. These constants can be found for any form of dispersion relation of  $E$  and  $D$ . In table 4-1 [37] the general constants for some possible models are given.

Table 4 - 1: Algorithm constant:  $C_1$ ,  $C_2$  and  $C_3$  for different dispersion relation models.

<b>Polarization term in Frequency domain</b>	$C_1$	$C_2$	$C_3$
<b>Lorentz Pole</b> $P(\omega) = \frac{a}{b + jc\omega - d\omega^2} E(\omega)$	$\frac{4d - 2b\Delta t^2}{2d + c\Delta t}$	$\frac{-2d + c\Delta t}{2d + c\Delta t}$	$\frac{2a\Delta t^2}{2d + c\Delta t}$
<b>Drude Pole</b> $P(\omega) = \frac{a}{jc\omega - d\omega^2} E(\omega)$	$\frac{4d}{2d + c\Delta t}$	$\frac{-2d + c\Delta t}{2d + c\Delta t}$	$\frac{2a\Delta t^2}{2d + c\Delta t}$
<b>Plasma frequency</b> $P(\omega) = \frac{a}{\omega^2} E(\omega)$	2	-1	$2a\Delta t^2$
<b>Debye term</b> $P(\omega) = \frac{a}{b + jc\omega} E(\omega)$	$\frac{-2b\Delta t}{c}$	1	$\frac{2a\Delta t}{c}$
<b>Conductivity term</b> $P(\omega) = \frac{a}{jc\omega} E(\omega)$	0	1	$\frac{2a\Delta t^2}{2d + c\Delta t}$

The algorithm can be illustrated using the following flow chart:

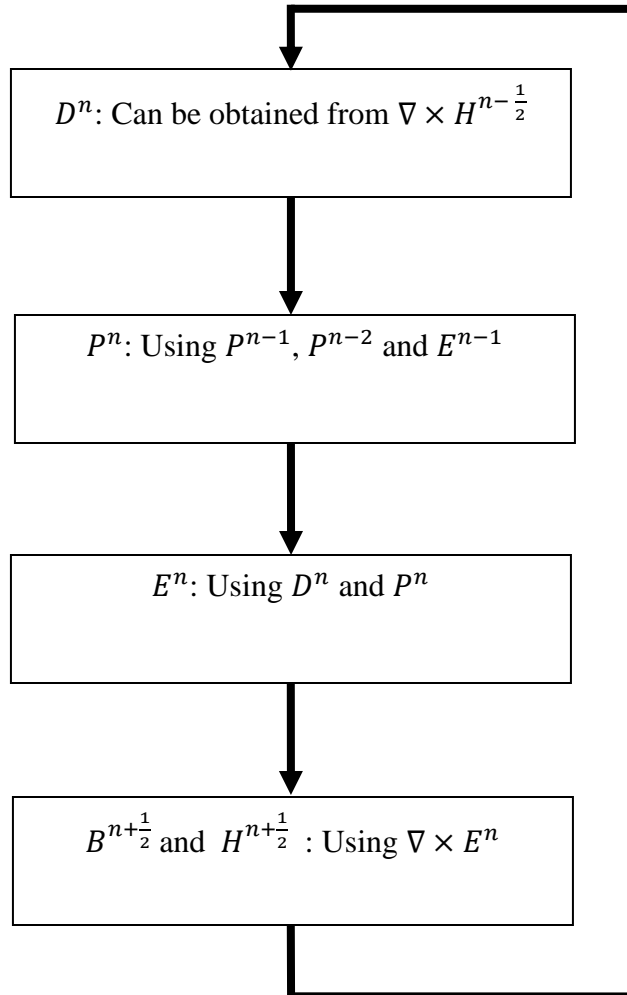


Figure 4 - 3: FDTD algorithm for linear dispersive case.



## 4.5 Integrating Third Order Non-linear Susceptibility $\chi^{(3)}$ into the General Algorithm

Further elaborating the ADE-FDTD [37] algorithm, this thesis models  $\text{As}_2\text{S}_3$  chalcogenide glass which is a non-linear dispersive material, using a multi-pole Lorentz model. The details of the Lorentz model are described in chapter 3. From equation (3.67) and (3.68) we have

$$s(\omega) = \chi_R^{(3)}(\omega) FT\{E^2(t)\} \quad (4.36)$$

where  $FT$  represents the Fourier transform.

$\chi_R^{(3)}(\omega)$  can be written as

$$\chi_R^{(3)}(\omega) = \frac{A\omega_R^2}{\omega_R^2 - 2j\omega\delta_R - \omega^2} \quad (4.37)$$

Equation (4.36) can be written to

$$s(\omega) = \frac{A\omega_R^2}{\omega_R^2 - 2j\omega\delta_R - \omega^2} FT\{E^2(t)\} \quad (4.38)$$

This can be further simplified as

$$[\omega_R^2 - 2j\omega\delta_R + (j\omega)^2]s(\omega) = A\omega_R^2 FT\{E^2(t)\} \quad (4.39)$$

In the time domain, the above equation takes the form

$$\omega_R^2 s(t) - 2\delta_R \frac{ds(t)}{dt} + \frac{d^2s(t)}{dt^2} = A\omega_R^2 E^2(t) \quad (4.40)$$

Now for any time instant  $n\Delta t$  the updated equation of  $s$  can be obtained by approximating the time derivatives in (4.38) as a result the update equation becomes

$$s^n = C_{11}S^{n-1} + C_{22}S^{n-2} + C_{33}E^{2^{n-1}} \quad (4.41)$$

where,

$$C_{11} = \frac{4d - 2b\Delta t^2}{2d + c\Delta t}, \quad C_{22} = \frac{-2d + c\Delta t}{2d + c\Delta t}, \quad C_{33} = \frac{2a\Delta t^2}{2d + c\Delta t} E^n$$

$$a = (1 - \alpha)\varepsilon_o\chi^{(3)}(\omega_R^2), \quad b = \omega_R^2, \quad c = 2\delta_R, \quad d = 1$$

Using equation (3.62) the update equation for polarization can be expressed as

$$P_{NL(3)}^n = \alpha_k (E^n)^3 + s^n E^n \quad (4.42)$$

Then the updated value of the electric flux density is

$$D^n = \varepsilon_o \varepsilon_\infty E^n + P_{LN(1)}^n + \alpha_k (E^n)^3 + s^n E^n \quad (4.43)$$

Solving for  $E^{n+1}$ , the following equation is obtained

$$A_k (E^n)^3 + B_k (E^n)^2 + C_k E^n + D_k = 0 \quad (4.44)$$

where,

$$A_k = 1, \quad B_k = 0, \quad C_k = \frac{(s^n + \varepsilon_o \varepsilon_\infty)}{\alpha \varepsilon_o \chi^{(3)}}, \quad D_k = \frac{P_{LN(1)}^n - D^n}{\alpha \varepsilon_o \chi^{(3)}}$$

Equation (4.44) is a cubic equation in  $E^n$  with real solution given by

$$E^n = \left( -\frac{D_k}{2} + \sqrt{\left(\frac{C_k}{3}\right)^3 + \left(\frac{D_k}{2}\right)^2} \right)^{\frac{1}{3}} + \left( -\frac{D_k}{2} - \sqrt{\left(\frac{C_k}{3}\right)^3 + \left(\frac{D_k}{2}\right)^2} \right)^{\frac{1}{3}} \quad (4.45)$$

The algorithm to calculate the updated  $E$  and  $H$  can be explained using following flow chart.

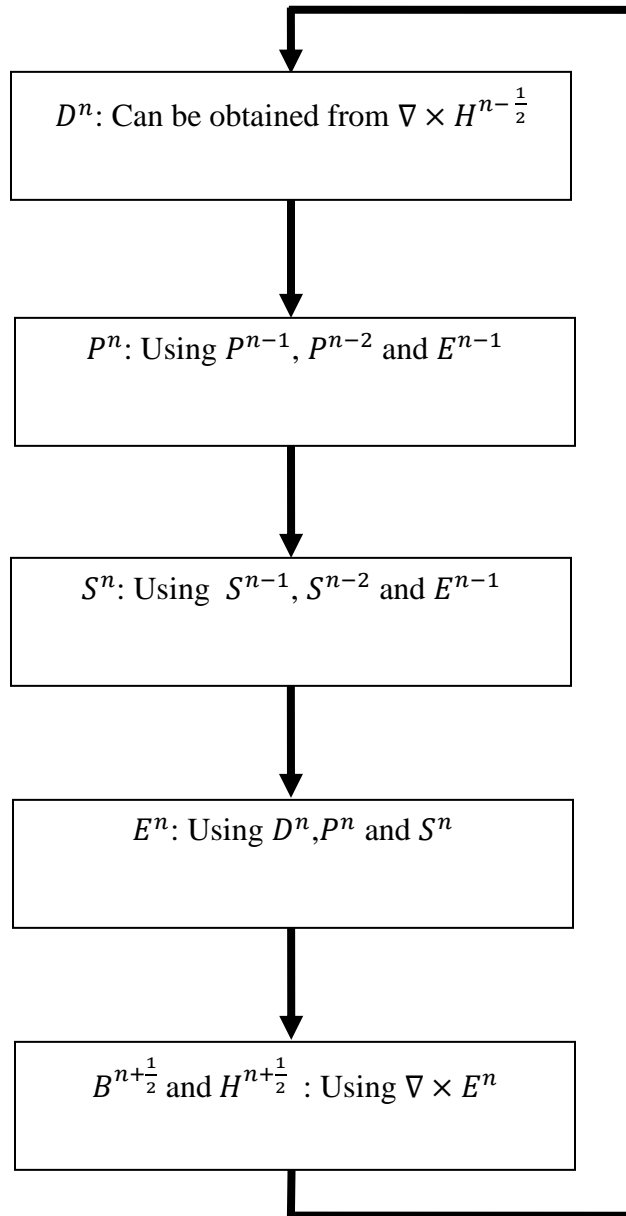


Figure 4 - 4: FDTD algorithm for nonlinear dispersive case.

## CHAPTER 5

# INVESTIGATION OF SPP MODULATION

### 5.1 Simulator Verification

The primary purpose of computer based simulation and numerical modeling is to aid in speeding up the development of critical projects and to reduce the resources required for its implementation, completion and accurate verification. Moreover it helps to replicate those theoretical behaviors which cannot be reproduced in the laboratory. It acts as prototype model for detail investigation even before executing experiments. They help in understanding complex internal functioning of a system which otherwise cannot be gauged by carrying out the experimental work or purely analytical means. Hence, the accuracy of the simulator is extremely essential for having a reliable and useful solution. Before using any newly developed simulator, it is important to verify the simulator with other methods such as analytical solutions or with the experimental results to minimize errors.

In this thesis, the non-linear dispersive material:  $\text{As}_2\text{S}_3$  chalcogenide glass is used to modulate SPPs by pumping high intensity light signals. The simulator (for non-linear dispersive behavior of  $\text{As}_2\text{S}_3$  chalcogenide glass) and the dispersion relation of the material for different wavelengths were verified through comparison with published results by Sagor et al [40].

## 5.2 Technique used for Testing the Algorithm for Non-linear Dispersive Material

In order to test the algorithm for non-linear dispersive material, we calculated the one-dimensional temporal solitons using the data given by Taflove [33]. The material was considered to have a linear and non-linear susceptibility function  $\chi^{(1)}$  and  $\chi^{(3)}$  respectively.

The linear susceptibility parameters used in the simulator is as follows

$$\chi^{(1)}: \quad \varepsilon_s = 5.25, \quad \varepsilon_\infty = 2.24, \quad \omega_o = 4 \times 10^{14} s^{-1}, \quad \delta = 2 \times 10^9 s^{-1}$$

The non-linear susceptibility parameters are:

$$\chi^{(3)}: \text{ non-linear co-efficient, } \chi_o^{(3)} = 7 \times 10^{-2} (v/m)^{-2},$$

Lorentz relaxation times,  $\tau_1 = 12.2 fs$  and  $\tau_2 = 32 fs$

A 50-fs optical pulsed signal source was used at  $t=0$  at the surface  $x=0$ .

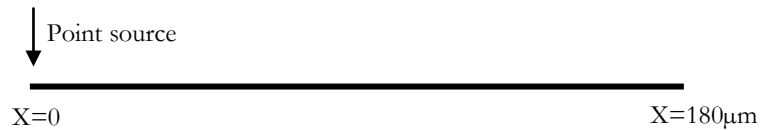


Figure 5 - 1: 1-D structure to solve non-linear dispersive material of Taflove [33].

The  $E$  signal having unity amplitude multiplied by a hyperbolic secant temporal envelope with a carrier frequency  $f_c = 1.37 \times 10^{14} Hz$  was pumped into the simulator. The spatial step size  $\Delta x$  was set at 5 nm and the propagating pulse was visualized at 20,000 and 40,000 time steps which correspond to 55  $\mu m$  and 126  $\mu m$  at time 487 fs and 973 fs. The simulated

results for their developed simulator, gave a very good agreement with the published results [33]. It was observed that the pulse undergoes spatial broadening due to material dispersion as shown in figure 5-2.

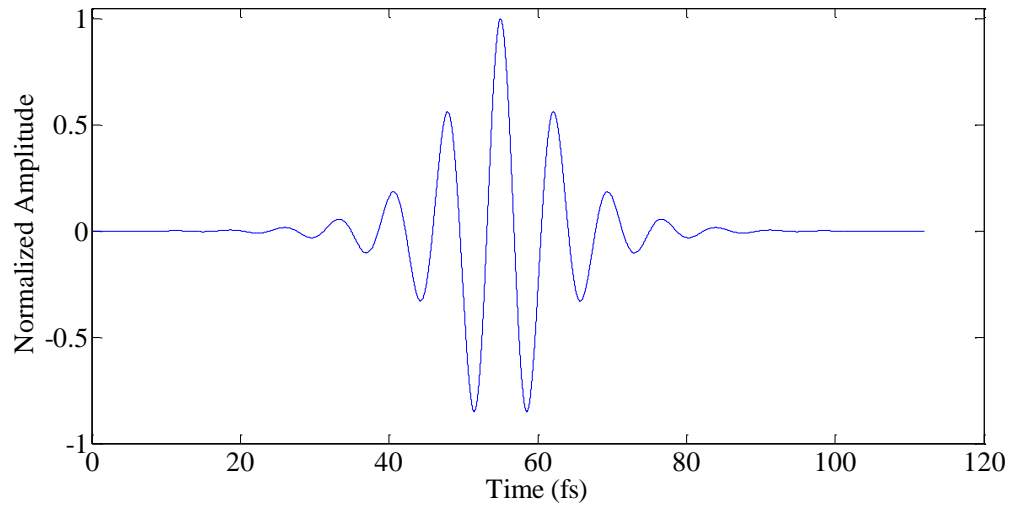
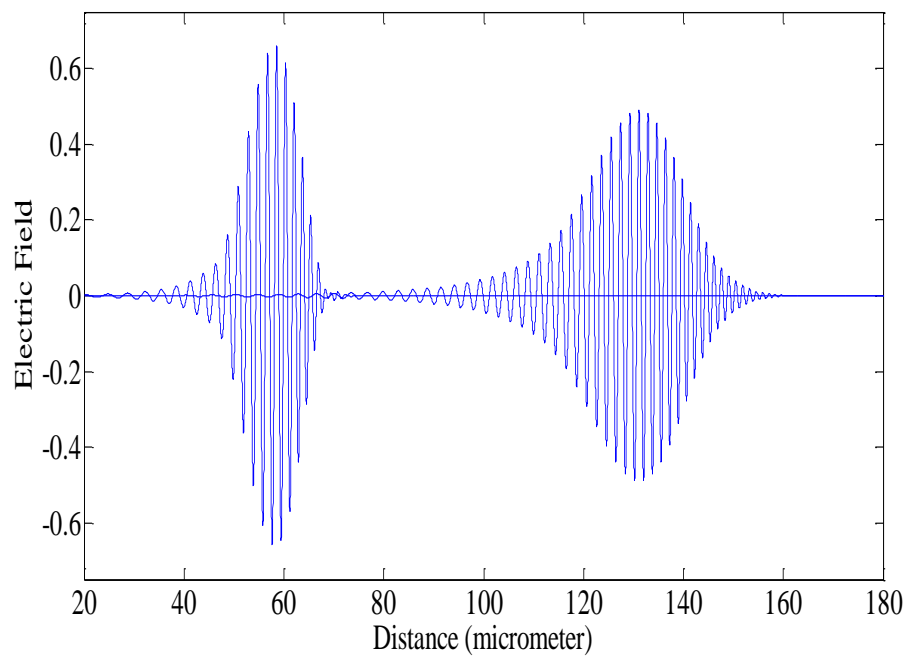
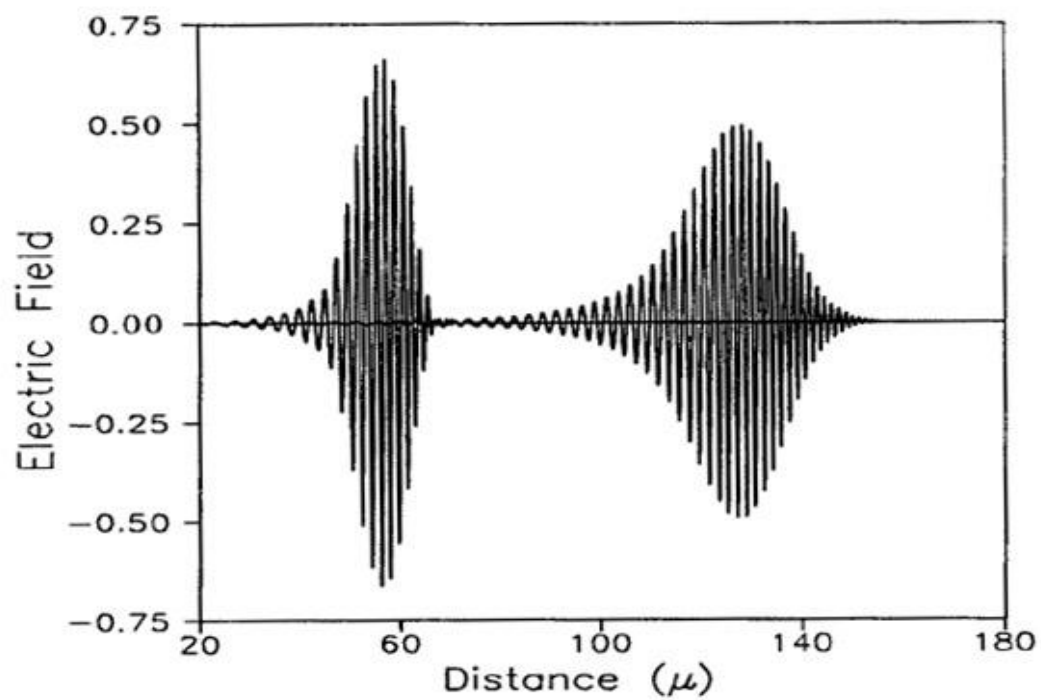


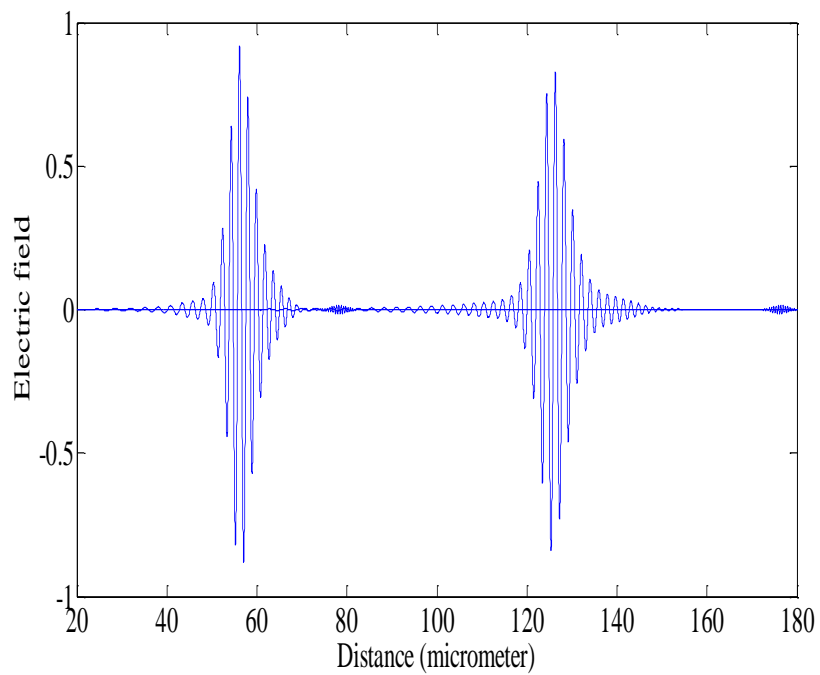
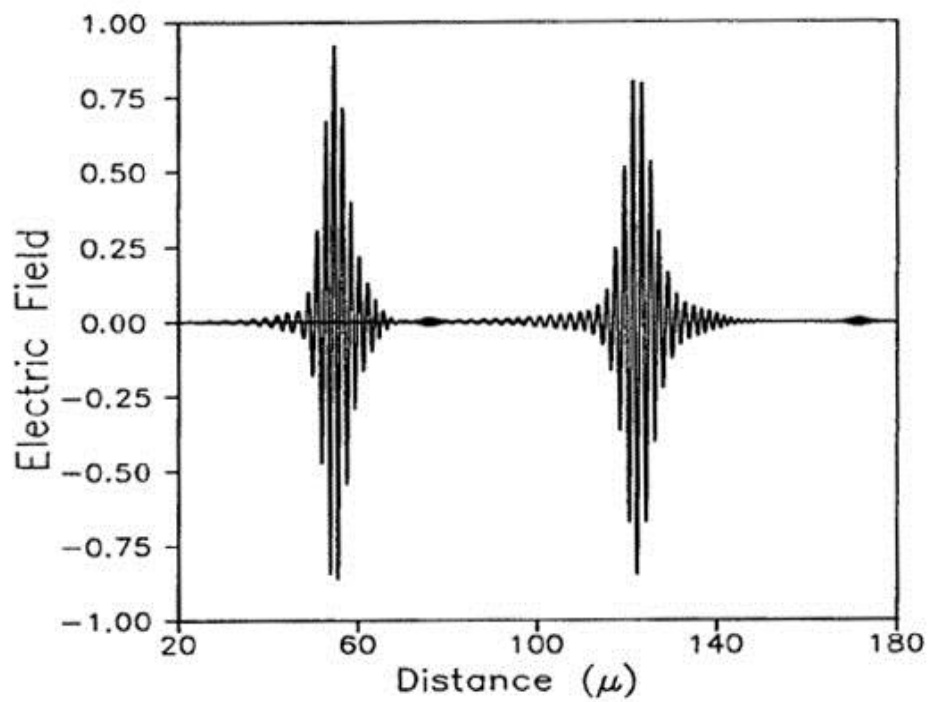
Figure 5 - 2: Input pulse in the time domain.

Figure 5-3 corresponds to the linear dispersive case showing the attenuation, broadening and frequency modulation effects of anomalous dispersion. Figure 5-4 corresponds to the results for the nonlinear dispersive case showing the formation of solitons.



(b)

Figure 5 - 3: ADE-FDTD simulation result for linear Lorentz dispersive material at the time of 487fs and 973fs. (a) Published result [33] (b) Simulated result.



(b)

Figure 5 - 4: ADE-FDTD simulation result for linear Lorentz dispersive material at the time of 487fs and 973fs. (a) Published result[10] (b) Simulated result.



### 5.3 Dispersion Relation of Chalcogenide Glass

Moreover Sagor et al [40] modeled the linear dispersion relation for chalcogenide glass based on the published experimental data by Zsolt L. Sámson et al [41]. The Optical Kerr coefficient  $n_2$  of ChG was derived as  $n_2 = 5.56933 \times 10^{-17} \text{ m}^2/\text{W}$  and the non-linear coefficient non-linear coefficient as,  $\chi_o^{(3)} = 7.530623 \times 10^{-19} (v/m)^{-2}$ .

The material was assumed to have the general Lorentz dispersion relation in the form of

$$\varepsilon_r(\omega) = \varepsilon_\infty + \frac{(\varepsilon_s - \varepsilon_\infty)\omega_0^2}{\omega_0^2 + 2j\omega\delta - \omega^2} \quad (5.1)$$

The parameters chosen for fitting were as follows

The static value of dielectric constant,  $\varepsilon_s = (2.257)^2$

Optical value of dielectric constant,  $\varepsilon_\infty = 2.7$

Material resonance frequency,  $\omega_0 = 7 \times 10^{15} \text{ rad/sec}$ .

Damping factor,  $\delta = 8 \times 10^{11} \text{ rad/sec}$ .

Excellent agreement for both real part and imaginary part of the frequency dependent dielectric constant was obtained for range of wavelength varying from 400 nm to 1600 nm. Hence, we use this established and verified model in this thesis. Dispersion relation for both fitting result and experimental result are shown in figure 5-5.

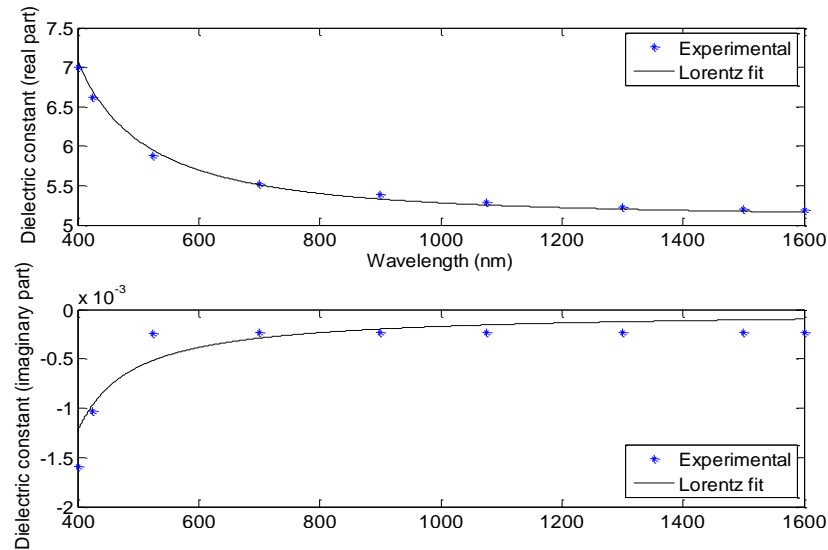


Figure 5 - 5: The dispersion relation of ChG glass.

## 5.4 Testing the Algorithm for Plasmonic Structure

The detailed theory of SPPs was covered in the literature. As SPPs play key role in modulation of another SPP which may be acting as information carrier, it is essential that its detailed behavior and important characteristic properties such as penetration depth in dielectric and normalized SPP wavelength be studied. Hence the behavior of SPPs for various input wavelengths is tested. The results of the tested algorithm for different simulated SPP parameters will be compared with the corresponding theoretical values.

The basic structure that is used for simulator verification is shown in figure 5-6. The following subsections demonstrate the verification of plasmonic algorithm for the simulator. Figure 5-6 shows a silver film of 0.3 width  $\mu\text{m}$  and 12.5  $\mu\text{m}$  length has been taken to test the propagation of SPP and various length scales for an Air-Ag interface.

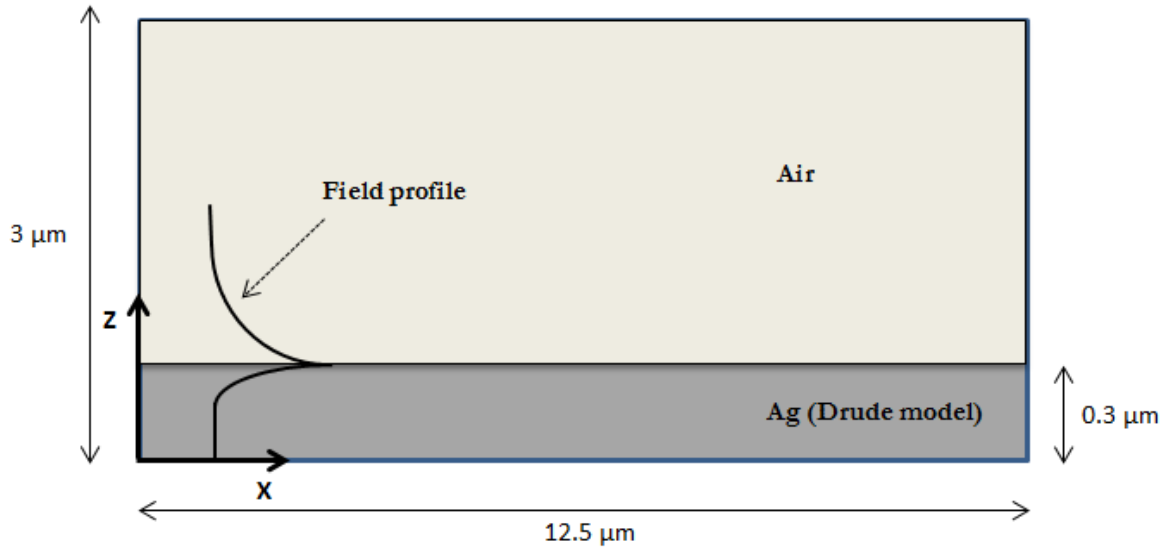


Figure 5 - 6: The dielectric metal structure considered for the simulator verification.

The Ag film is modeled using 1-pole Drude model having plasma frequency,  $\omega_p = 1.2 \times 10^{16} \text{ rad s}^{-1}$  and damping constant  $\Gamma = 1.45 \times 10^{13} \text{ s}^{-1}$ . The relative permittivity of dielectric was taken to be equal to 1.

One of the SPPs was generated by introducing the Plasmon mode taken from a previously travelling SPP and then multiplied by a cosine wave having various wavelengths ranging from 400 nm to 1600 nm. The resulting signal was multiplied with a Gaussian envelope having a pulse width of 50 fs. Figure 5-7 shows a snapshot of the  $E_z$  profile of SPP propagation after 34 fs.

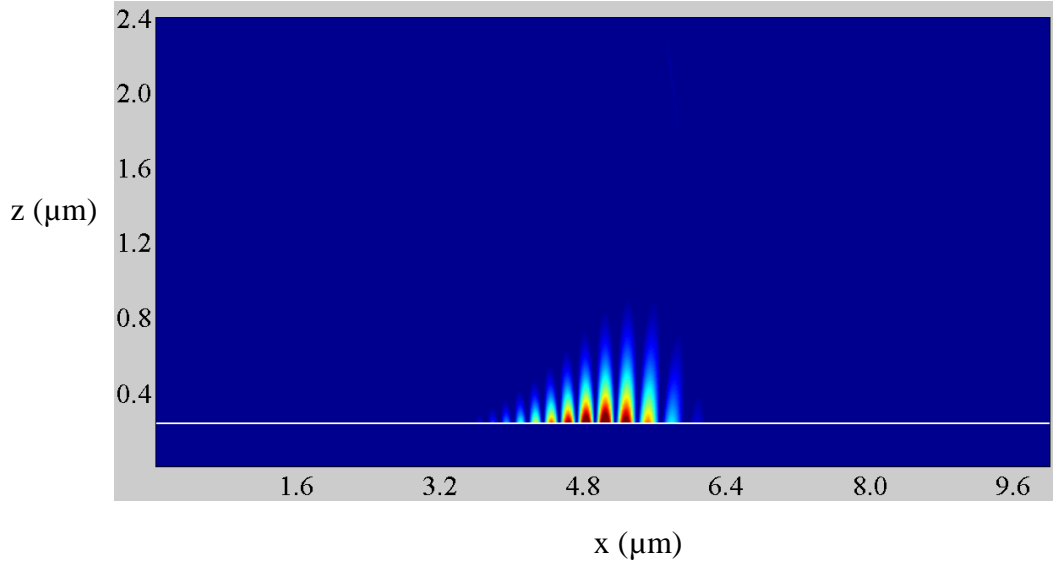


Figure 5 - 7: Snapshot of  $E_z$  profile of SPP propagating along a Metal-Dielectric interface.

### 5.4.1 The Normalized SPP wavelength

The SPP wavelength,  $\lambda_{SPP}$  is given by [42]

$$\lambda_{SPP} = \lambda_o \sqrt{\frac{\epsilon_d + \epsilon'_m}{\epsilon_d \epsilon'_m}} \quad (5.2)$$

It is assumed that the  $|\epsilon'_m| \gg |\epsilon''_m|$ .

The normalized wavelength  $\lambda_{SPP}/\lambda_o$  is given by

$$\frac{\lambda_{SPP}}{\lambda_o} = \sqrt{\frac{\epsilon_d + \epsilon'_m}{\epsilon_d \epsilon'_m}} \quad (5.3)$$

where,

$\lambda_o$  is the free space wavelength;

$\epsilon_d$  is the relative permittivity of the dielectric

$\epsilon'_m$  is the real part of the complex relative permittivity of the metal.

The normalized wavelength can be calculated by taking the distance between two consecutive peaks. The permittivity of both the dielectric and metal (Ag film is modeled using 1-pole Drude model), are known. So, theoretical values of the normalized wavelength can be calculated using equation (5.3). This method is applied for our case and figure 5-4 shows an excellent agreement for theoretical and simulated results.

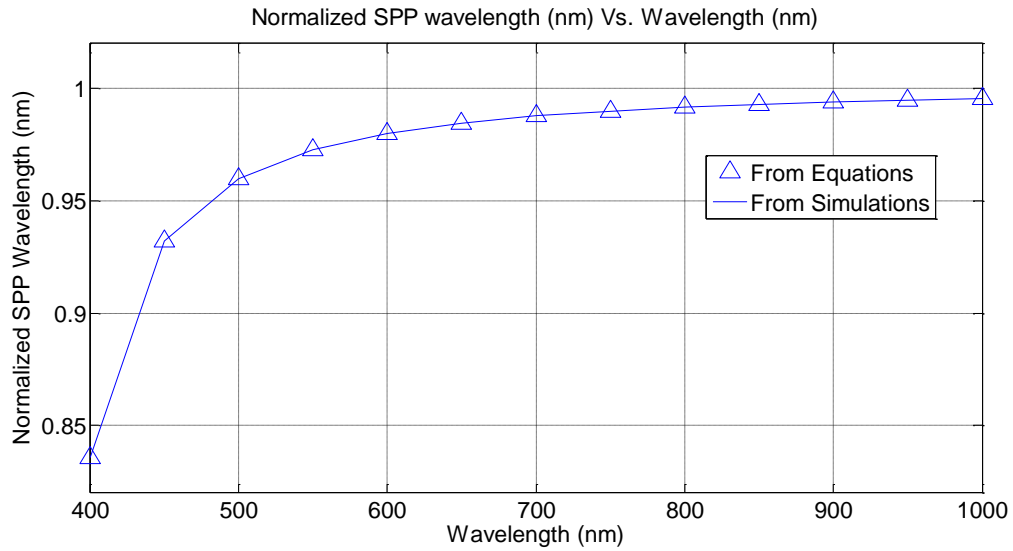


Figure 5 - 8: Normalized SPP wavelength at different free space wavelength.

### 5.4.2 The SPP field penetration depth

The penetration of the field into the materials bounding the interface can be expressed in terms of the relative permittivity of both metal and dielectric. The penetration depths into the dielectric,  $\delta_d$  and metal,  $\delta_m$ , are expressed as [39]

$$\delta_d = \frac{1}{k_o} \left| \frac{\epsilon_d + \epsilon'_m}{\epsilon_d^2} \right|^{\frac{1}{2}} \quad (5.4)$$

$$\delta_m = \frac{1}{k_o} \left| \frac{\epsilon_d + \epsilon'_m}{\epsilon_m^2} \right|^{\frac{1}{2}} \quad (5.5)$$

where,

$$k_o = \text{wavevector for light in free space} = \frac{2\pi}{\lambda_o}$$

Figure 5-5 shows the penetration depth of Electromagnetic (EM) field into Air with respect to change in Wavelength. It can be seen that the penetration depth of EM field (or the tail of the SPP) increases with the increase in wavelength. This figure gives the minimum dimension of the dielectric to be chosen to allow the SPP to fully develop and propagate into the desired device.

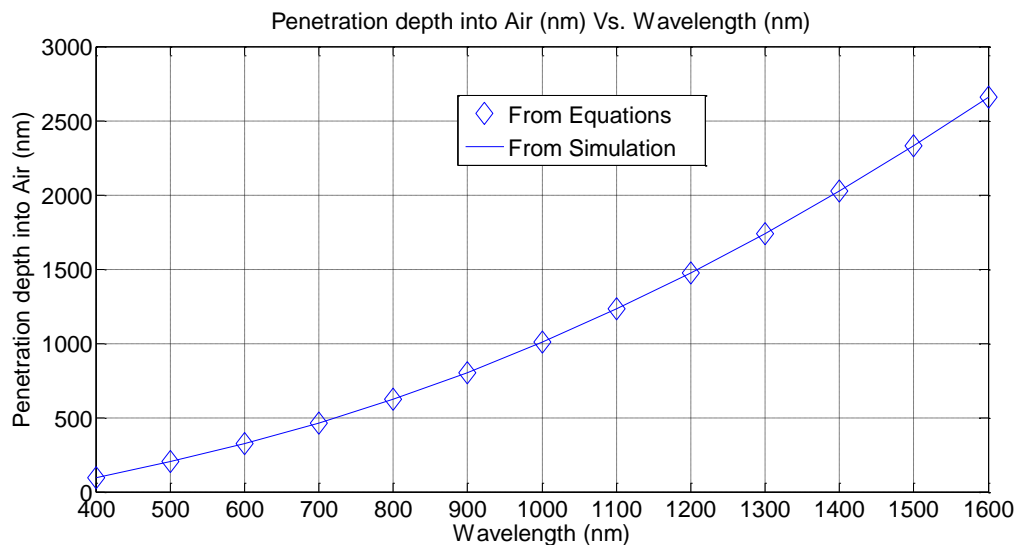


Figure 5 - 9: Penetration depth of SPP into air versus wavelength.

This penetration depth of the SPP field was verified using the data from the simulated results and the equations outlined above. The verification was done for the penetration depth in the dielectric and figure 5-5 shows a very good agreement between the analytical and simulated results.

# CHAPTER 6

## SIMULATION RESULTS FOR MODULATION OF SURFACE PLASMON POLARITONS

Various techniques to modulate the SPPs are presented in this chapter. Each device is unique and the modulation of SPPs obtained in each device is documented. The detailed geometry, dimensions, source used to excite the control signal and the test signal is discussed in details. It is shown here that the third-order non-linear Chalcogenide glass under the excitation of high intensity light source facilitates the modulation of SPPs by exciting Kerr non-linear characteristics of the glass and thus affecting the plasmonic wave in an interesting way.

### 6.1 General Pulse Characteristics

Before discussing the structure of various devices it would be appropriate to discuss the general pulse characteristics and the frequency range at which the Chalcogenide glass will be operated.

In all the devices the input and the control source field will be sent with either a Gaussian Pulse or a Continuous Wave Gaussian function with a carrier wavelength of 1064 nm, which corresponds to the wavelength of YAG laser. Initially the input source pulse was generated

having unity amplitude and subsequently the amplitude was increased in order to reach desired input intensity levels. Figure 6-1 and 6-2 show the source pulse in time domain and frequency domain respectively.

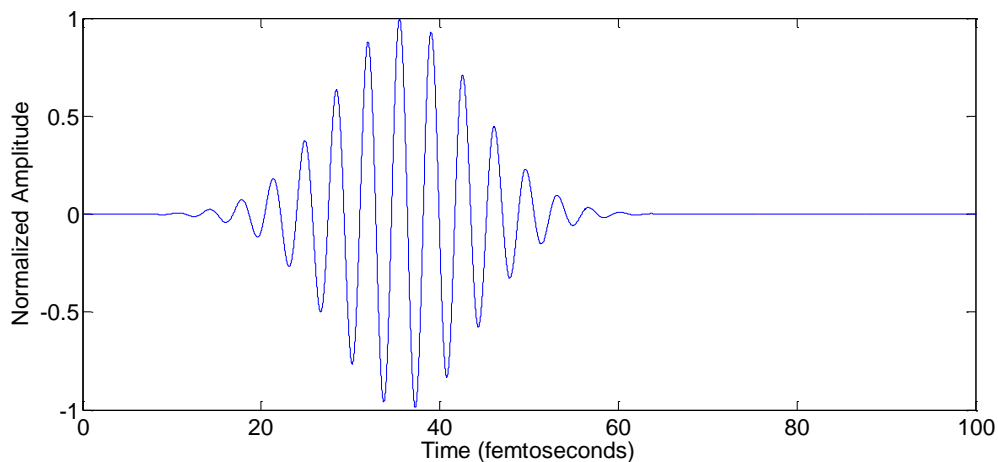


Figure 6 - 1: Input Pulse in the time domain

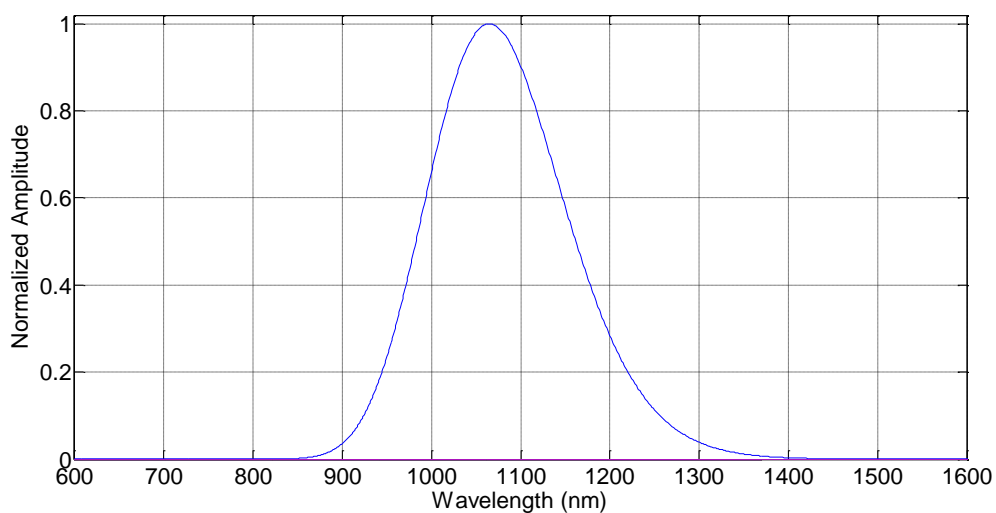


Figure 6 - 2: Input pulse in the wavelength domain

It is reported by Sagor et al [40] that the Chalcogenide glass begins to exhibit non-linear effects at high input intensities beyond  $6 \times 10^8$  V/m. It is in and around this range that the



devices are operated to observe for any modulation effect being displayed by the Plasmonic waves. The modulation can be observed either by recording the amplitudes, phase, frequency or power profile of the devices.

## 6.2 Metal-Waveguide Structure

The first device to be tested for modulation of SPPs is a Metal-Waveguide structure. The interaction between the Waveguide mode and the Continuous Wave (CW) SPP is analyzed by recording the power and intensity profile of the CW SPP at the output. To begin the discussion on the Metal-Waveguide structure we start with detailed model description as follows.

### 6.2.1 Model Description

The basic outlay of the Metal-Waveguide structure is as shown in figure 6-3. It consists of a Silver metal film of thickness 272 nm. The thickness was chosen such that the CW plasmon travelling on one side of the metal doesn't couple to the other side. A waveguide is modeled orthogonal to the silver metal surface as shown in the figure. The core of the waveguide is made up of Chalcogenide glass ( $\text{As}_2\text{S}_3$ ) having thickness of about 400 nm. The core of the waveguide is flanked on either side by a dispersive material of refractive index 1.7 and hence acts as cladding. The dimension of each cladding material is 1  $\mu\text{m}$ . The length of the device is 8  $\mu\text{m}$  and its width is 2.4  $\mu\text{m}$  as shown in the figure 6.3. The Metal-Waveguide structure is aligned such that its length is along the z-axis and width along x-axis.

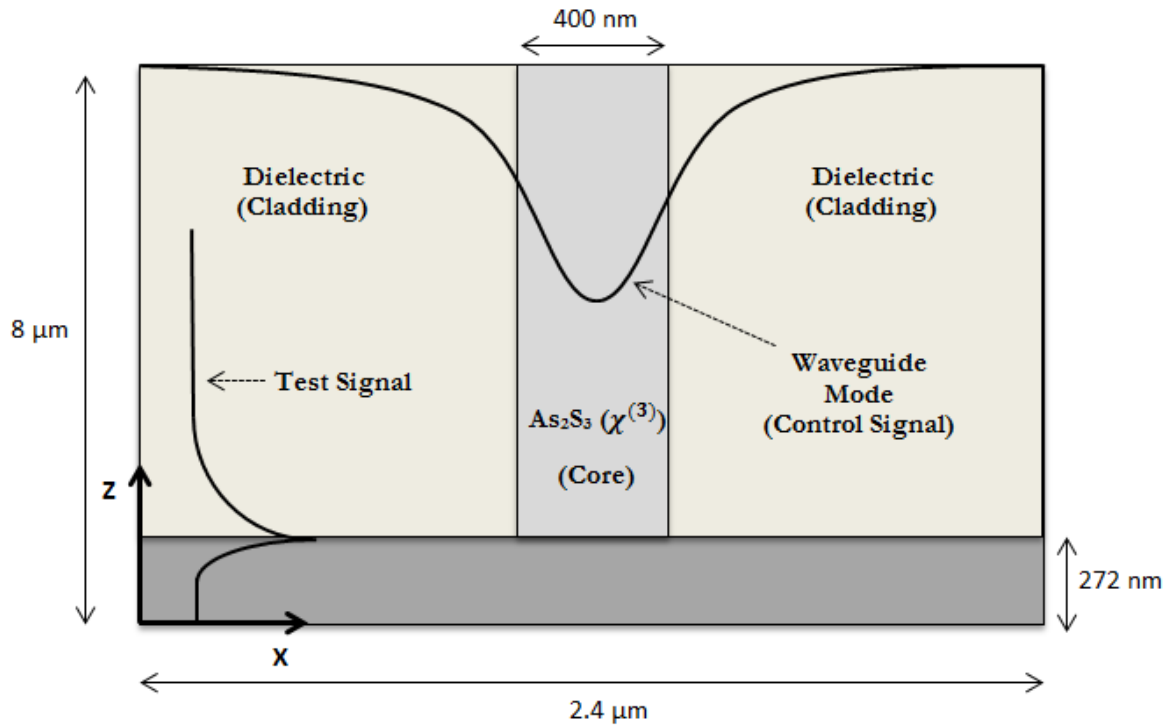


Figure 6 - 3: Block diagram of Metal-Waveguide structure.

The Ag metal acts as a perfect reflector to the mode propagating in the waveguide. The device is modeled such that it is surrounded by a Perfectly Matched Layer (PML) on all sides to reduce interference due to reflection of the signals from the boundaries.

## 6.2.2 Input Source

The biggest challenge in modeling the metal-waveguide device is to obtain fundamental mode for the waveguide. The refractive index of cladding is 1.7 and that of the core is 2.257. In this model, the algorithm developed by Muller for obtaining the fundamental mode of waveguide from certain set of parameters such as the operating wavelength of the waveguide, dimensions and refractive indices of core and cladding is employed. For the above mentioned set of refractive indices the waveguide effective index is found to be 2.045473564990815.

Based on the Muller's algorithm, it was finally possible to obtain the fundamental mode for the device as shown in figure 6-4. This fundamental mode of unity amplitude can be later increased to the desired intensity level as and when required.

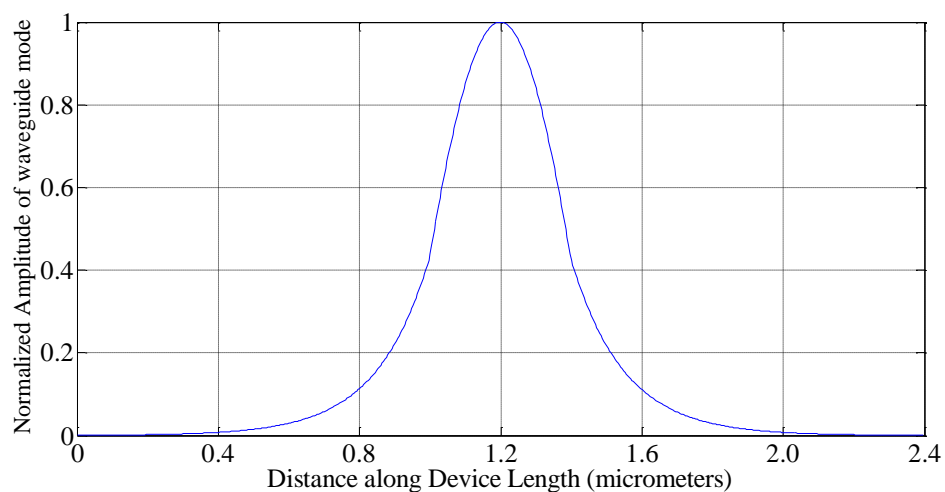


Figure 6 - 4: The normalized fundamental mode of the waveguide pumped into the device

Similarly the plasmon mode is obtained by taking the cross-section profile of a plasmon that propagates along the metal surface as shown in Figure 6-5.

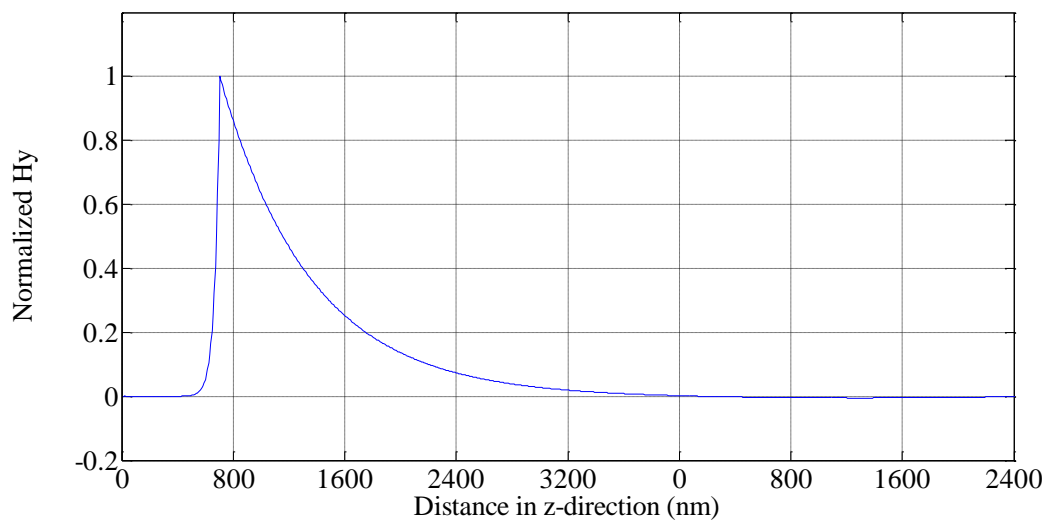


Figure 6 - 5: The normalized Hy field profile pumped in the device.

Figure 6-5 shows the  $H_y$  field profile of SPP mode of unity amplitude. The amplitude of SPP mode is kept constant at low intensity levels such as  $1 \times 10^3$  A/m.

### 6.2.3 Results for Inputs with Different Amplitudes

In this device the CW SPP propagating along the silver metal surface acts as the test signal and the waveguide mode of wavelength 1064 nm acts as the control signal. The CW SPP has a constant amplitude of  $1 \times 10^3$  A/m while the amplitude of the waveguide mode is increased in steps such as  $1 \times 10^0$ ,  $1 \times 10^1$ ,  $1 \times 10^2$  A/m and so on. Figure 6-6 shows a snapshot of CW SPP propagating along the metal surface at the bottom of device and the fundamental mode propagation along the waveguide.

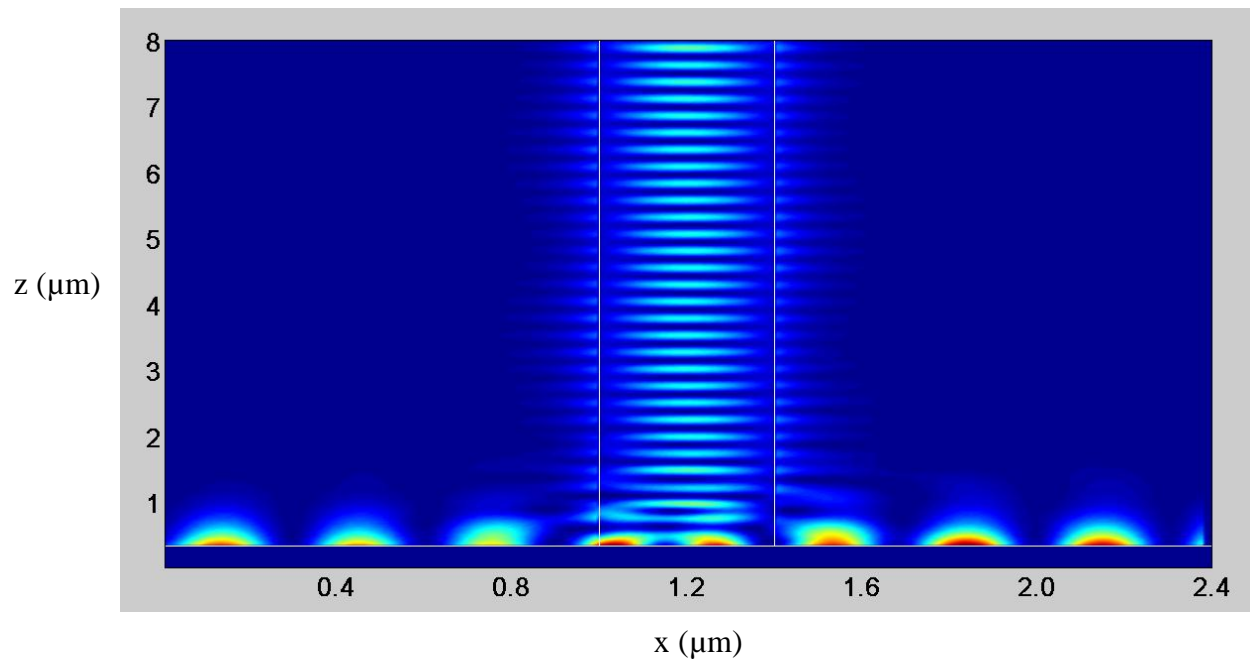


Figure 6 - 6: Snapshot of Metal-Waveguide device with CW SPP and CW waveguide input.

It can be seen that the waveguide mode is fully confined to the core region and the CW SPP propagates smoothly without any radiations from the surface.

For various control inputs, the power and the intensity profile of the waveguide is recorded at the output i.e. at a distance of 400 nm from the right PML.

Figure 6-7 shows the variation of the normalized power profile of the CW SPP under the influence of various control signal amplitudes. It can be seen that the normalized power profile of CW SPP is unaffected and remains almost constant until the control signal amplitude exceeds  $1 \times 10^5$  A/m. For the control signal intensity starting from  $1 \times 10^6$  to  $2 \times 10^6$  A/m, the power of the test signal increases. For the control signal intensity ranging from  $3 \times 10^6$  to  $5 \times 10^6$  A/m, the power of test signal falls rapidly as the non-linearity of ChG glass is activated at such high intensity levels.

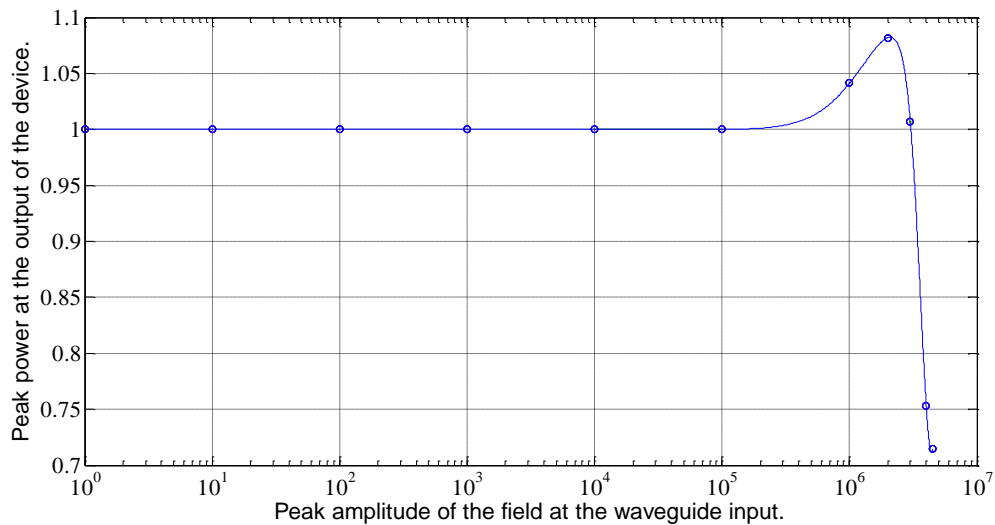


Figure 6 - 7: The Normalized power curve for different control input levels at the device output.

It is to be noted that the effect of control signal on the test signal is removed by subtracting the power of CW SPP in presence of control signal from the power of control signal propagating alone. In this way it can be assured that the calculated output power profile of figure 6-7 is a purely CW SPP power free of all interference from the control signal.

To verify this point, the intensity of the CW SPP is recorded at the output i.e. at a distance of 400 nm from the right PML. It can be recalled that the intensity of an EM signal is proportional to the square of its electric field strength.

$$I = |E|^2 \quad (6.1)$$

where, I is the Intensity of EM signal and

E is the Electric field strength.

Figure 6-8 shows the variation of the normalized intensity profile of the CW SPP under various control signal amplitudes. As intensity is directly proportional to electric field strength, it can be observed that the intensity profile plot closely resemble the power profile plot.

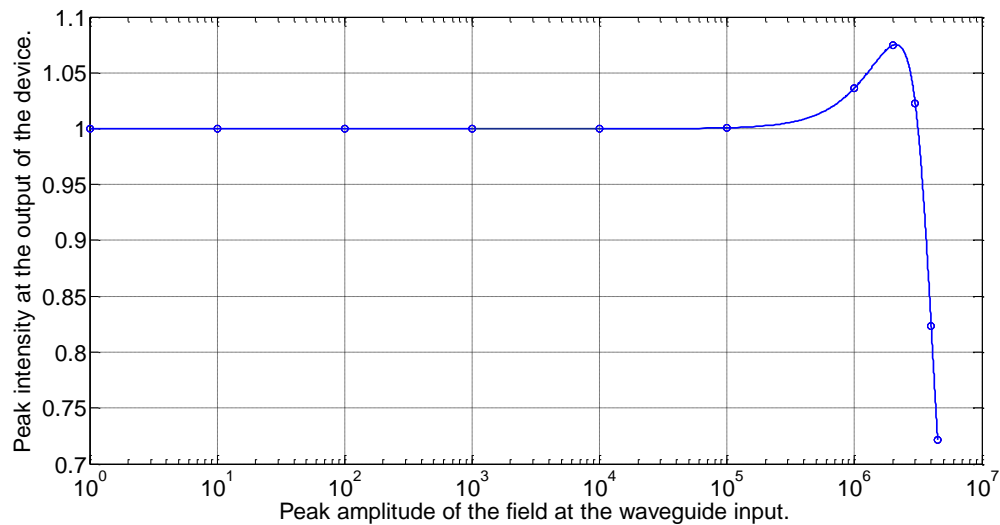


Figure 6 - 8: The normalized intensity curve for different control input levels at the device output.

Figure 6-9 and 6-10 show the variation of normalized power and normalized intensity of the test signal with device dimensions at low and high control input intensities respectively. The

solid line represents the power profile when the core is modeled as non-linear Chalcogenide glass and the dashed and dotted lines represent the case when the core is modeled as dispersive and linear material respectively.

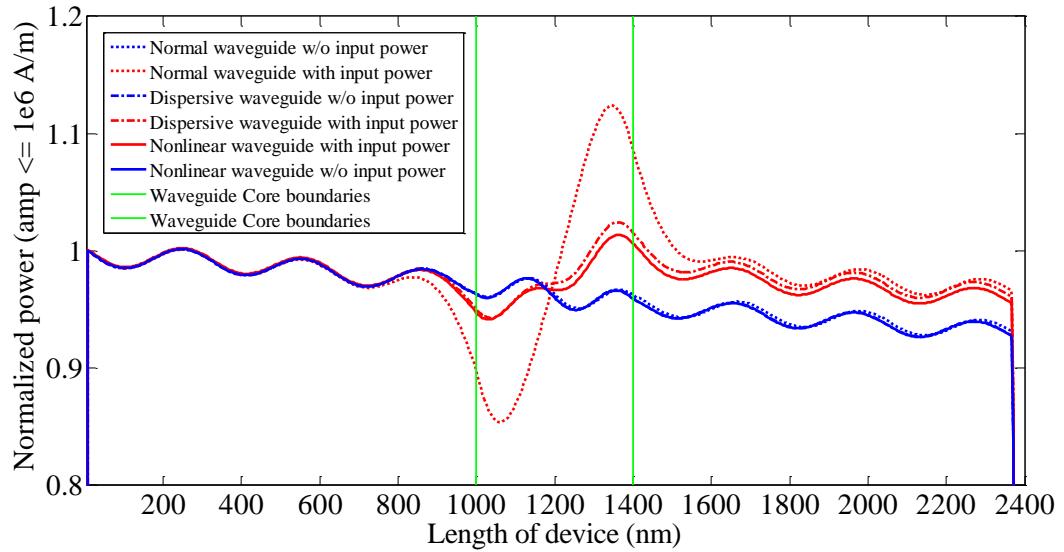


Figure 6 - 9: Spatial power profile of the Metal-Waveguide structure at low control signal intensity.

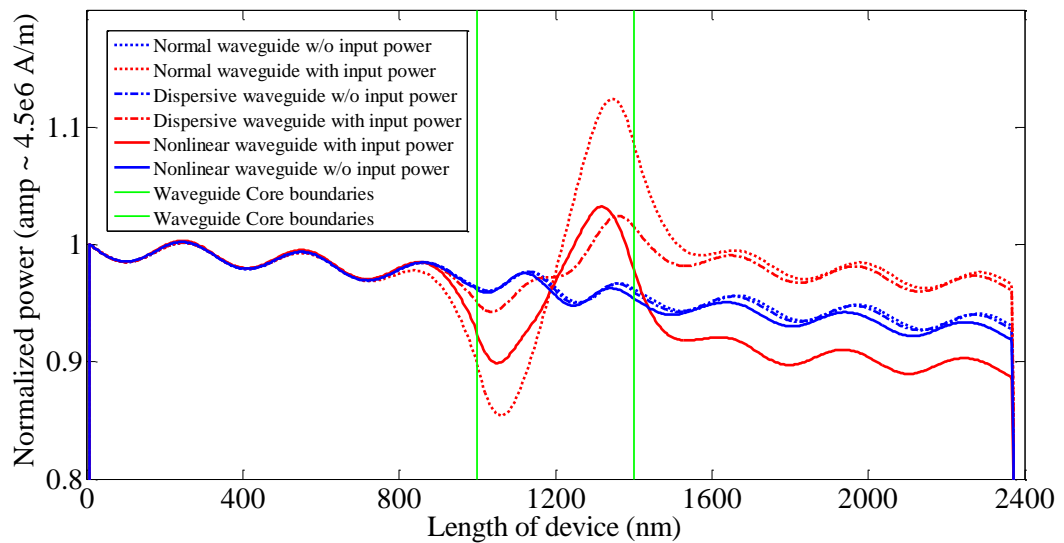


Figure 6 - 10: Spatial power profile of the Metal-Waveguide structure at high control signal intensity.

From figure 6-9 it is very apparent that at low control input intensities all the materials behave linearly. But, at high control input intensities, it can be seen that the Chalcogenide glass starts behaving non-linearly and hence it attenuates the output as shown in figure 6-10.

### **6.3 Metal-Insulator-Metal (MIM) Structure**

The second device to be tested for modulation of SPPs is a Metal-Insulator-Metal (MIM) structure. The interaction between two dissimilar CW SPP signals is investigated by recording the power profile of the CW SPP at the output. It would be appropriate to begin the discussion on the Metal-Insulator-Metal structure with the detailed description of the model and its input sources.

#### **6.3.1 Model Description**

Metal-Insulator-Metal structures are one of the prominent and widely used devices in guiding plasmonic light at sub-nanoscale wavelengths. It is ultra-compact and suitable for integration with semiconductor nano-devices because of its nano-scale dimensions. Moreover it strongly confines the plasmonic light close to the metal surface. The Metal-Insulator-Metal structure is as shown in figure 6-11.



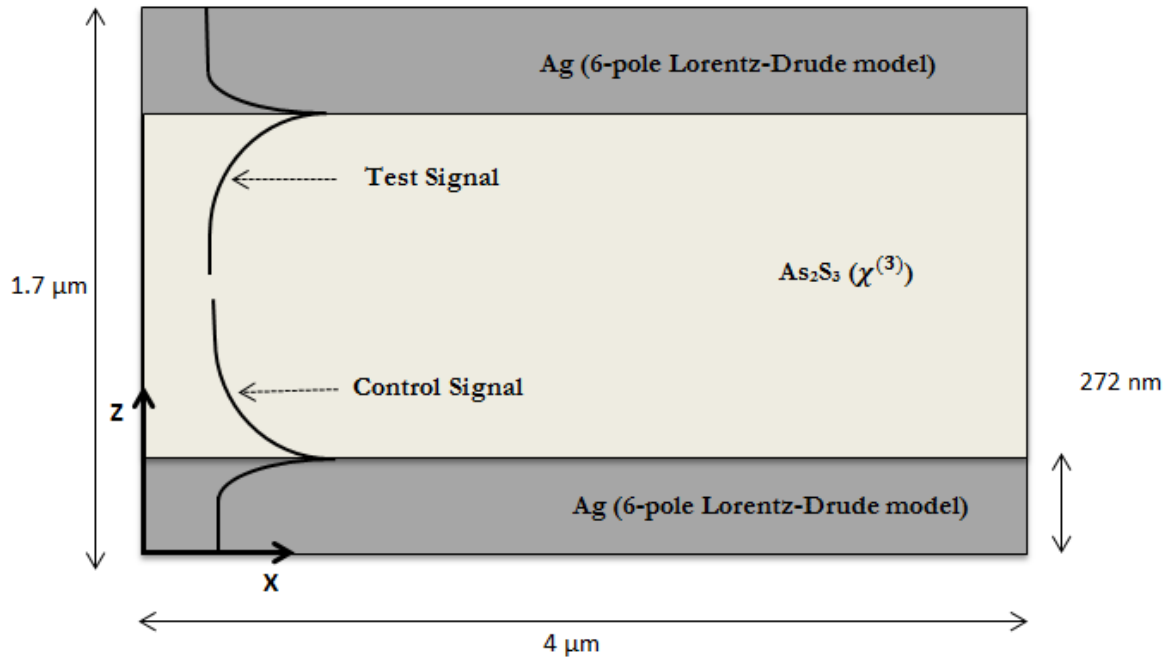


Figure 6 - 11: Block diagram of Metal-Insulator-Metal structure.

The MIM structure that is modeled in this thesis consists of a Chalcogenide glass ( $As_2S_3$ ) sandwiched between two silver films of thickness 272 nm. The thickness of the insulator is approximately 1.15  $\mu m$ . The length of the total device is 4  $\mu m$ . The MIM structure is aligned such that its length is along x-axis and width along z-axis as can be seen in figure 6-11.

### 6.3.2 Input Source

In order to obtain a neat input field profile to excite SPP, a Gaussian pulse is excited close to the metal surface. As a result some of the light couples with the metal surface to form SPP, which propagates along the length of the metal. The SPP mode is obtained by taking the cross-section profile of a fully developed Plasmon that is propagating along the metal surface. Figure 6-12 and 6-13 shows the  $E_z$  field profile of SPP mode of unity amplitude. The amplitude of SPP mode propagating along the top metal surface is kept constant at low intensity levels and hence it acts as a test signal, whereas the amplitude of SPP mode

propagating along the bottom metal surface is switched from low intensity levels to high intensity levels and thus acting as a control signal. The wavelength of control signal is chosen as 1064 nm. When the control signal is switched from low intensity levels to high intensity levels it excites the non-linear behaviour of Chalcogenide glass.

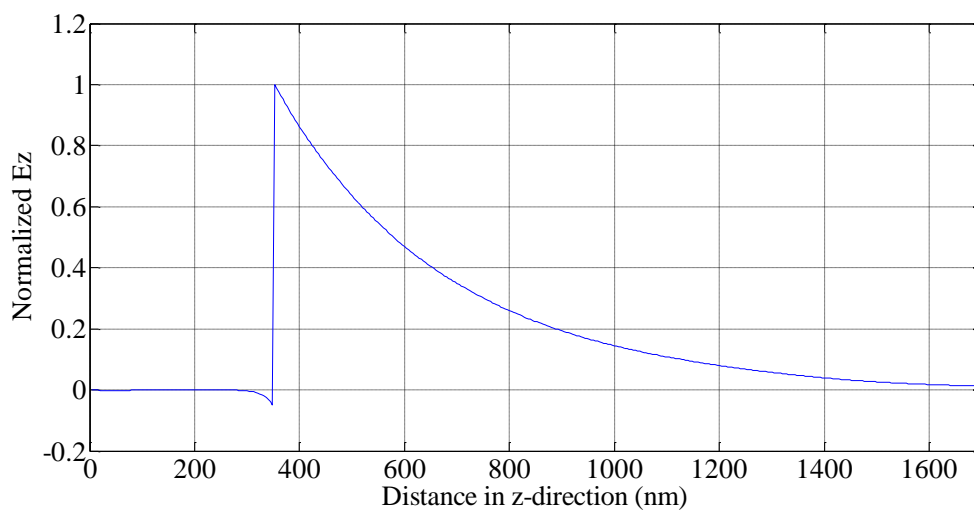


Figure 6 - 12: The normalized Ez field profile pumped in the device.

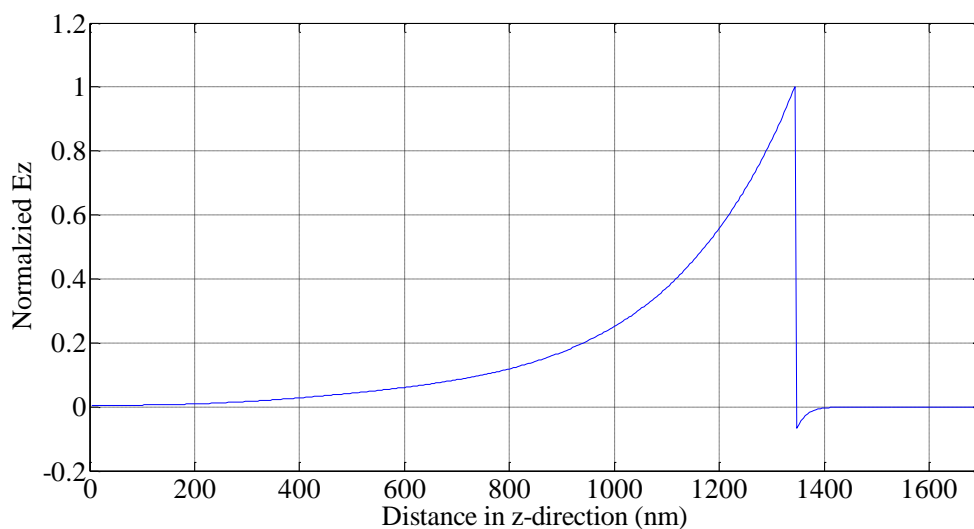


Figure 6 - 13: The normalized Ez field profile pumped in the device.

### 6.3.3 Results for Inputs with Different Amplitudes

For modulation plasmon in the MIM structure the test signal is excited at low intensity levels such that it does not induce non-linearity of its own in the ChG glass.

Once the test signal is fully developed and spans the entire length of the device, a control signal of varying intensities is launched to study the variation of power in upper half region of the device. Figure 6-14 shows a snapshot of CW SPP propagating along the top and bottom metal surfaces of the device with clear demarcation between insulator and metal surfaces.

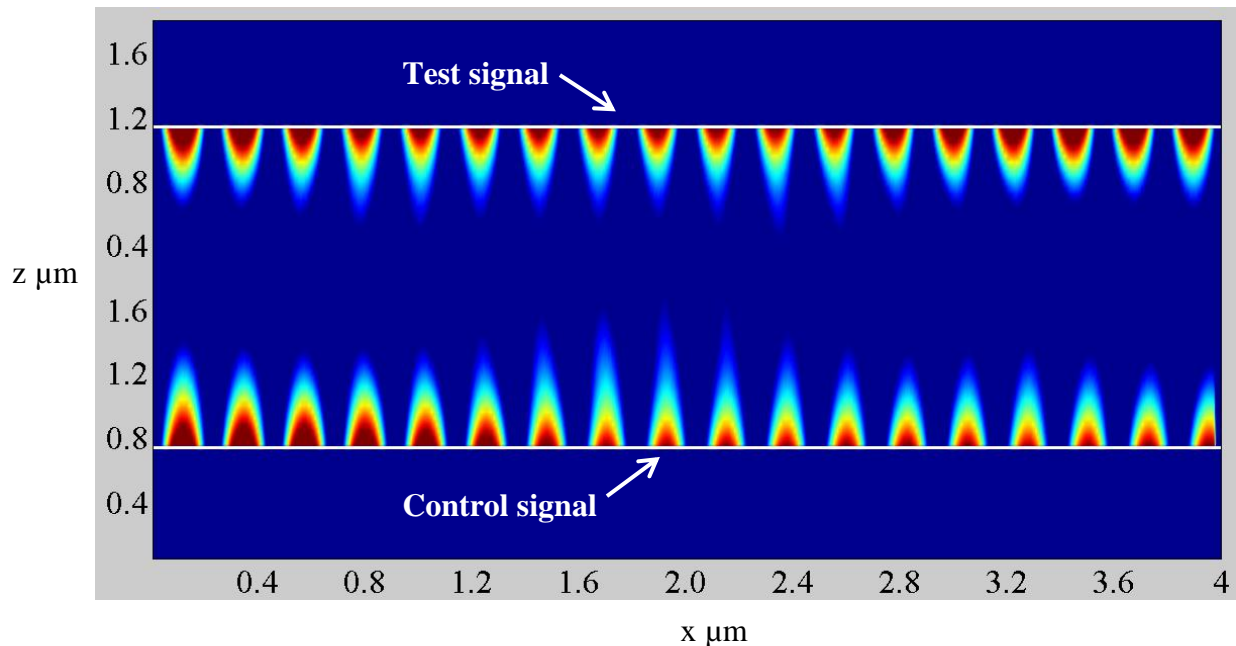


Figure 6 - 14: Snapshot of the MIM structure with test signal and control signal clearly visible.

In figure 6-15 it can be seen that as the control signal is gradually increased from amplitude of  $1 \times 10^8$  V/m to  $8 \times 10^8$  V/m the power profile of the upper half region of the device increases monotonously until  $6 \times 10^8$  V/m. Beyond this the power profile starts falling as can be seen in the case of control signal with amplitude of  $8 \times 10^8$  V/m. This is due to the

fact that the non-linear behaviour of the ChG glass is triggered at this intensity, and hence the SPP power is lost to radiation.

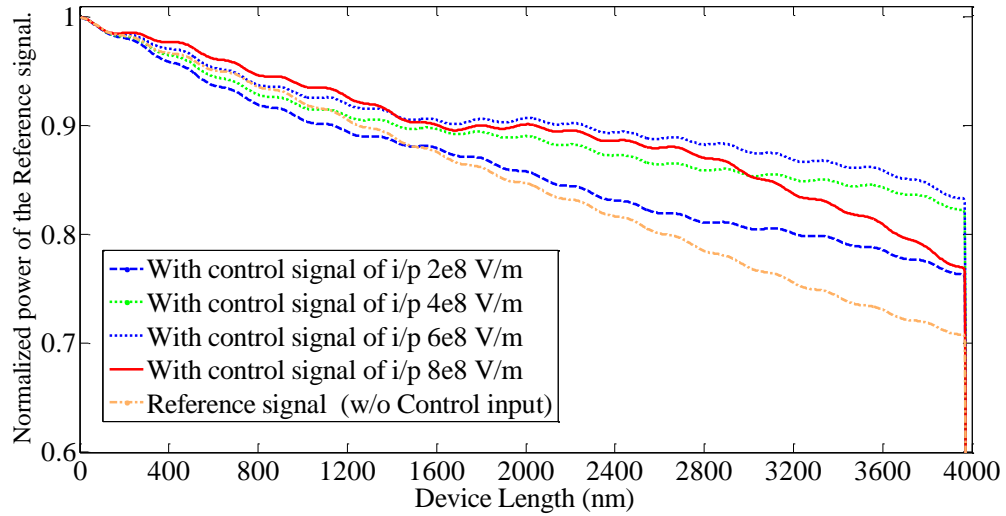


Figure 6 - 15: Normalized output power of MIM device at low intensities

On further increase in the intensity levels of the control signal, the output power falls gradually as can be perceived from the figure 6-16.

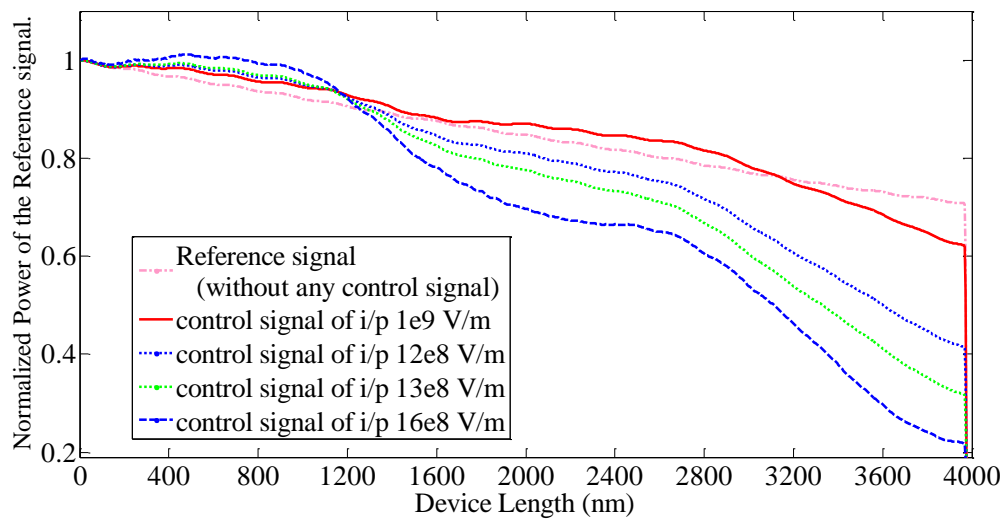


Figure 6 - 16: Normalized output power of MIM device at high intensities

At certain point, the output intensity falls below the reference power level (power of test signal recorded in the absence of any control signal). This occurs at the control signal amplitude of  $1 \times 10^9$  V/m. With the increase in the control signal levels, the output keeps falling further as there is an increase in the non-linearity of ChG glass.

Figure 6-17 and 6-18 shows the output power plots for the case with reduced dimensions. The width of the device is reduced to  $1.2 \mu\text{m}$  and length to  $2 \mu\text{m}$ . It can be seen that the MIM structure behaves similar to the one in previous case for control input intensity in the range  $8 \times 10^8$  V/m. The only exception is that the device is lossier than the previous one.

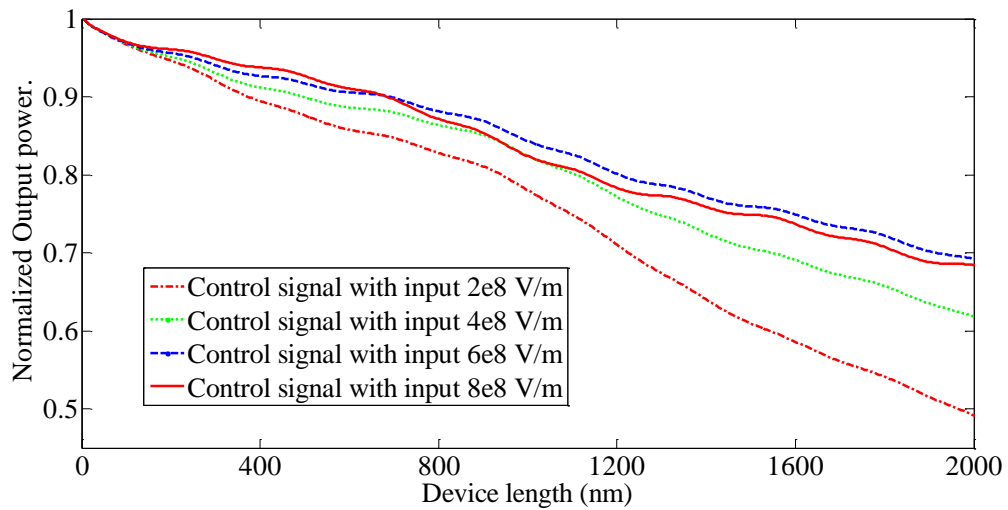


Figure 6 - 17: Normalized output power of truncated MIM device at low intensities

For further increase in the intensity of control signal the power of the test signal is totally extinct as the normalized power profile falls below  $0 \text{ W/m}^2$  as seen in figure 6-18. This means that the SPP is blocked and power is flowing the other way (reflected) for control input intensity of amplitude  $15 \times 10^8$  and  $16 \times 10^8$  V/m. Figure 6-18 shows the power profile of the truncated device with the non-linearity of the material activated. To explain

this behaviour it can be stated that at higher inputs beyond  $15 \times 10^8$  V/m, physical phenomena such as photon absorption takes place which eventually causes overheating in ChG glass eventually limiting the amplification and thereby inhibiting the nonlinear action.

Finally it can be concluded that as the input intensity of the control signal is continuously increased, the ChG glass reaches saturation where it is no more able to exhibit nonlinear phenomenon and hence start acting as normal dielectric.

As a result this swing in the output power from high to low power levels on application of progressively increasing control signal input demonstrates the classical case of switching which can be used in fabrication of active devices.

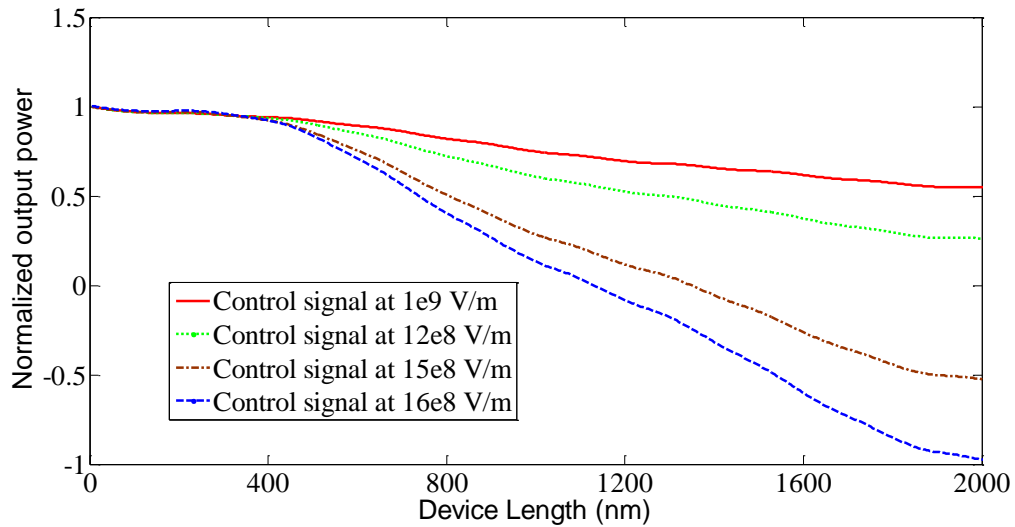


Figure 6 - 18: Normalized output power of truncated MIM device at high intensities

The change in refractive index of the material due to instantaneous Kerr effect can be calculated using the eqn. 3.59 which is given as  $n(I) = n + n_2 I$  or  $n(I) = n + n_2 \left( \frac{|E|^2}{2\eta} \right)$ ,

where  $n_2 = 5.56933 \times 10^{-17} \text{ m}^2/\text{W}$  and  $\eta$  is the impedance of the medium. For the

control signal intensity variation between  $8 \times 10^8$  V/m and  $16 \times 10^8$  V/m the change in refractive index is between 0.212 and 0.852.

## 6.4 Embedded Metal Film Structure

After investigating for a device which can modulate the SPPs in realms other than power and intensity domain we finally came up with a novel and innovative idea of modeling a prototype named 'Embedded Metal Film Structure'. It has an ultra-thin metal film embedded inside the Chalcogenide glass. To begin the discussion on the Embedded Metal Film (EMF) structure we start with detailed model description as follows.

### 6.4.1 Model Description

The EMF structure consists of a non-linear ChG glass deposited on silver layer of thickness 272 nm. A thin layer of Ag metal of 20 nm thickness is embedded inside the ChG glass as shown in figure 6-19. The thickness of 20 nm is chosen to allow the asymmetric mode of the SPP to couple its energy back and forth along the length of the thin metal film. The length of the EMF device is 8  $\mu\text{m}$  along the x-direction and the width is 2.6  $\mu\text{m}$  along the z-direction as is clearly evident in figure 6-19.

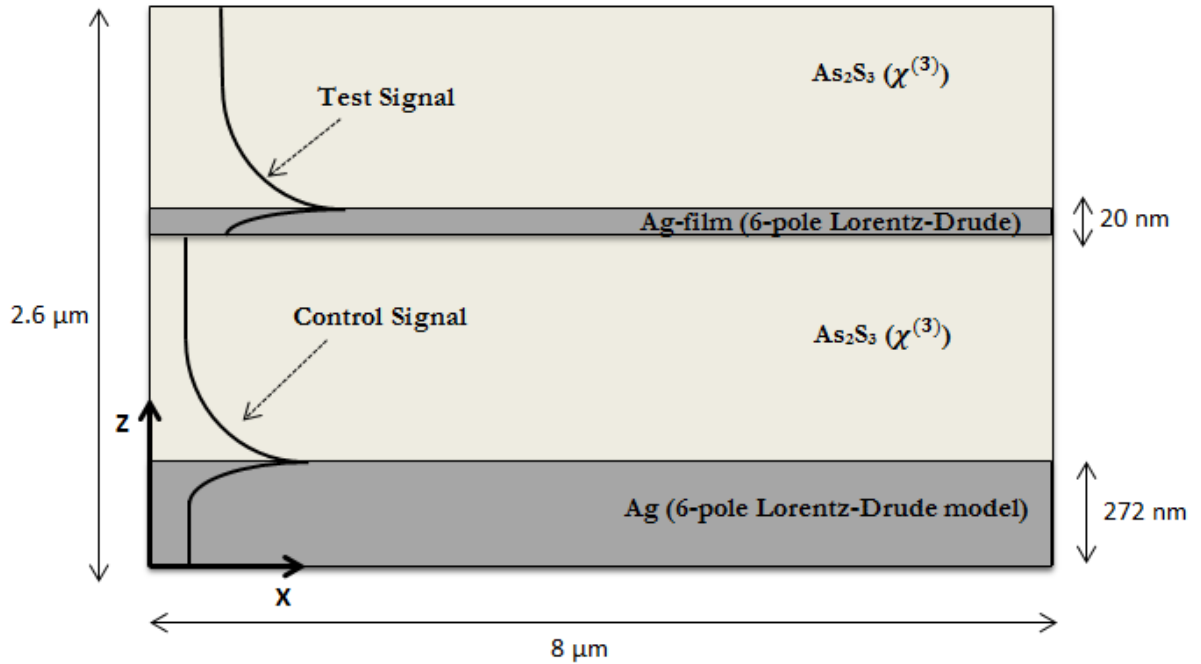


Figure 6 - 19: Block diagram of Embedded Metal Film structure

### 6.4.2 Input Source

Plasmon mode is obtained by taking the cross-section profile of a fully developed plasmon that propagates along the metal surface. The technique for obtaining the plasmon mode is discussed in detail in section 6.3.2. Figure 6-20 and 6-21 shows the  $E_z$  field profile of SPP mode of unity amplitude. The SPP mode shown in figure 6-15 (a) corresponds to the plasmon propagating on the metal surface whereas the SPP mode shown in figure 6-15 (b) corresponds to the asymmetric mode of the plasmon propagating on the thin metal film. The amplitude of SPP mode of thin metal film is kept constant at low intensity levels such as  $1 \times 10^5$  V/m.



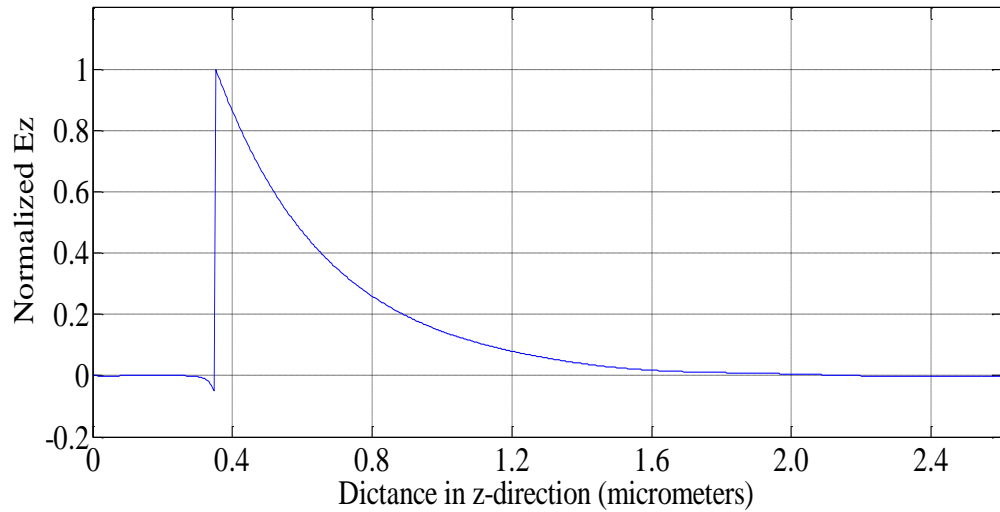


Figure 6 -20: The normalized Ez field profile pumped in the device.

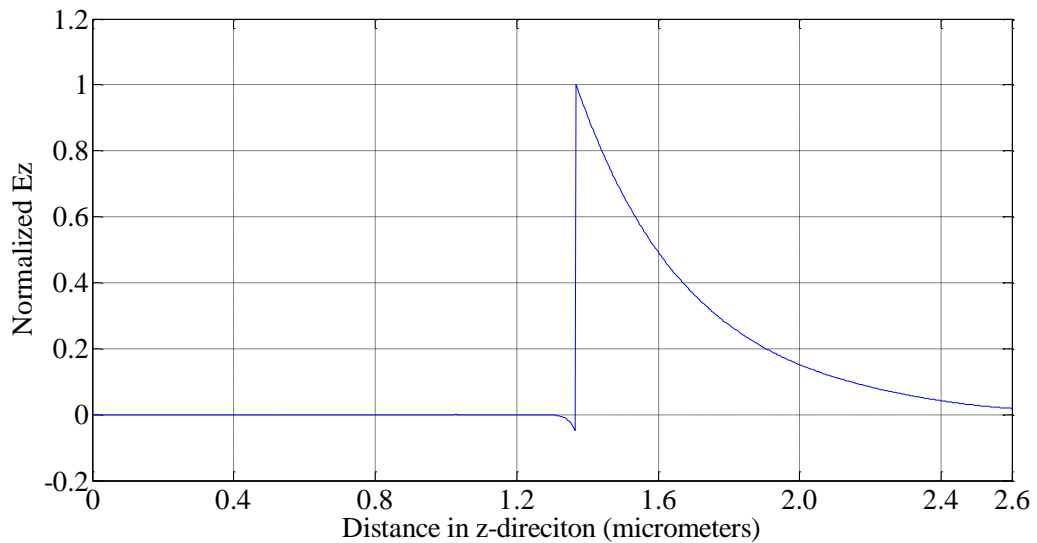


Figure 6 - 21: The normalized Ez field profile pumped in the device.

### 6.4.3 Results for Inputs with Different Amplitudes

The CW SPP that is pumped into the thin metal surface acts as test signal, as it is generally pumped with low intensity inputs, whereas the CW SPP pumped onto the surface of the thick metal acts as control signal. The wavelength of the control signal is chosen as 1064 nm.

The test signal is first allowed to fully proliferate along the thin metal film and then the control SPP of various intensities is launched. Power profile for the region above the thin metal is calculated so as to get results without any interference from the control signal. Figure 6-22 shows a snapshot of the device.

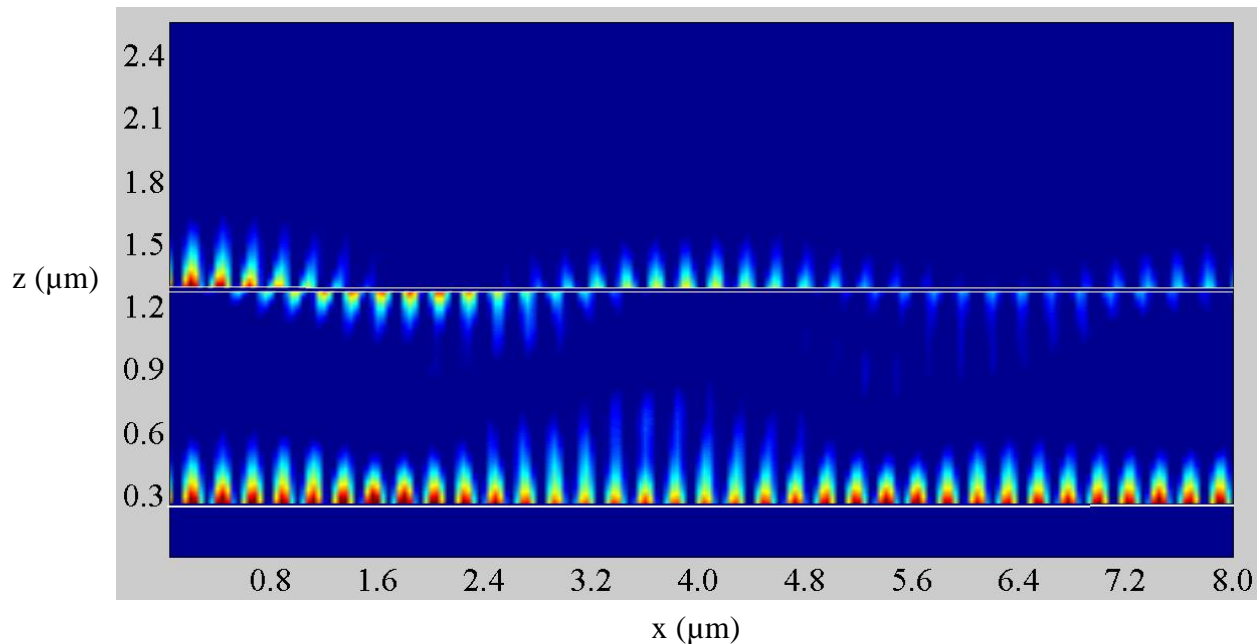
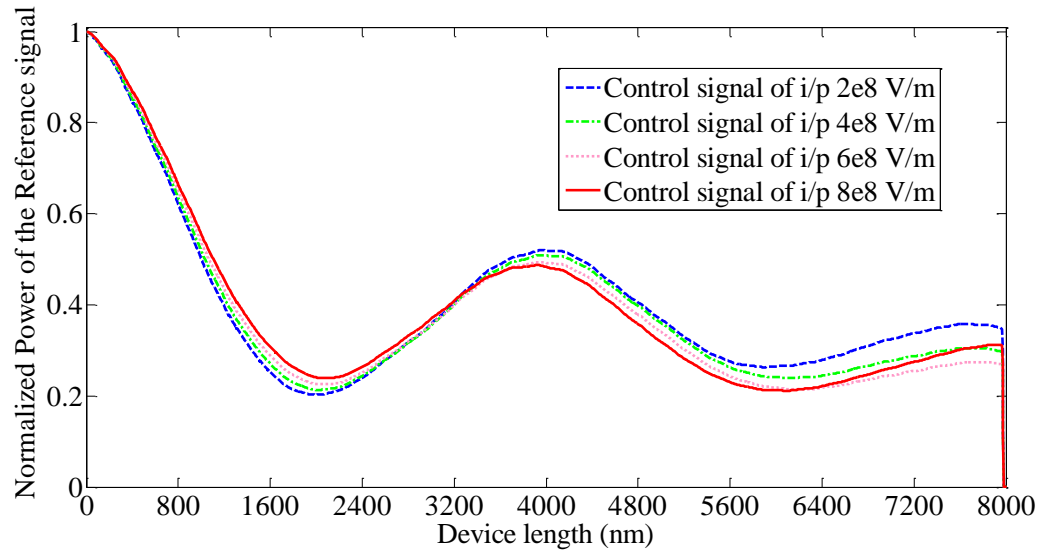


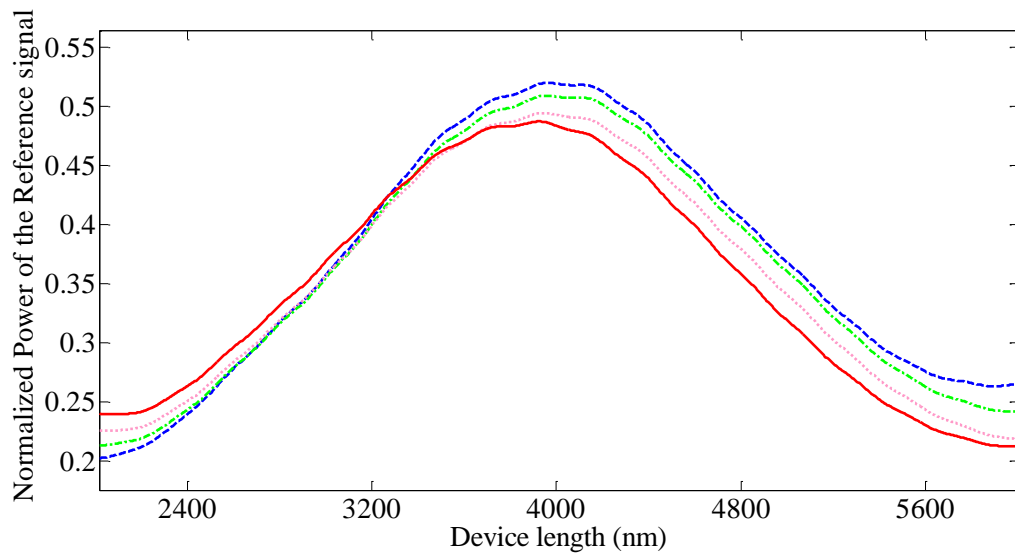
Figure 6 - 22: Snapshot of Embedded Film Structure showing test signal and control signal inputs.

For test signal of amplitude  $1 \times 10^5$  V/m and for gradual increase in the amplitude of the control signal ranging from  $2 \times 10^8$  to  $8 \times 10^8$  V/m, the calculated power profile of the device is as shown in figure 6-23 (a). The power profile curves of the device overlap one another until  $6 \times 10^8$  V/m control signal input. But, the most striking behavior is observed at the control signal amplitude of  $8 \times 10^8$  V/m. The non-linear behavior of the ChG glass is triggered at this amplitude and hence the power curve corresponding to  $8 \times 10^8$  V/m represented by dotted line shows slight shift from the rest of the pack. Figure

6-23 (b) shows the magnified version of figure 6-23 (a) to highlight minute shift experienced by the test signal under the control input of  $8 \times 10^8$  V/m.



(a)



(b)

Figure 6 - 23: Power profile of EMF structure at low control signal intensity (a) Profile of complete device (b) Magnified version.

For further increase in the amplitude of control signal input, a clear phase shift is observed. Apart from the phase shift, the strange upward shift of power curves is observed for control input amplitude ranging from  $1 \times 10^9$  to  $16 \times 10^9$  V/m. This is due to the fact that the higher control signal input levels changes the effective refractive index in the bottom ChG glass. Due to this mismatch between the bottom and the top ChG glass interface the test signal tries to minimize its coupling across the thin film as shown in figure 6-24.

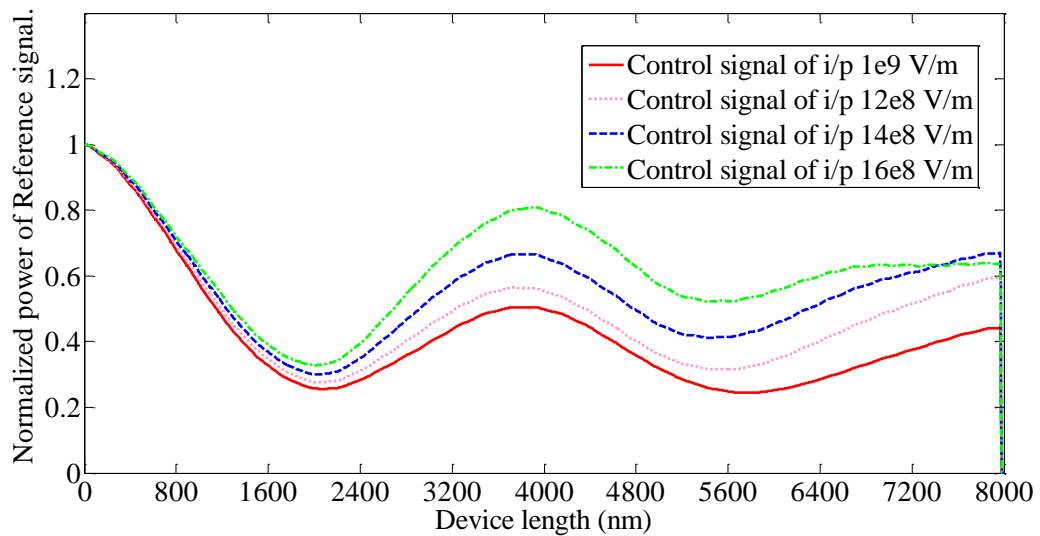
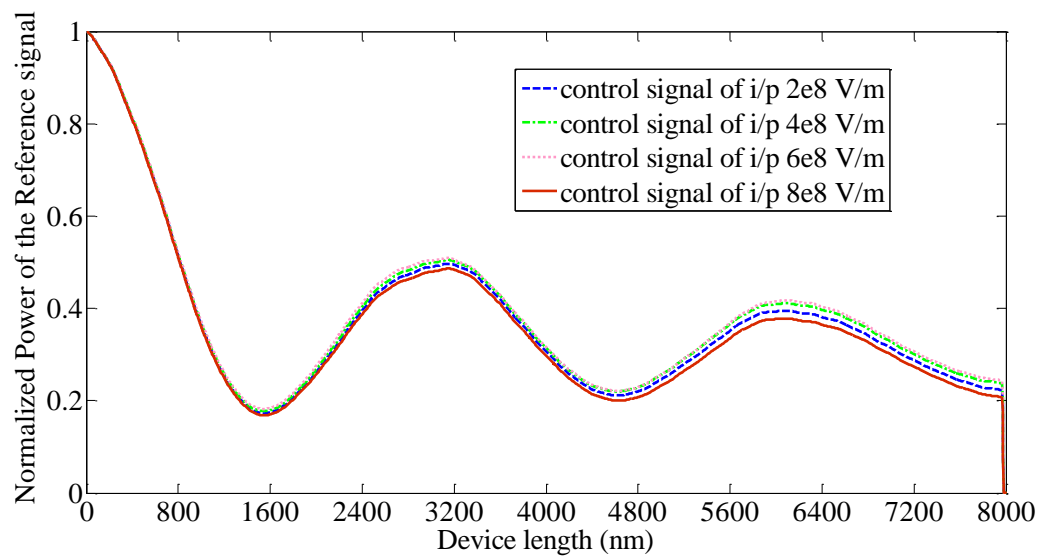


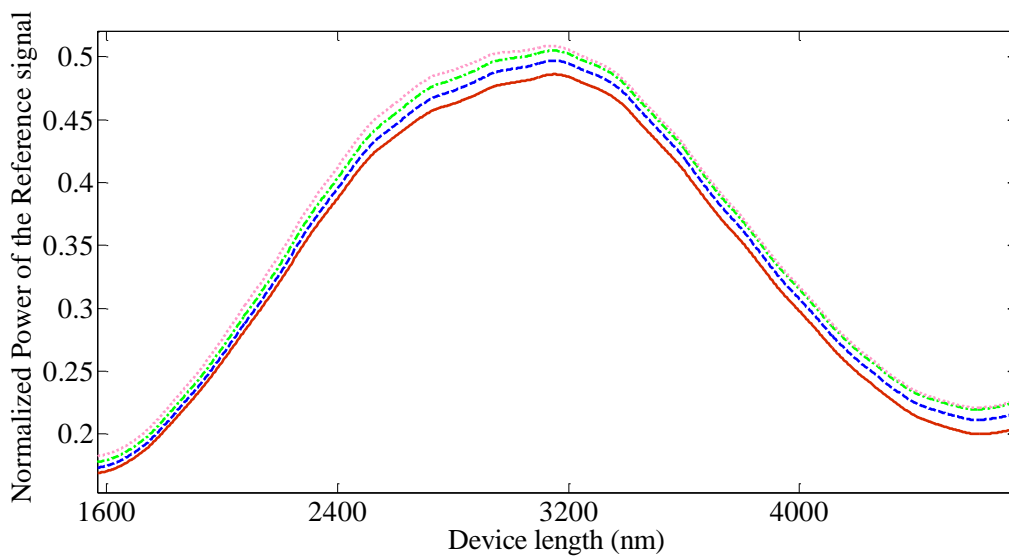
Figure 6 - 24: Power profile of EMF structure at high control signal intensity

To support the observation made about the mismatching refractive index phenomenon we present a case where the test signal is pumped with very high amplitude such as  $1 \times 10^9$  V/m. The test signal induces nonlinearity of its own in the upper region of ChG glass. For gradual increase in the amplitude of control signal ranging from  $2 \times 10^8$  to  $8 \times 10^8$  V/m the calculated power profile of the device is as shown in the figure 6-25 (a). The power profile curves of the device overlap above one another until  $6 \times 10^8$  V/m control signal

input. There is very slight shift in the power curve profile at  $8 \times 10^8$  V/m which can be seen in the figure 6-25 (b), which is the amplified version of figure 6-25 (a).



(a)



(b)

Figure 6 -25: Power profile of EMF structure at low control signal intensity (a) Profile of complete device (b) Magnified version.

But for further increase in the amplitude of control signal from  $1 \times 10^9$  to  $16 \times 10^8$  V/m there is no apparent upward shift in the Power curves even though the phase shift is clearly evident as depicted in figure 6-26 (a) and (b).

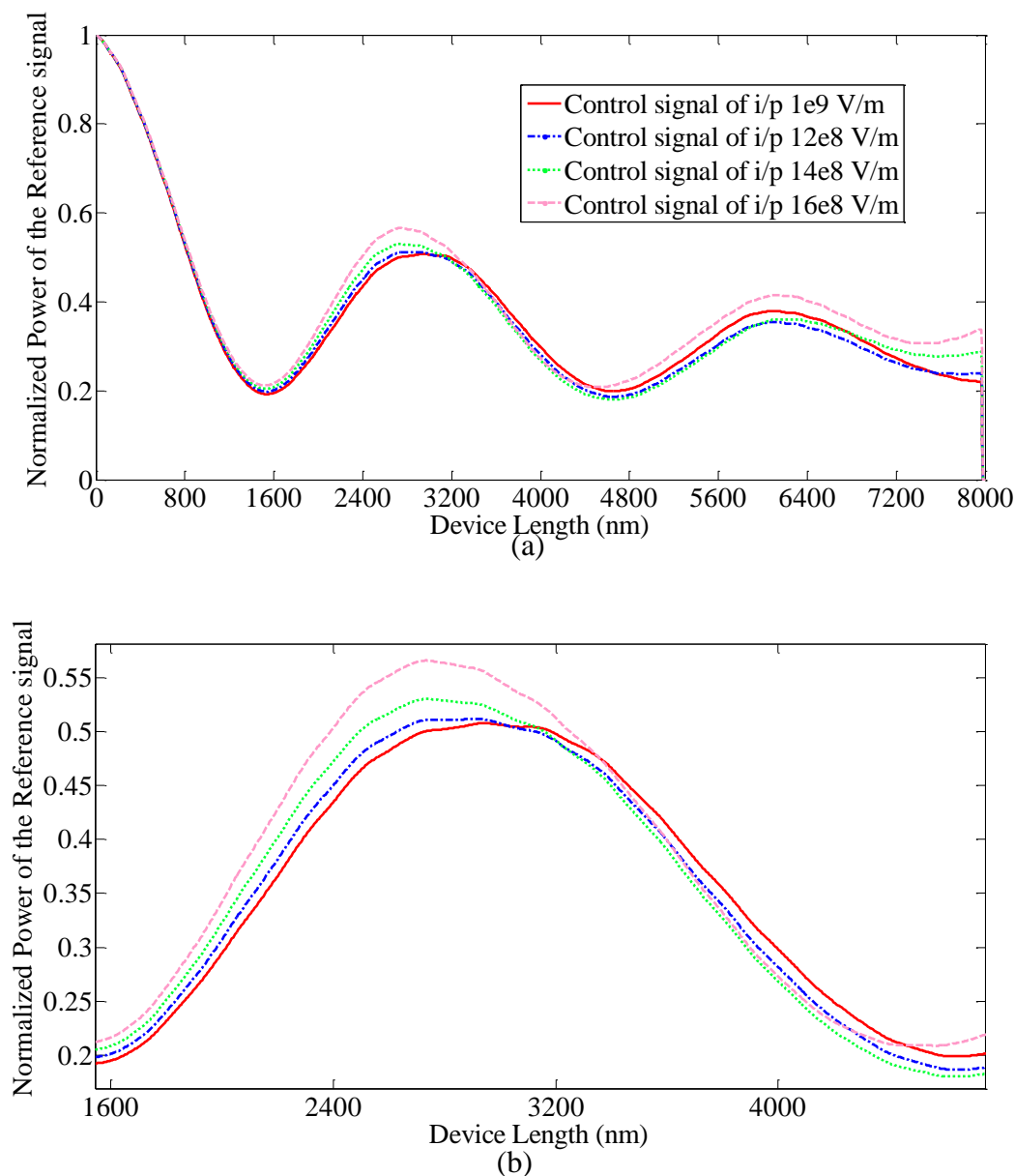


Figure 6 - 26: Power profile of EMF structure at low control signal intensity (a) Profile of complete device (b) Magnified version.

Figure 6-26 (b) is the magnified version of figure 6-26 (a) to better visualize the shift in power curve profile and to establish the fact that this phenomenon also contributes to the modulation of SPPs taking us a step closer to realization of Active Plasmonics.

To further support the observation that the mismatch in the refractive index of the material hinders the uniform coupling of SPP across a thin film we present a case where CW SPP is pumped across the thin film flanked on either by dielectric material of different refractive indices. Figure 6.27 shows the power profile of CW SPP in the upper dielectric region having a constant refractive index of 2.7. The refractive index of bottom dielectric region is changed in steps as 2.5, 2.7 and 2.9.

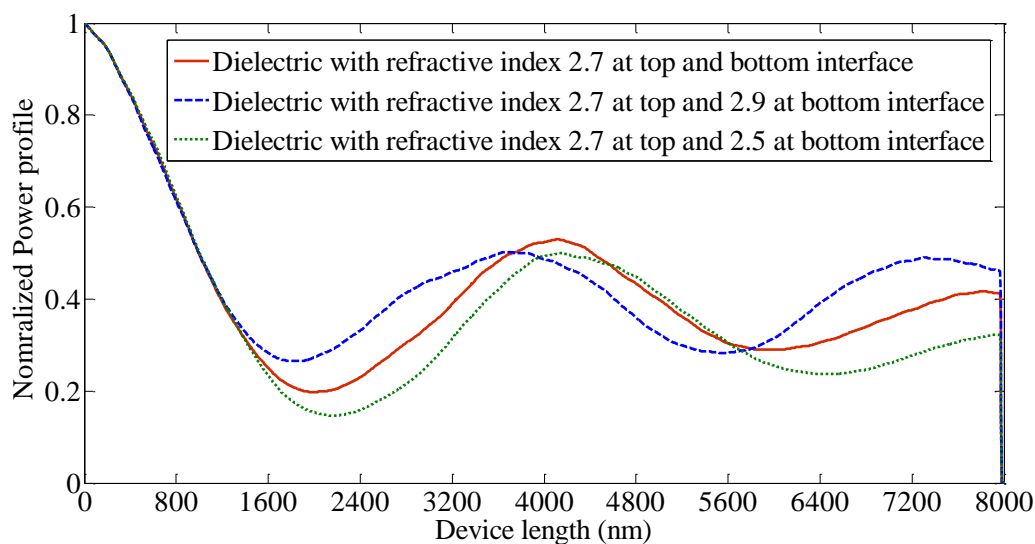


Figure 6 - 27: Power plot of a novel model depicting the coupling behavior of CW SPP along thin metal film for dielectric material of different refractive index.

It can be seen that the CW SPP propagates uniformly for homogenous dielectric material on either side. But, when the refractive index of bottom dielectric is changed to 2.9 the CW SPP tries to propagate and retain itself at the top dielectric medium and hence the depth of

penetration onto the bottom interface is less than the previous case, whereas for the dielectric medium of refractive index 2.5 the Plasmon penetrates more and tries to retain itself at the bottom interface as can be seen from figure 6.27.

## 6.5 Coupled Plasmonic Nanocavities Structure

The fourth device to be tested for modulation of SPPs is a Coupled Plasmonic Nanocavities (CPN) structure. The interaction between the Pulsed line source excited over the Nanocavities and the Continuous Wave (CW) SPP signal propagating along the bottom interface of the metal surface is analyzed by recording the Power profile of the CW SPP at the output. To begin the discussion on the Metal-Waveguide structure we start with detailed model description as follows.

### 6.5.1 Model Description

The CPN structure consists of the Silver metal of thickness 340 nm. A deep cavity is etched at the center of the metal. This cavity is abutted by grating of uniform depth and thickness. The cavity and the gratings are filled up by depositing non-linear ChG glass over it. The bottom of the metal is coated with dielectric material of refractive index 2.7 as shown in figure 6-28. These grating are periodically arranged in such a fashion that the energy from the line source impinging on the ChG glass interface gets is focused at the cavity region and thereby causing the cavity to resonate.

The separation between the bottom of the cavity and the bottom of the metal surface interface is extremely small. This spacing is denoted as 'gap' in figure 6-28. This gap determines the amount of light that can leak from the cavity into dielectric medium.



Simultaneously it also determines the amount of Plasmon power that can peep/leak/interact with the material present inside the cavity. The length of the device is  $4\ \mu\text{m}$  and the width of the device is  $3\ \mu\text{m}$ . The Coupled Plasmonic Nanocavities structure is aligned such that its length is along x-axis and width along z-axis.

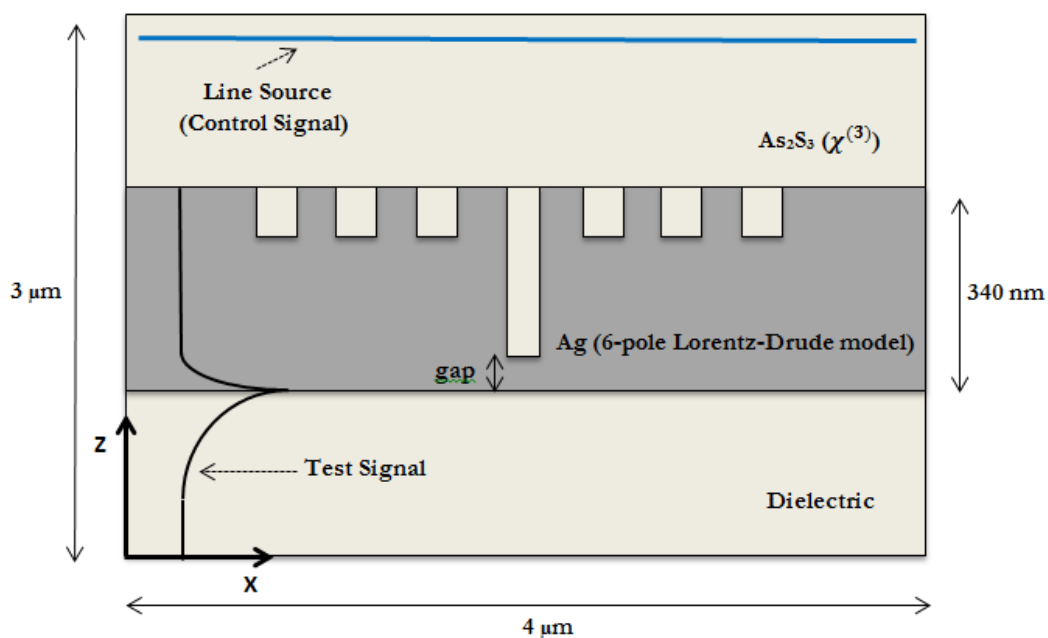


Figure 6 - 28: Block diagram of Coupled Plasmonic Nanocavities structure.

Figure 6.29 shows the magnified image of the etched metal with all features clearly labelled.

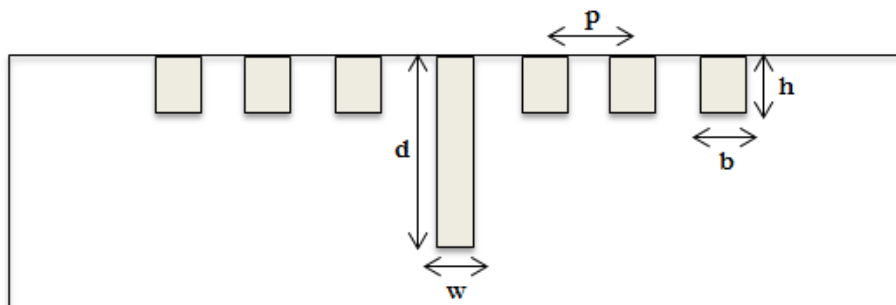


Figure 6 - 29: Enlarged view of Metal gratings with clear labeling

The depth of the cavity is represented as 'd' and its width by 'w', 'h' corresponds to the depth of the grating and 'b' as the grating width. Moreover 'p' represents the grating periodicity for the given device.

The real dimensions that were modelled for simulation are as follows,

Depth of Cavity  $d=300$  nm;

Width of Cavity  $w=60$  nm;

Depth of Grating  $h=40$  nm;

Width of Grating  $b=40$  nm &

Periodicity of Grating  $p=80$  nm.

### **6.5.2 Input Source**

Plasmon mode is obtained by taking the cross-section profile of a fully developed Plasmon that propagates along the metal surface. The technique for obtaining the Plasmon mode is discussed in detail in section 6.3.2. Figure 6-30 shows the  $E_z$  field profile of SPP mode of unity amplitude and it corresponds to the Plasmon propagating on the bottom of the metal surface. The amplitude of SPP mode of thin metal film is kept constant at low intensity levels such as  $1 \times 10^4$  V/m.

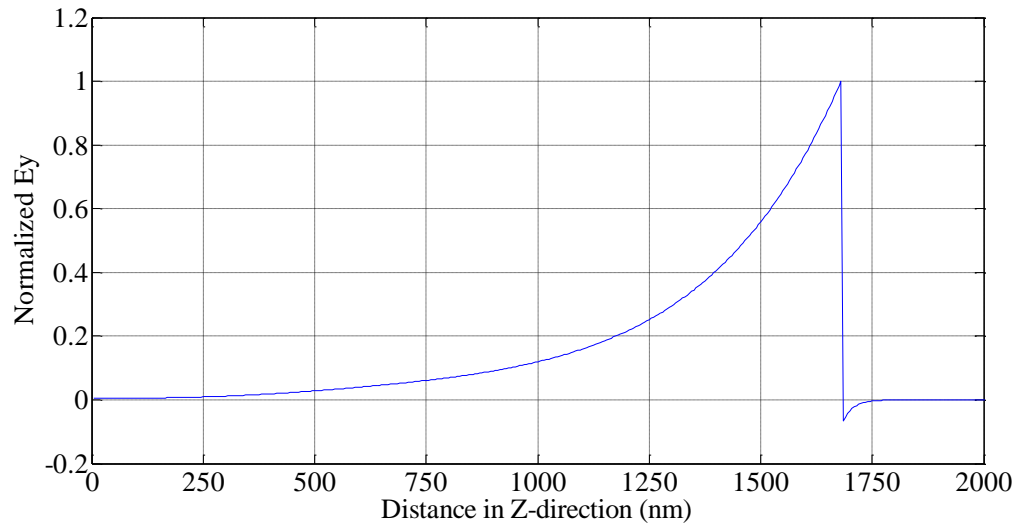


Figure 6 - 30: The normalized  $E_z$  field profile pumped in the device.

The line source is placed at the top of the device in the ChG glass region. It feeds the control signal of varying amplitudes. It is multiplied with a Gaussian pulse and a time varying cosine term to make it operate as a pulsed line source. The light after being incident on the gratings gets focused in the cavity region which eventually resonates for carefully designed set of geometrical parameters.

### 6.5.3 Results for Inputs with Different Amplitudes

The line source positioned at the top of the ChG glass acts as the control signal feeder. The wavelength of control signal is chosen as 1064 nm. When the control signal varies from low intensity levels to high intensity levels the ChG glass behavior changes from linear material to non-linear material. Moreover the device is studied for various ‘gap’ dimensions such as 20 nm, 40 nm and 60 nm to get the clear picture of the output power variation. Figure 6-31 shows the snapshot of the device when the line source alone is switched on. The gratings are

clearly seen and one can notice that some amount of power leaks through the thin gap that separates bottom of the cavity and the bottom metal surface.

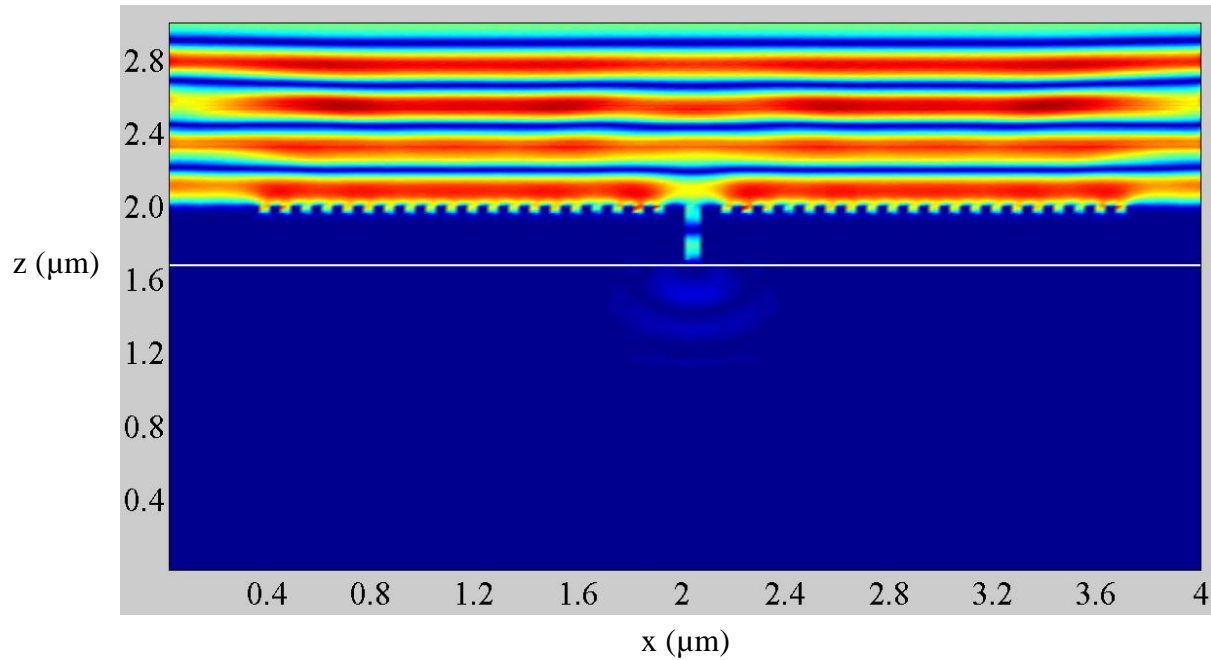


Figure 6 - 31: Snapshot of CPN structure with only the pulsed Line source switched on.

The intensity of the leaked power decreases as the ‘gap’ dimension keeps increasing. The white line in the figure 6-31 shows demarcation between the metal surface and the bottom dielectric medium.

Figure 6-32 shows the snapshot of the Coupled Plasmonic Nanocavities structure when the CW SPP alone is pumped in. It can be clearly seen that some of the energy from the SPPs gets radiated in the device. The CW SPP acts as test signal as it is pumped with low intensity levels.

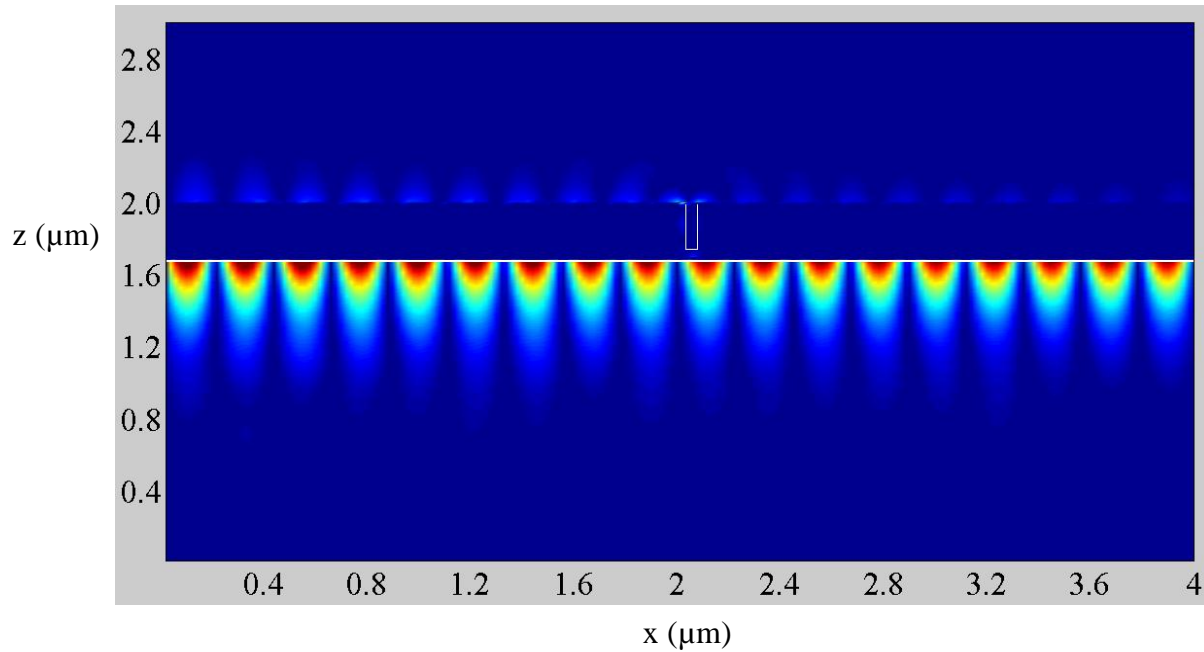


Figure 6 - 32: Snapshot of CPN structure with CW SPP pumped in.

Figure 6-33 shows the results for the device with ‘gap’ dimensions of 40 nm. The test signal is pumped with amplitude of  $1 \times 10^4$  V/m and the control signal amplitude is varied from  $1 \times 10^8$  to  $18 \times 10^8$  V/m. Initially the Chalcogenide glass is replaced with a linear dielectric medium of refractive index 2.7. For the linear material the output SPP power is recorded for various control signal inputs as highlighted before. The plot with square marker shows the output plasmon power with linear material at top. It can be seen that the normalized output power is almost constant irrespective of any change in control signal amplitude.

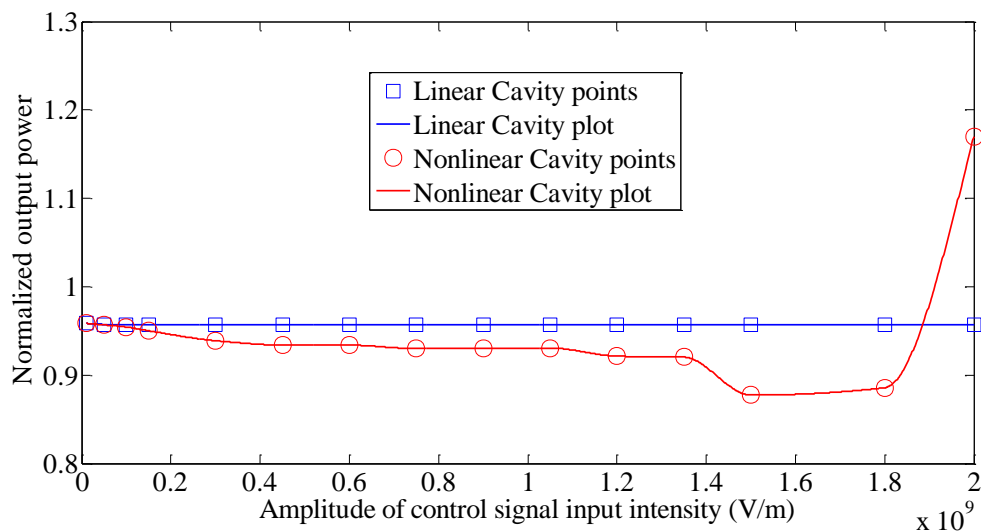


Figure 6 - 33: Power plot of CNP device with gap dimension of 40nm

But when linear material is replaced with the non-linear ChG glass and the output power for various control signal intensities are recorded, it can be seen that the output power (represented by the plot with round markers) remains almost constant until  $1 \times 10^9$  V/m and starts falling gradually until  $18 \times 10^8$  V/m. This is due to the fact that Plasmon encounters losses due to the non-linear behavior of ChG glass at such high intensities.

Figure 6-34 shows the results for the device with 'gap' dimensions of 20 nm. It can be seen that due to very thin gap compared to the previous case, the test signal experiences more loss due to better interaction between the test signal and the cavity material.

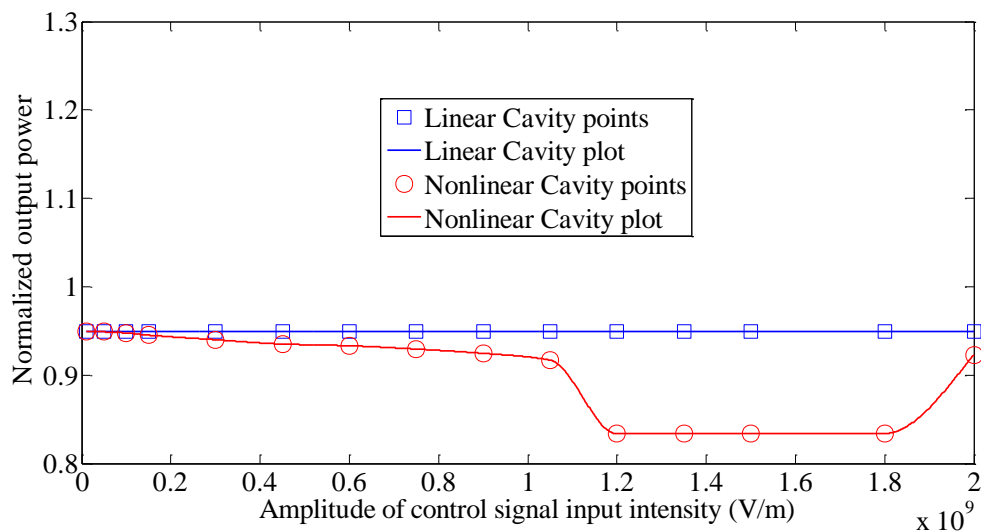


Figure 6 - 34: Power plot of CNP device with gap dimension of 20nm

For 'gap' dimensions of 60 nm the test signal endures less loss due to reduced interaction of test signal with the cavity material. Figure 6-35 shows the results for the device with 'gap' dimensions of 60nm.

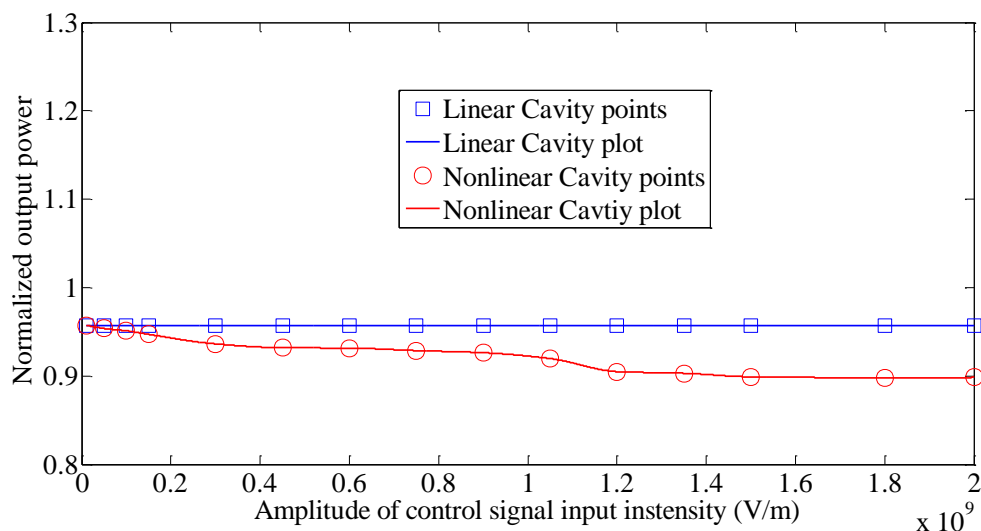


Figure 6 - 35: Power plot of CNP device with gap dimension of 60nm

Through careful engineering of innovative techniques and by modeling novel devices it can be reaffirmed that the SPPs can be modulated to serve the field of Active Plasmonics.

## CHAPTER 7

# CONCLUSIONS AND FUTURE WORKS

### 7.1 Summary and Conclusions

In this thesis, various devices with novel techniques were engineered in order to modulate Surface Plasmon Polaritons. For this purpose Chalcogenide glass having third-order non-linearity is employed. The third-order non-linearity of Chalcogenide glass is modeled and used in the simulator. Special consideration was taken while designing the devices so that they can be fabricated thereby enabling the verification of simulation results with the experimental results. The research work done in this thesis is summarized as follows:

- The third-order non-linear material model was incorporated into the FDTD algorithm that involved the solving of a cubic equation. Instantaneous Kerr nonlinear response was taken into consideration. The material model equations were based on the linear susceptibility ( $\chi^{(1)}$ ) and third order-nonlinear susceptibility ( $\chi^{(3)}$ ).
- A frequency-dependent dispersion model for the linear response of  $\text{As}_2\text{S}_3$  chalcogenide glass was used assuming that the properties of  $\text{As}_2\text{S}_3$  followed the Lorentzian third order non-linear material model.



- Metals that are dispersive in the optical ranges were simulated using 6-pole Lorentz-Drude model.
- The Metal-Waveguide structure was modeled such that it modulated the power and intensity profile of CW SPP propagating on the Metal surface under the influence of various Waveguide input intensity levels.
- The Metal-Insulator-Metal device was shown to modulate the test signal (CW SPP) propagating on the upper metal surface under the influence of various control input intensity signals through the means of loss induction in the ChG glass at higher intensities.
- The Embedded Metal Film structure was shown to modulate the CW SPP propagating across the thin film by shifting its power profile at high control input intensities applied at the bottom metal.
- The Coupled Plasmonic Nanocavities structure successfully modulated the power profile of the CW SPP propagating on the Metal-dielectric interface under the control of pulsed line source by transforming the material behavior in the cavity from linear to non-linear region at high input intensities.

## 7.2 Future Work

This work can be extended into new and exciting domains where the challenge of integrating photonics with electronics can be accomplished by scaling new pinnacles through innovative and novel ideas. Few directions in which this work can be extended are,

- The need and urgency to incorporate various other factual parameters such as temperature, magnetic field, pressure etc., in the FDTD model is required to advance the research in the field of Active Plasmonics.
- New materials and properties such as higher order non-linearities, semiconductor active materials need to be modeled so as to allow easy fabrication of economical structures.
- Materials that can induce non-linearity, change in refractive index or phase change at low input intensities need to be investigated to allow manufacturing of low power consumption devices.
- General software packages that can include structures of various geometries, different material properties and large frequency range of operation by merely selecting the desired parameters from the menu box as is the case in various operating systems can be designed to speed up the investigations and to obtain better and accurate results.
- The current numerical simulator can be extended to 3-D structures in order to simulate the linear dispersion and the third order-nonlinearity for the more realistic 3-D structures.

## REFERENCE

- [1] R. H. Ritchie, "Plasma Losses by Fast Electrons in Thin Films," *Physics Review*, vol. 106, pp. 874–881, 1957.
- [2] J M Pitarke, V M Silkin, E V Chulkov, and P M Echenique, "Theory of surface plasmons and surface-plasmon Polaritons," *Reports on progress in physics*, vol. 70, pp. 1–87, 2007.
- [3] Vasily V. Temnov et al., "Active magneto-plasmonics in hybrid metal–ferromagnet structures," *Nature Photonics*, vol. 4, February 2010.
- [4] Wayne Dickson, Alexey Krasavin, Gregory Wurtz, and Anatoly Zayats, "Nonlinear plasmonics: controlling light with light," *SPIE, newsroom*.
- [5] William L. Barnes, Alain Dereux, and Thomas W. Ebbesen, "Surface plasmon subwavelength optics," *Nature*, vol. 424, pp. 824-830, August 2003.
- [6] Kevin F. MacDonald and Nikolay I. Zheludev, "Active plasmonics: current status," *Laser Photonics*, vol. 4, no. 4, pp. 562–567, 2010.
- [7] Eli Yablonovitch, "Inhibited Spontaneous Emission in Solid-State Physics and Electronics," *Phys. Rev. Lett.*, vol. 58, no. 20, May 1987.
- [8] Sajeev John, "Strong localization of photons in certain disordered dielectric superlattices," *Phys. Rev. Lett.* , vol. 58, no. 23, June 1987.
- [9] Pendry, J.B., Holden, A.J., Robbins, D.J., and Stewart, W.J., "Magnetism from conductors and enhanced nonlinear phenomena," *Microwave Theory and Techniques, IEEE* , vol. 47, no. 11, pp. 2075 - 2084 , November 1999.
- [10] S. Maier, *Plasmonics: Fundamentals and Applications*. New York: Springer, 2007.

- [11] R. Dingle, W. Wiezmann, and C. H. Henry, "Quantum states of confined carriers in very thin Al(x)Ga(1-x)As - GaAs - Al(x)Ga(1-x)As heterostructures," *Phys. Rev. Lett*, vol. 33, pp. 827-830, 1974.
- [12] H. Iwai, "CMOS downsizing toward sub-10 nm," *Solid-State Electron*, vol. 48, pp. 497-503, 2004.
- [13] M. Bohr, "Intel's silicon research and development pipeline," Technical Report 2006.
- [14] A. V. Krasavina and N. I. Zheludev, "Active plasmonics: Controlling signals in Au/Ga waveguide using nanoscale structural transformations," *Applied Physics Letters*, vol. 84, February 2004.
- [15] A. V. Krasavin, K. F. MacDonald, and N. I. Zheludev, "High-contrast modulation of light with light by control of surface plasmon polariton wave coupling," *Applied Physics Letters*, vol. 85, no. 16, October 2004.
- [16] Thomas Nikolajsen, Kristjan Leosson, and Sergey I. , "Surface plasmon polariton based modulators and switches operating at telecom wavelengths," *Applied Physics Letters*, vol. 85, no. 24, December 2004.
- [17] Pacific, Henri J. Lezec, and Harry A. Atwater, "All-optical modulation by plasmonic excitation of CdSe quantum dots," *Nature Photonics*, pp. 402 - 406, 2007.
- [18] Ragip A. Pala, Ken T. Shimizu, and Nicholas A. Melosh, "A Nonvolatile Plasmonic Switch Employing Photochromic Molecules," *Nano Letters*, vol. 8, no. 5, 2008.
- [19] Matthew J. Dicken et al., "Electrooptic Modulation in Thin Film Barium Titanate Plasmonic Interferometers," *Nano Letters*, vol. 8, no. 11, 2008.
- [20] Z L S´amson, K F MacDonald, and N I Zheludev, "Femtosecond active plasmonics: ultrafast control of surface plasmon propagation," *J. Opt. A: Pure Appl. Opt.*, vol.

11 , 2009.

- [21] Jennifer A. Dionne, Kenneth Diest, Luke A. Sweatlo, and Harry A. Atwater, "PlasMOStor: A Metal-Oxide-Si Field Effect Plasmonic Modulator," *Nano Letters*, 2009.
- [22] Vasily V. Temnov et al., "Active magneto-plasmonics in hybrid metal–ferromagnet structures," *Nature Photonics*, vol. 4, February 2010.
- [23] Zsolt L. Sámson et al., "Chalcogenide glasses in active plasmonics," *Phys. Status Solidi RRL*, 2010.
- [24] A. Christ, T. Zentgraf, , S. G. Tikhodeev, J. Kuhl, and H. Giessen, "Controlling the interaction between localized and delocalized surface plasmon modes: Experiment and numerical calculations," *Physical Review B* , vol. 74, no. 155435 , 2006.
- [25] C. J. Powell and J. B. Swan , "Origin of the Characteristic Electron Energy Losses in Aluminum," *Phys. Rev.* , vol. 115, no. 4, pp. 869–875 , 1959.
- [26] E. A. Stern and R. A. Ferrell, "Surface Plasma Oscillations of a Degenerate Electron Gas," *Phys. Rev.* , vol. 120, no. 1, pp. 130–136 , 1960.
- [27] J M Pitarke<sup>1</sup>, V M Silkin , E V Chulkov , and P M Echenique, "Theory of surface plasmons and surface-plasmon polaritons," *Rep. Prog. Phys.*, vol. 70, no. 1, January 2007.
- [28] G. H. Yuan, X. C. Yuan, J. Bu, P. S. Tan, and Q. Wang, "Manipulation of surface plasmon polaritons by phase modulation of incident light," *Optics Express* , vol. 19, no. 1, pp. 224-229, January 2011.
- [29] Guang S. He and Song H. Liu, *Physics of Nonlinear Optics*. Singapore: World Scientific Publishing Co. pte. Ltd, 1999.

- [30] P. Drude, "Zur elektronentheorie der metalle," *Annalen der Physik*, vol. 306, pp. 566-613, 1900.
- [31] P. Drude, "Zur elektronentheorie der metalle; II. Teil. galvanomagnetische und thermomagnetische effecte," *Annalen der Physik*, vol. 308, pp. 369-402, 1900.
- [32] A. D. Rakic et al, "Optical properties of metallic films for vertical-cavity optoelectronic devices," *Applied Optics*, vol. 37, pp. 5271-5283, 1998.
- [33] A. Taflove and S. C. Hagness, "Computational electrodynamics: the finite-difference time-domain method," 2000.
- [34] M. Fujii et al, "High-order FDTD and auxiliary differential equation formulation of optical pulse propagation in 2-D Kerr and Raman nonlinear dispersive media," *Quantum Electronics, IEEE*, vol. 40, pp. 175-182, 2004.
- [35] M. N. D. Sadiko, *Numerical Techniques in Electromagnetics*, 2nd ed.: CRC, 1992.
- [36] W. C. Chew, J. M. Jin, E. Michielssen, and J. Song, *Fast and Efficient Algorithms in Computational Electromagnetics.*, 2001.
- [37] K. Yee, "Numerical solution of initial boundary value problems involving Maxwell's equations in isotropic media," *IEEE Transactions on Antennas and Propagation*, vol. 14, no. 196, pp. 302-307.
- [38] Y. Hao et al, *FDTD modeling of metamaterials: theory and applications.*: Artech House, 2009.
- [39] M. A. Alsunaidi and A. A. Al-Jabr, "A general ADE-FDTD algorithm for the simulation of dispersive structures," *Photonics Technology Letters, IEEE*, vol. 21, pp. 817-819, 2009.
- [40] R H Sagor, M. A. Alsunaidi, and B. S. Ooi, "SPP Propagation in Nonlinear Glass-

Metal Interface," in *8th international conference HONET'11, IEEE*, Riyadh, 2011.

- [41] Z. L. Sámson, et al., "Chalcogenide glasses in active plasmonics," *physica status solidi (RRL)–Rapid Research Letters*.
- [42] W. L. Barnes, "Surface plasmon–polariton length scales: a route to sub-wavelength optics," *Journal of Optics A: Pure and Applied Optics*, vol. 8, p. S87, 2006.

## VITAE

**Name** : Syed Salmaan Rashid.

**Nationality** : Indian.

**Date of Birth** : June 6, 1987.

**Permanent Address** : Q. No. B-773, N.G.O's Colony, Sector – 5,

Vanasthalipuram, Hyderabad, Andhra Pradesh, India - 500070

**Present Address** : Room#811/216, KFUPM, Dhahran, K.S.A.

**Email** : salmaan010@yahoo.com

**Phone** : +91-9441071075

+91-9441066865

**Degrees** :

**Bachelor of Science** in Electronics & Communication Engineering from Osmania University (Sep. 2004 – May. 2008).

**Experiences** :

**Research Assistant** in Electrical Engineering Department of King Fahd University of Petroleum & Minerals (KFUPM) (Feb. 2010 – Jan. 2012).

**Software Engineer (Member Technical)** in Broadridge financial Solutions Pvt. Ltd. at Hyderabad, India.